Universidad Carlos III de Madrid

Departamento de Matemáticas

Tesis Doctoral

Stochastic Dynamics of Substrate-confined Systems: Fisher Fronts and Thin Liquid Films

Autor: Svetozar Nesic

Directores: Esteban Moro Egido
Rodolfo Cuerno Rejado

Leganés, Madrid, 2015

TESIS DOCTORAL

STOCHASTIC DYNAMICS OF SUBSTRATE-CONFINED SYSTEMS: FISHER FRONTS AND THIN LIQUID FILMS

Autor: **Svetozar Nesic**
Directores: **Rodolfo Cuerno Rejado**, **Esteban Moro**

Firma del Tribunal Calificador

		Firma
Presidente:		
Vocal:		
Secretario:		

Calificación :

Leganés, de de

STOCHASTIC DYNAMICS OF SUBSTRATE-CONFINED SYSTEMS: FISHER FRONTS AND THIN LIQUID FILMS

Svetozar Nesic

June 25, 2015

Agradecimientos

Escribir la tesis es un proceso muy parecido al de hacer las maletas antes de dejar un sitio para siempre. Comprimir la vida de los últimos seis años en un libro de apenas cien páginas, a uno le hace repasar el pasado y recordar a todas aquellas personas que han estado en este camino.

Sin duda, esta tesis no hubiera sido posible realizarla sin el gran apoyo, las experiencias emitidas y la paciencia de mis supervisores Esteban y Rodolfo. No puedo no mencionar la dedicación y esmero de Rodolfo para hacer las cosas bien. Quiero expresar mi gratitud a todos los miembros del departamento de matemáticas y a los del grupo interdisciplinar de sistemas complejos (GISC) por haberme acogido y ayudado todo este tiempo. Dar clases de problemas de cálculo uno y dos fue una escapada a un mundo simple y bonito, donde he tenido suerte de repartir clases con Javi Laguna, Fernando, Tommaso y Pablo. También, he tenido oportunidad de escuchar muy buenas clases del programa de máster, como las de Carlos, José, Yuri, etc. Hablando de buenas charlas, es imposible olvidarse del seminario que dio Andy. Fue uno de esos que cuando se acaba sales disparado a resolver un problema. Sí, Andy, con el que los problemas abiertos y la cerveza cuadran muy bien..

Trabajar en el despacho 2.2D06B ha sido muy agradable gracias a mis magníficos compañeros, Edo, Sergio, Juanma y Dani. Gracias a Edo por siempre estar dispuesto a ayudar en cualquier problema, desde resolver segmentation faults, discutir problemas físicos, hasta estudiar bien las noches madrileñas. La investigación a veces suele ser muy deprimente y estresante. Esos momentos se superan recuperando la motivación fuera de la academia. Aquí especialmente le agradezco a Sergio por su admiración hacia mi talento deportivo en las canchas de voleibol y fútbol. En los momentos difíciles siempre está Juanma para ofrecer tranquilamente una explicación física de lo que está pasando. A parte de eso, las conversaciones con Juanma y Dani siempre han sido muy interesantes y motivantes.

La universidad de Carlos III ha hecho posible que realizara una estancia de tres meses en la universidad NJIT de Newark. A raíz de eso empezamos a colaborar con uno de los grandes investigadores en el mundo de microfluídica, Lou Kondic. La colaboración resultó en dos papers y muchas ideas por intentar realizar. Lou introdujo una nueva dimensión en nuestra investigación y su constante interés, ayudas e ideas, forman una buena parte de esta tesis. Ademas, gracias a él y su familia estar en un país tan social y culturalmente raro como eeuu fue mucho más agradable.

A parte de experiencia académica, vivir 6 años en Madrid ha sido una oportunidad inolvidable. En primer lugar le doy gracias a Jelena por apoyar mi solicitud, hacer posible que viniera aquí y siempre estar ayudándome a superar la diferencia cultural y académica. Por otro lado, llegar a entender y respirar una cultura tan profunda como la española se lo debo a Paloma. Cuando dentro de unos años saque esta tesis a quitar el polvo, espero que ella esté donde siempre ha querido estar, en la ópera.. Mis más sinceros agradecimientos también van a las personas que a parte de muchos buenos momentos han estado siempre y cuando las necesitaba, Gio y Dario, Milena y Djordje, Edo Carlesi. Son muchas más las personas que han enriquecido mi vida aquí, entre otras, mis compañeros de piso May, Javi y Silvia, Marco, Elena, Andrea, Alexis y Marisa, el equipo de baloncesto Lavapiés, el equipo de la universidad, el grupo scientifico-gastronomico formado por Edgar, Dani, Uri, Edo, y el miembro externo Ángel. Aunque estemos todos en diferentes ciudades, países, agradezco las oportunidades de cruzarme con mis compañeros de la carrera, Jelena, Milos, Lele, Kepcija, Marija*2, Marina, Kristina y volver a saber de ellos. Finalmente, gracias a mi bailarina preferida Karioca y su toque artístico que ha introducido en mi vida numérica.

Durante todos estos años, cambiaba los horribles calurosos veranos madrileños por los un poco menos horribles veranos belgradenses. Es cuando uno siente lo que realmente es la familia y el amor incondicional que transmiten, lo que son los amigos de toda la vida, tu gente. Sin ellos nada de esto tendría el mismo sentido..

Contents

Introduction

Traditionally, research in statistical physics, has been focused very strongly in the analysis of equilibrium states. The blooming development of computers during the last few decades has opened the possibility for scientists to study non-equilibrium phenomena through massive numerical simulations. Besides the main goal, which is to determine the state into which a system would evolve under certain physical and initial conditions, numerical simulations can also provide a better understanding of the dynamics, and sometimes even point out the possibility of analytical solution [1–3]. A large variety of models have been successfully studied numerically, starting form simple particle models with given particle interactions to complex surfaces in high space dimensions. Possible applications of these models also spread across different scientific fields, such as biology, chemistry or even economy. On the other hand, current industrial needs require to quantitatively describe processes that take place at small (micro and nano) scales. Especially important is the study of interfacial phenomena, as surface growth processes are relevant in chemical reactions, erosion processes which have huge industrial interest, fluid flows, etc.

The lack of detailed information about or the sheer complexity of the system interactions, for example intermolecular forces between fluid particles, has brought stochastic theories into the focus of non-equilibrium studies. By including fluctuations into the description of a system, the evolution process can be significantly affected. Fluctuations are seen to accelerate the spreading of liquid drops [4, 5], slow down pulled fronts [6–8], etc.

This thesis is a result of a study of the influence of fluctuations in the behavior of two paradigmatic models in soft condensed matter physics. The first one is a reaction-diffusion process that corresponds to the time evolution of a continuum density function through the so-called Fisher-Kolmogorov-Peterovsky-Piscunov (FKPP) partial differential equation [9–11]. Under certain initial conditions, this equation develops traveling wave solutions which describe well e.g. chemical reactions [12] and many dynamical systems studied in biology [11]. Our interest is directed towards a more realistic stochastic equation, in order to study how the dynamics is affected by the fluctuations in the number of agents (molecules, bacterias, etc.) which are interacting in the underlying chemical or biological systems. The second topic of this thesis is related to the stochastic lubrication equation. Currently there are many industrial processes in which fluid dynamics is relevant at microscopic and nanometric film thicknesses [13–16]. On these scales the standard lubrication equation fails to describe the dynamics accurately, while the complex molecular structure introduces defects in the fluid free surface that can be accounted for through incorporation of thermal fluctuations [4, 17, 18]. We have studied the stochastic thin film evolution for the same reason as for FKPP fronts, namely, to see how fluctuations influence the dynamics. Actually, the stochastic system can provide a better understanding of the evolution seen in many thin film dewetting experiments [19–22].

We study these two continuum models numerically using algorithms tailored for stochastic partial differential equations. The presence of noise requests a large number of realizations so that the algorithms have to be adjusted to decrease the already extensive computational times to a minimum. Furthermore, both models describe the evolution of physically non-negative variables, namely, a density in the case of the FKPP equation and the film thickness for thin liquid films. Due to the presence of an underlying substrate, these variables are moreover not invariant under shift transformations ($h \to h + \delta h$), i.e. there exist privileged values of either density or thickness. These two facts pose potential problems for the stability of numerical solutions, as symmetric fluctuations around the mean may lead to non-physical negative values of density or thickness. These difficulties need to be circumvented by numerical schemes, and for this reason we also present the algorithms in detail.

This thesis has the following structure:

- **Chapter 1** gives an overview of some concepts and tools which are widely used to deal with surface growth systems in which rough surfaces evolve in time. First, we briefly introduce basic particle and continuum models of surfaces. Although different, many of such models have similar large-scale behavior, i.e. they can be classified into universality classes. One of the most celebrated ones, the KPZ universality class is introduced in some detail, as later on we show its relevance for stochastic FKPP fronts. Finally we describe systems that are not scale invariant but, rather develop instabilities that lead to pattern formation, which later on will be seen in thin liquid films.

- In **Chapter 2**, the stochastic FKPP (sFKPP) equation is described. The chapter starts with general reaction-diffusion (RD) processes that are modeled through partial differential equations. Then, the FKPP equation is introduced as a RD process. We summarize briefly some mathematical properties of the equations, and then motivate and derive the inclusion of a stochastic term, to account for fluctuations due to the finite number of interacting particles in a volume. The chapter ends with previous results from both numerical and analytical studies.

- In **Chapter 3** we give a full description of the algorithm employed to simulate the sFKPP equation. The algorithm is based on a splitting-step scheme, which is introduced first. Then the equation is split into a stochastic and a deterministic part, which are both are numerically solved using an explicit Euler method and an associated Fokker-Planck equation, respectively.

- In **Chapter 4** we present our study of two-dimensional sFKPP fronts. The study is performed by simulating the sFKPP equation. We argue which universality class do these fronts belong to and provide extensive numerical analysis to support our conclusions. Finally, we formulate scaling relations for the fluctuation spectrum showing that the front morphology is affected even by extremely small fluctuations. The results of this chapter (except for Section 4.2) are published in Ref. (1) below.
- **Chapter 5** is an introduction to the second part of our investigation, namely, stochastic thin liquid films. We derive the stochastic lubrication equation (SLE) from the stochastic Navier-Stockes equations using the lubrication approximation. Here the noise originates in the thermal fluctuations in the distribution of molecular velocities in the fluid. Finally we discuss how to model the solid-liquid and liquid-gas interactions.
- **Chapter 6** In this chapter we describe in detail how to adjust the implicit scheme to simulate the SLE in $1d$ and $2d$. We also provide details on the rescaling to non-dimensional units to be employed in our simulations.
- In **Chapter 7** we present our study on the effect that thermal noise has on droplet spreading. We show that fluctuations accelerate the spreading, not only in the surface-tension-dominated regime, but also in the gravity-dominated regime. Furthermore, we show that the fixed contact angle given by the standard Young-Laplace formula slightly changes under the influence of fluctuations. The results of this chapter are published in Ref. (2) below
- **Chapter 8** is finally dedicated to dewetting phenomena, both in deterministic and stochastic systems. We first discuss the predictions from linear analysis and then present our numerical results on the fully non-linear evolution. The results of this chapter have been submitted for publication, and are contained in Ref. (3) below.

Published Articles and Preprints

1. S. Nesic, R. Cuerno, E. Moro, "*Macroscopic Response to Microscopic Intrinsic Noise in Three-Dimensional Fisher Fronts*", *Physical Review Letters* **113**, 180602 (2014).
2. S. Nesic, R. Cuerno, E. Moro, L. Kondic, "*Dynamics of thin fluid films controlled by thermal fluctuations*", *European Physical Journal Special Topics* **224**, 379 (2015).
3. S. Nesic, R. Cuerno, E. Moro, L. Kondic, "*Role of Thermal Fluctuations in Nonlinear Thin Film Dewetting*", submitted to *Physical Review Letters* (2015).

1

Kinetic roughening

Modeling physical systems through the evolution of their surfaces has been a breakthrough in diverse contexts, such as physics, biology, and their applications. The approach is somehow different than usual when physical systems are described. Instead of trying to implement specific physical mechanisms that determine the dynamics of the surface in a system, see the fig. 1.1) one could consider the evolution of the latter phenomenologically. Moreover, here we consider surfaces in which randomness plays an important role. Typical examples include e.g. bacterial colonies that go through a food source leading to growth of an aggregate with a rough surface, or deposition processes such as snow falling. Snowflakes fall randomly and deposit onto a surface, causing space-time fluctuations in the boundary of the snow deposits. A similar, but industrially much more important process, is molecular deposition, an experimental process whereby computer chips are produced. The industrial interest to model these systems is to reduce the roughness of a thin film as much as possible. In order to achieve that goal, it is important to know where the surface fluctuations come from. Mathematical models could show how these systems should evolve, and a comparison to similar noiseless systems usually gives a good description of the effect that noise has.

Another important property that has to be taken into account is the length scale. A snow surface seen from large distances looks completely smooth, but if we come close enough it looks rough. On the other hand, there are surfaces whose morphology remains invariant in some sense when described at different length scales. These systems are called **fractals** [1, 24–26]. In any case the length scale is an important physical property for constructing mathematical models.

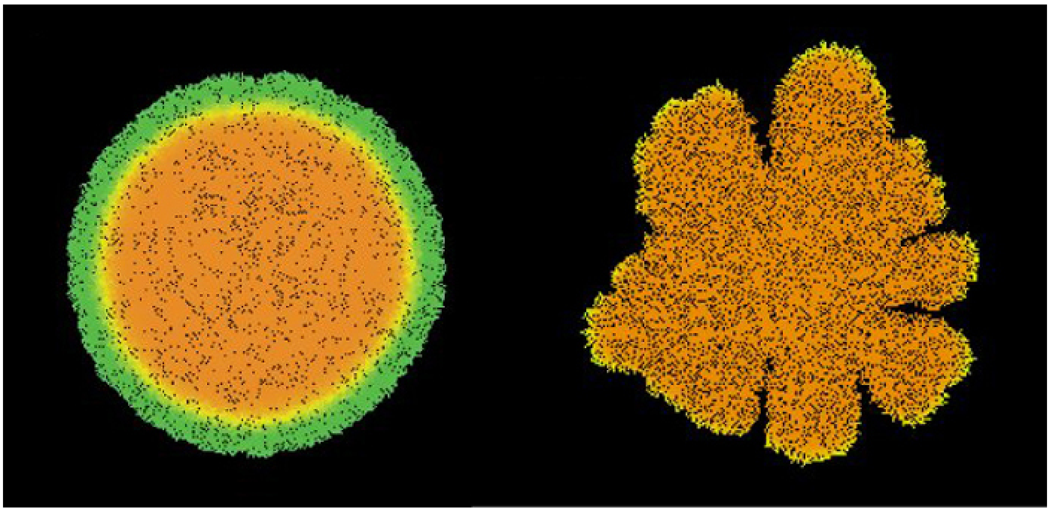

Figure 1.1: Simulations of a model that describes colonies of rod-shaped bacteria growing on solid substrates for two different parameter conditions. Picture taken from Farrell *et al.* [23]. In each case, the boundary separating filled from empty sites defines a rough surface (interface).

Speaking of mathematical models, usually there are two conceptually different ways to formulate them. Thus, one has **discrete models** or **continuum equations**. **Discrete models** usually deal with particles whose interactions are well defined. Then, every new particle that arrives interacts with the surround, changing the overall morphology. **Continuum equations**, mostly stochastic partial differential equations, represent a surface as a continuous function that evolves in time. Naturally, **discrete models** describe better short length scales where the short interactions are relevant, but both types of models should give similar results at larger scales. This provides a powerful way to classify different models based on their scaling properties.

In this chapter we introduce mathematical tools to deal with the growth of rough surfaces at different length and time scales. These tools will help us to characterize a vast variety of systems (for example snow flakes and atom deposition processes) into a few universality classes. Universality classes define a set of large-scale properties that should be common, for all the systems belonging to the same class. Therefore, their classification leads to a possible better understanding of the main physical mechanisms that drive the evolution.

1.1 Caracterization of rough surfaces

Before introducing specific physical models, here we present a phenomenological characterization of the morphology of rough surfaces, which later on will be used to analyze discrete and continuum models in Secs. 1.2 and 1.3, respectively. Moreover, the approach can be also applied to reaction-diffusion processes such as stochastic Fisher traveling waves which will be presented in detail in Chapter 2.

In order to describe a surface we define a function $h(\vec{r}, t)$ that represents the surface height above position $\vec{r}$ on a reference surface (in $1d$ systems, a line), see Fig. 1.2(a). In stochastic systems, which are the main topic of this thesis, the height function roughens in time due to the effect of fluctuations. The natural variables to use are the mean height and roughness, which characterize how rough the surface is in time. The mean height is defined as a sum for systems on a lattice (discrete systems),

$$\overline{h}(t) = \frac{1}{L^d} \sum_{\vec{r}_i \in \mathbf{D}} h(\vec{r}_i, t), \tag{1.1}$$

where d is the space dimension of the system, L its lateral size in the domain $\mathbf{D}$ (for simplicity we assume that all space dimensions of the reference surface have the same extensions) so that $\vec{r} \in \mathbb{D}$ and $\mathbf{D}$ is a subdomain of $\mathbb{R}^d$. For continuum systems the sum becomes an integral. In general, when a fluctuations are relevant it is more convenient to average the measured roughness over different noise realizations. Therefore, unless stated differently throughout the thesis the roughness function will be given by

$$w^2(L, t) = \frac{1}{L^d} \left\langle \sum_{\vec{r}_i \in \mathbf{D}} (h(\vec{r}_i, t) - \overline{h}(t))^2 \right\rangle. \tag{1.2}$$

where $\langle \cdots \rangle$ is average over different noise realizations. Frequently one considers flat initial condition, i.e. $h(\vec{r}, 0)$ is a constant. As time increases, the surface becomes more and more rough. Therefore, with a large generality one expects the roughness to scale as

$$w(L, t) \sim t^{\beta}, \tag{1.3}$$

where β is called the **growth exponent**. Besides fluctuations, these systems are subject to forces that tend to smooth the surface. The rougher the surface is, the stronger these forces are. Therefore, one expects for a finite system that the roughness will not grow indefinitely but rather saturates [a typical behavior is sketched in Fig. 1.2(b)]. Actually one expects that the saturation roughness scales with the system size obeying a power-law as well [1],

$$w_{sat}(L) \sim L^{\alpha}. \tag{1.4}$$

The exponent α is usually called the **roughness exponent**. In general, even if the initial surface is not correlated, the interplay between the various forces introduces a correlation

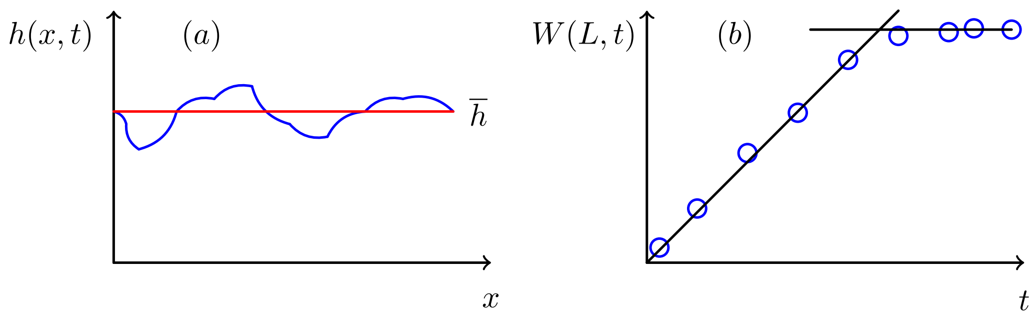

Figure 1.2: (a) Example of a one-dimensional rough surface. The blue line represents the height at position x, while the red line corresponds to the mean height of the surface. (b) Surface roughness function (blue circles) vs time; After increasing as a power-law, it saturates as a result of the interplay between deterministic and stochastic forces. Solid black lines are obtained by linear regression.

between different points on the surface. As time passes the system gets more and more correlated until it finally becomes fully correlated and the roughness function saturates. Therefore, we expect that at a given time t, a length ξ exists so that any two points on the surface within the distance ξ are correlated, while distances larger than ξ they are not. We assume that the correlation length grows as a power-law $\xi \sim t^{1/z}$. Then the system will become fully correlated after a time t_x when the correlation length reaches the system size,

$$t_x \sim L^z, \tag{1.5}$$

where z is called the **dynamic exponent** and t_x is the saturation time. Note that, if a system obeys (1.3) and (1.5), then for times longer than the saturation time the roughness depends only on the system size as

$$w(L, t_x) = t_x^\beta \sim L^{z\beta}. \tag{1.6}$$

We thus obtain a relation between the exponents:

$$z = \frac{\alpha}{\beta}. \tag{1.7}$$

This allows us to rewrite the roughness as

$$w(L,t) \sim t^\beta = t_x^\beta \left(\frac{t}{t_x}\right)^\beta \sim L^\alpha f(\frac{t}{L^z}), \tag{1.8}$$

which is useful to compare systems at different length and time scales, as the function f is non-dimensional [see Fig. 1.3(b)] it behaves as

$$f(x) \sim \begin{cases} x^\beta & \text{if } x \ll 1 \\ \text{const.} & \text{if } x \gg 1 \end{cases}. \tag{1.9}$$

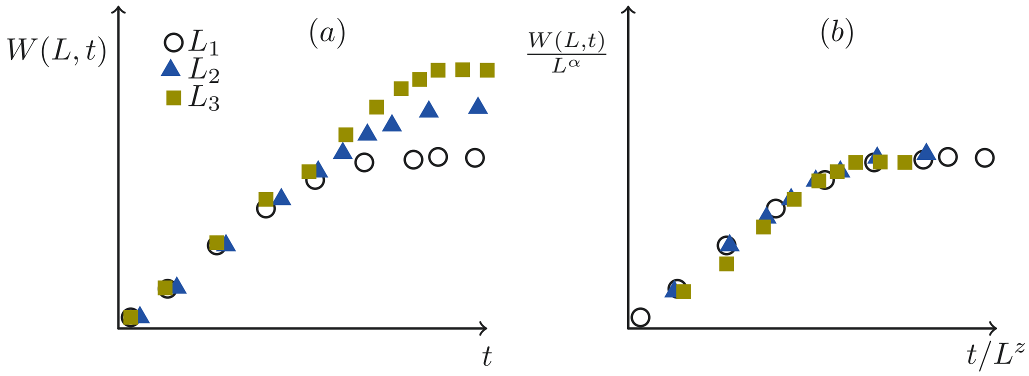

Figure 1.3: (a) Example of a roughness function for different system sizes, where $L_1 < L_2 < L_3$. (b) Rescaling the roughness function and time the curves collapse if the system obeys the Family-Vicsek scaling Ansatz (1.8)-(1.9).

The relation (1.8) is known as the Family-Vicsek scaling Ansatz [24]. The function f is called the scaling function and it only depends on a single variable. All three dynamic laws together with the Family-Vicsek scaling ansatz can be obtained by introducing the change of variables $x \to \vec{r}' = b\vec{r}$, $t \to t' = b^z t$, $h \to h' = b^\alpha h$ into the definition of roughness function, Eq. (1.2), and requesting invariance within a correlation length-scale.

The three scaling exponents characterize the dynamics of the surface growth and their values define an **universality class**. As already mentioned, many different microscopic mechanisms show the same macroscopic behavior, which results in having the same exponents values. Usually, the universality classes are described by stochastic partial differential equations, i.e. continuum models, which will be introduced in Sec. 1.3.

Besides the simplest models, it is almost impossible to analytically obtain the roughness function explicitly. However, by assuming the Family-Vicsek ansatz, one could calculate the exponents by collapsing the roughness curves of numerical results, see e.g. Fig. 1.3.

There are other observables related to the surface roughness that can also efficiently describe the evolution of a surface. One of the most frequently used is the height-difference correlation function, which is defined as

$$G(\vec{r}) = \left\langle \frac{1}{L^d} \sum_{\vec{r}_i \in \mathbf{D}} [h(\vec{r}_i, t) - h(\vec{r}, t)]^2 \right\rangle . \tag{1.10}$$

If we repeat the arguments stated above, we obtain the following scaling relation [27] for systems that obey the FV ansatz,

$$G(r) \sim \begin{cases} t^{2\beta} & \text{if } r \ll t^{1/z} \\ r^{2\alpha} & \text{if } r \gg t^{1/z} \end{cases} , \tag{1.11}$$

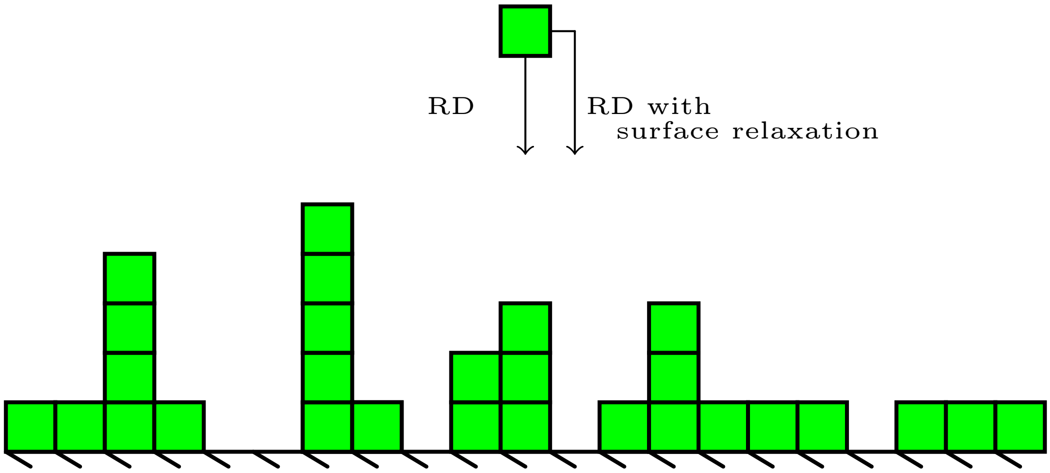

Figure 1.4: The RD particle sticks to where it falls while the RD with relaxing surface particle falls off if the neighbor position is smaller.

Hence, we can rewrite the function G as $G(\vec{r}, t) \sim |\vec{r}|^{2\alpha} g(t/|\vec{r}|^z)$, where the non-dimensional scaling function g is

$$g(x) \sim \begin{cases} x^{2\beta} & \text{if } x \ll 1 \\ \text{const} & \text{if } r \gg 1 \end{cases} . \tag{1.12}$$

1.2 Discrete models of kinetic roughening

Since this thesis is devoted to continuum models, here we give only a brief overview on discrete models in order to show similarities to continuum systems and to illustrate the occurrence of universality classes.

The simplest discrete model is certainly **Random Deposition (RD)** [1]. The model describes systems where particles are falling vertically from a randomly chosen position onto a horizontal surface and stick irreversibly exactly where they land. The model is very simple. We divide the space into L columns of unit width. At each time step a particle falls along a randomly chosen column, see Fig. 1.4. Each column has an equal probability to receive a new particle, $p = 1/L$. It is easy to show [1] that after depositing N, particles the height values have a binomial distribution, which implies that the expected height is $\langle h \rangle \sim N$. As one particle falls at each time step, the expected average height is $\langle h \rangle \sim t$. The roughness (1.2) is also easy to calculate for this case [1, 25, 28]. Using the binomial distribution function and the definition of the roughness (1.2) one shows that $w(t, L) \sim t^{1/2}$. The roughness for longer times does not depend on the system size L, therefore it grows unboundedly. There is no mechanism to introduce correlation, hence the roughness exponent α is not well defined.

Two models which are closely related to the RD are **Random Deposition with surface relaxation** and **Ballistic Deposition (BD)**. The basic idea of the RD applies for these two models, just with one additional fact. BD particles can stick to the neighbor column if the height is larger than that of the column the particle was originally falling to. This introduces a lateral growth. There is no analytical solution to this problem but numerical simulations show that the correct exponents are $\beta = 0.33 \pm 0.006$ and $\alpha = 0.47 \pm 0.02$ [1,28] for a $1d$ system. On the other hand, the RD with surface relaxation permits a particle to move from the column to that neighbor column that has the smallest height. This relaxation actually introduces correlations and it leads to the saturation in the roughness function [28]. Unfortunately, it is not possible to solve this model analytically either. Simulating numerically the model in one dimension one obtains $\beta = 0.24 \pm 0.01$ and $\alpha = 0.48 \pm 0.02$ [1]. It is important to state that these results hold only for one-dimensional systems and that the dimensionality often plays an important role.

1.3 Continuum models of kinetic roughening

Basic continuum models that describe the dynamics of a surface are provided by a Langevin equation of the form

$$\frac{\partial h(\vec{x},t)}{\partial t} = F(h,\vec{x},t) + \eta(\vec{x},t), \tag{1.13}$$

where $\vec{x} \in \mathbb{R}^d$ and $F(h,\vec{x},t)$ is a deterministic term which usually depends on local properties of the surface, like the surface slope or curvature. The term $\eta(\vec{x},t)$ represents random fluctuations and is usually taken to be Gaussian, with zero mean,

$$\langle \eta(\vec{x},t) \rangle = 0, \tag{1.14}$$

and uncorrelated,

$$\langle \eta(\vec{x},t)\eta(\vec{x}',t') \rangle = D\delta^d(\vec{x}-\vec{x}')\delta(t-t'). \tag{1.15}$$

Here D provides the noise strength, which in physical systems is related to e.g. the system temperature or to e.g. an external flux of particles. Fluctuations also may arise from the resistance of the medium, e.g. to fluid flow. Such fluctuations are time-independent so that the noise term reads $\eta(\vec{x},h)$ and it is called quenched noise. Depending on the particular case one or the other noise term could be used. In this thesis, only thermal noise will be considered.

The function $F(h,\vec{x},t)$ is the one responsible for the space correlations of the system, and its interplay with the noise leads to the specific values of exponents α,β and z introduced in Sec. 1.1. In general the function $F(h,\vec{x},t)$ may have many restrictions in order to describe such specific physical systems. The restrictions define a set of symmetries that the function $F(h,\vec{x},t)$ has to satisfy. For instance, if we assume that growth events do not depend on the instant when we start to measure time, $F(h,\vec{x},t)$ should not depend explicitly on time. The same logic can be used for the space coordinates $\vec{x}$, hence $F(h, \vec{x}, t)$ should only depend on the height of the interface $F(h)$.

On the other hand, in many cases the evolution of the surface does not depend on where the explicit value of $h(\vec{x})$ is, so that we can not have any explicit dependence on h either, but only its derivatives since $\nabla(h(\vec{x}) + \delta_h) = \nabla h(\vec{x})$. Finally, not all orders of derivative are expected to satisfy surface dynamics symmetries. Although all orders are invariant under translation, they are not all invariant under space inversion. If we change variables as $\vec{x} \to -\vec{x}$, for isotropic systems correlations are not expected to change, but some derivatives will. Therefore we have to exclude odd-order derivatives. To satisfy all previous symmetry relations, $F(h)$ can only include terms like $\nabla^{2n}h$, $(\nabla h)^{2n}$ and their combinations $\nabla^{2n}h(\nabla h)^{2m}$. The simplest case is the **Edwards-Wilkinson (EW)** equation, which for simplicity we consider in $1d$:

$$\frac{\partial h(x,t)}{\partial t} = \nu \nabla^2 h(x) + \eta(x,t). \tag{1.16}$$

The first term on the rhs is usually called height diffusion or surface tension. Here we have constructed this equation from symmetry principles but it can be also derived as a physical model. Namely, this equation is also a special case of Gaussian approximation of the Ising model at the critical temperature [29, 30], where the noise represents thermal fluctuations.

The EW equation (1.13) and in general any linear Langevin equation where $F(h)$ only contains linear terms, can be solved analytically. A natural approach in order to eliminate the gradients is to Fourier-transform the height function. This is especially useful as many surface growth models fulfill periodic boundary conditions. It can be also easily adapted to zero derivative boundary conditions by changing the Fourier *cosine-sine* basis to only *cosine* basis [31]. The Fourier transformed height function in one dimension reads

$$\mathcal{F}(h(x,t)) = \hat{h}(q,t) = \frac{1}{\sqrt{2\pi L}} \int_{-\frac{L}{2}}^{\frac{L}{2}} e^{i\,x\cdot q} h(x,t)\, dx, \tag{1.17}$$

where q is a vector that takes values $q = [0, 2\pi]$. Assuming the deterministic term in (1.13) has the form $F(h) = \nabla^{2n}h$ (where the EW equation is the particular $n = 1$ case) we get

$$\mathcal{F}(\nabla^{2n}h) = (-1)^n q^{2n} \hat{h}(q,t), \tag{1.18}$$

while the noise correlations transform as

$$\langle \eta_q(t)\, \eta_{q'}(t') \rangle = 2D\delta_{q,-q'}\delta(t-t'). \tag{1.19}$$

The resulting equation fits the general form

$$\frac{\partial \hat{h}_q}{\partial t} = \nu \omega_q \hat{h}_q + \hat{\eta}_q(q,t), \tag{1.20}$$

where ω_q is a polynomial in q that appears after transforming the space derivatives. For the EW equation (1.19), $\omega_q = -q^2$. This equation is now easy to solve, and the solution is

$$\hat{h}_q = e^{-D\omega_q t} \int_0^t e^{\nu\omega_q s}\, \hat{\eta}_q(q,s)\, ds, \tag{1.21}$$

where the initial condition is a flat surface, $h(x, t = 0) = 0$. Besides the possibility to analytically solve the Langevin equation, Fourier-transformed functions can also provide new convenient expressions to obtain the scaling exponents. In general, these relations could be easier to solve in order to obtain the scaling exponents. Therefore, we can also define correlation function in Fourier space. A particularly useful one is called structure factor and is defined as

$$S(q) = \langle h_q h_{-q} \rangle, \tag{1.22}$$

There is an exact relation between the structure factor and the roughness [recall the definition (1.2)], being

$$w^2(t) = \frac{1}{L^d} \sum_{q \neq 0} S(q), \tag{1.23}$$

where the sum becomes an integral for continuum systems. From the definition of the structure factor (1.22) and the definition of the height-difference correlation function (1.10) it easy to derive the exact relation

$$G(\vec{r}) = \frac{2}{L^d} \sum_q S(\vec{q}) \left[1 - \cos(\vec{q} \cdot \vec{r})\right]. \tag{1.24}$$

For linear systems the structure factor can be easily found analytically. The average over the noise terms of the product of solutions (1.21) for q and $-q$ using (1.19) gives

$$S(q, t) = D \frac{e^{2\nu\omega_q t} - 1}{\nu\omega_q}, \tag{1.25}$$

The second term on the numerator vanishes exponentially fast, so that after a long enough time the structure factor becomes

$$S(q, t) = \frac{-D}{\nu\omega_q} \sim \frac{1}{q^2}. \tag{1.26}$$

The scaling relation of the one-dimensional height-difference correlation function (1.11) implemented into Eq. (1.24) determines the following exponent relation

$$2\alpha + d = 2 \quad \Longrightarrow \quad \alpha = 1/2. \tag{1.27}$$

On the other hand, at early times a Taylor expansion of Eq. (1.25) when $t \to 0$ shows that the structure factor grows linearly in time. Thus, Eq. (1.23) implies $w \sim t^{1/2}$, the nodes are independent and the evolution is the same as for the random deposition model. For later times, the diffusion term introduces correlations. To find the growth exponent β at these stages of the evolution we use the integral form of Eq. (1.23) in $1d$, and we assume that the system size is large ($L \to \infty$, $q \in [2\pi/L, 2\pi]$), so that

$$w^2(t) = \frac{D}{\nu} \int_0^{2\pi} \frac{1 - e^{-2\nu q^2 t}}{q^2} dq \sim t^{1/2} \quad \Longrightarrow \quad \beta = \frac{1}{4}. \tag{1.28}$$

Finally, the dynamic exponent z is obtained from the Family-Viscsek relation (1.8) $z = \alpha/\beta = 2$. All three exponents define the **Edwards-Wilkinson universality class**.

The same result can be obtained more elegantly by a simple rescaling of the EW equation. As mentioned in Sec. 1.1, we introduce the following change of coordinates

$$x \to x' = bx \qquad t \to t' = b^z t \qquad h \to h' = b^\alpha h. \tag{1.29}$$

Then, the partial derivatives are

$$\frac{\partial h'}{\partial t'} = b^{\alpha - z}\frac{\partial h}{\partial t} \qquad \nabla'^{2n} h' = b^{\alpha-2n}\nabla^{2n} h \qquad (\nabla' h')^{2n} = b^{2n(\alpha-1)}(\nabla h)^{2n}, \tag{1.30}$$

while the noise scales as

$$\langle \eta(bx, b^z t)\, \eta(bx', b^z t')\rangle = b^{-d-z} D\delta^d(x - x')\delta(t - t'). \tag{1.31}$$

Using these results, we can rewrite Eq. (1.13) in the primed coordinates as

$$\frac{\partial h}{\partial t} = b^{-\alpha+z} f(b)F(h) + b^{-\alpha+\frac{z}{2}-\frac{d}{2}}\eta(x,t), \tag{1.32}$$

where $f(b)$ depends on the from of the function $F(h)$ and primes have been dropped. If we impose that Eq. (1.32) remains invariant under (1.29), we get relations for the deterministic growth law

$$b^{-\alpha+z} f(b) = 1, \tag{1.33}$$

while the noise amplitude D remains unchanged $D' = D$ when

$$z = d + 2\alpha. \tag{1.34}$$

This exponent relation is known as hyperscaling. For the particular case of the Edwards-Wilkinson equation, we could easily obtain all three exponents. After rescaling, Eq. (1.16) becomes

$$\frac{\partial h(x,t)}{\partial t} = \nu b^{z-2}\nabla^2 h(x) + b^{-\alpha+\frac{z}{2}-\frac{d}{2}}\eta(x,t), \tag{1.35}$$

and scale invariance implies $z = 2$ together with hyperscaling, thus

$$\alpha = \frac{2-d}{2}, \qquad \beta = \frac{2-d}{4}. \tag{1.36}$$

For the one-dimensional EW system the exponents correspond to the analytical solution. Moreover, they are the same as for the Random Deposition with surface relaxation discrete model, described in the previous section. The EW equation is certainly easy to solve, but in many other cases it will not be possible to obtain the exponents just by a rescaling of the equation.

In general, a continuum equation could provide exponents that describe whole sets of discrete models in nature. Finding the exponents analytically, as it is demonstrated for the EW equation, is not easy task as it seems, and for many important equations it is simply not possible. In some cases, finding the a discrete model that has the same properties as the equation and simulating it could give us exponents better than the equation itself.

Besides the Edward-Wilkinson universality class there are additional ones that are of great interest for surface growth problems such as the **Kardar-Parisi-Zhang (KPZ)**, **Linear** and **non-Linear Molecular Beam Epitaxy** universality classes [32, 33], etc. The main difference between the KPZ and the other three universality classes is the conservation mas law which in the KPZ scenario is not fulfilled. Actually, if the surface height grows in absence of conservation laws, e.g. if bulk vacancies are significant, the expected asymptotic growth is KPZ. In addition, the KPZ universality class is of special interest to us as stochastic Fisher fronts are related to it. Therefore, the KPZ equation will be presented in detail in the next section.

1.4 Kardar-Parisi-Zhang equation

After the Edwards-Wilkinson equation, perhaps the next simple continuum model is Kadar-Parisi-Zhang (KPZ) equation [34] which is capable of reproducing the kinetic roughening properties of a wide class of non-equilibrium systems. This equation is not merely more complex mathematically than the EW, but it has an increased physical complexity. Comparing to the Edwards-Wilkinson equation, the KPZ has just an additional nonlinear term that is symmetric under space inversion $x \to -x$, namely,

$$\frac{\partial h(x,t)}{\partial t} = \nu \nabla^2 h(x) + \frac{\lambda}{2}(\nabla h)^2 + \eta(x,t). \tag{1.37}$$

This equation is equivalent to the stochastic **Burgers** equation [35, 36] which describes fluid mechanics processes [37]. A physically motivated derivation of the KPZ continuum model is analogous to the Ballistic Deposition model mentioned in Sec. 1.2. A particle with height $v\delta t$ falls vertically towards the surface and sticks to it. Unlike the RD model, here the surface has a curvature and slopes, hence the increase in height is in the direction perpendicular to the surface, see Fig. 1.5. The vertical increase is

$$\delta h = v\delta t\sqrt{1 + (\nabla h)^2}. \tag{1.38}$$

If the surface slope is small, $\nabla h \ll 1$, the equation becomes

$$\delta h = v\delta t + \frac{v}{2}\delta t(\nabla h)^2. \tag{1.39}$$

The second term on the RHS is actually the non-linear, quadratic term of the KPZ equation, responsible for the so-called lateral growth. It is easy to see that this non-linear mechanism does not conserve the value of the mean height and it generates an additional growth velocity proportional to the parameter λ. Adding the Edwards-Wilkinson term (which represents surface relaxation by e.q. surface tension) we obtain the full KPZ equation. Eq. (1.37) cannot be written in the variational form

$$\frac{\partial h}{\partial t} = -\mu\frac{\delta H}{\delta h} + \eta(x,t), \tag{1.40}$$

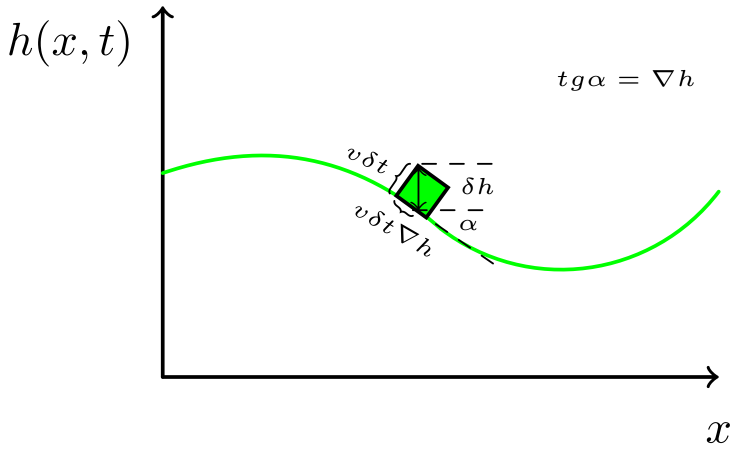

Figure 1.5: A sketch of KPZ surface growth.

with a constant mobility μ [38, 39], which means that the KPZ equation is a dynamical system that describes purely non-equilibrium processes [40, 41]. As the dynamics are almost the same as for the Ballistic Deposition model, if we use the same rescaling as for the Edwards-Wilkinson equation (1.29), we should get the same exponents, which are $\beta = 0.33 \pm 0.006$ and $\alpha = 0.47 \pm 0.02$ for a $1d$ system [1, 34]. The rescaling in (1.29) provides

$$\frac{\partial h}{\partial t} = \nu b^{z-2}\nabla^2 h + \frac{\lambda}{2} b^{\alpha+z-2}(\nabla h)^2 + b^{-\alpha+\frac{z}{2}-\frac{d}{2}}\eta(x,t). \tag{1.41}$$

A problem occurs when we try to impose scale invariance on (1.41). The first term on the right hand side gives $z = 2$ but the second one gives $\alpha = 0$ that is inconsistent with $z = d + 2\alpha$. Even when the terms are scaled separately (it is expected that the non-linear term dominates over surface tension) the exponents are $\beta = 1/5$ and $\alpha = 1/3$. The reason the exponents do not match the ones of Ballistic Deposition is that when the system coordinates are rescaled the particle length $v\delta t$ introduced in the formula (1.38) scales as well. That means that the coefficient λ from the equation (1.37) has to be rescaled. Therefore, we cannot obtain the values of the scaling exponents through the change of variable (1.29), as we did for the Edwards-Willkinson equation. There is a variety of approximate analytical solutions and numerical simulations that provide the numerical values for the exponents of the KPZ equation, see Table 1.1,

KPZ	α	β	z
1D	$\frac{1}{2}$	$\frac{1}{3}$	$\frac{3}{2}$
2D	0.39	0.24	1.625

Table 1.1: Table of dynamical exponents for the KPZ equation in one and two dimensions. [1, 42–44].

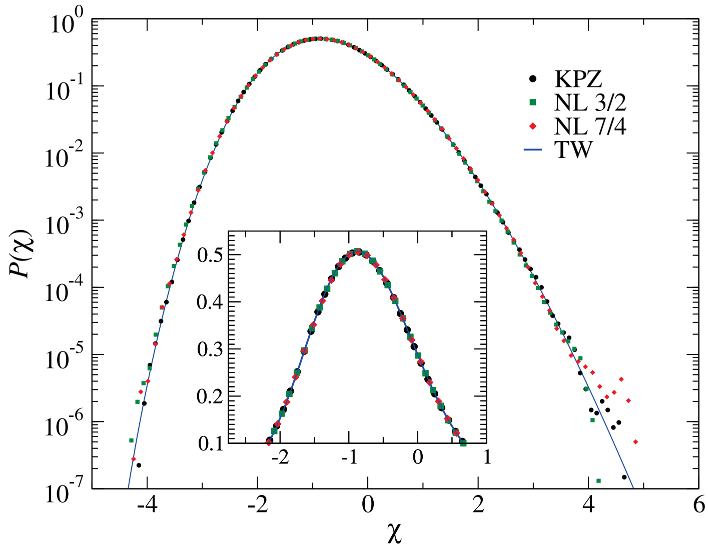

Figure 1.6: Numerical simulations in band geometry [51], show that the 1D KPZ height distribution matches the Tracy-Widom (GOE) distribution. NL 3/2 and 7/4 denote simulation data for other equations with the same statistics. *Inset:* Zoom of main panel.

Recently analytical solutions have been obtained for one dimensional KPZ interfaces with zero [45] or non-zero [26, 46] average curvature, where the statistics of height fluctuations at long times are described by the Tracy-Widom (TW) distribution [47] for the largest eigenvalue of random matrices in the Gaussian Unitary (GUE) or Orthogonal (GOE) ensembles, respectively, see Fig. 1.6. The idea came from [48, 49] where some growth models such as zero-temperature directed polymers in a random environment and the asymmetric simple exclusion process, were indeed shown to posses the TW largest-eigenvalue (GUE) distribution for the circular interfaces and the TW (GOE) distribution for flat interfaces [50]. In general the height function for systems described by the $1d$ KPZ equation can be written as [50–52]

$$h(x,t) \simeq v_\infty t + (\Gamma t)^{1/3}\chi \qquad (1.42)$$

where χ is a random amplitude whose statistics are those of the corresponding TW distribution, and v_∞ and Γ are constants. To be able to compare to other models we would have to get rid of any parameter dependence. Hence, we need to rescale the height in the following manner

$$h \to (h - v_\infty t)/(\Gamma t)^{1/3} \qquad (1.43)$$

The new rescaled height is a universal (time and parameter independent) variable described by the TW distribution. Here, the parameter Γ accounts for the relation between the roughness functions for different system sizes or noise strengths. Together with the deterministic growth velocity v_∞, it is usually determined numerically. One way to calculate it is to set the variance of the rescaled height to the variance of the TW-GOE distribution,

Figure 3. 1D height distributions for equation (1) (•) and equation (2) for $\mu = 3/2$ (■) and $\mu = 7/4$ (♦). The variable χ is defined in the text. The solid blue line is the TW (GOE) distribution expected for $d = 1$ [42]. $P(\chi)$ is estimated from 2048 independent runs starting from a flat initial condition. Inset: zoom of main panel, in linear representation. All units are arbitrary.

(compared with $\alpha_{KPZ}(2) \simeq 0.39$ [26]) and $z \simeq 1.61$, the smaller $\mu = 3/2 < 1.61$ system has the same exponent values as for $d = 1$! Recall that, for $\alpha_{KPZ}(1) \leq \mu < z_{KPZ}(2)$, the 2D exponents are non-KPZ [31], $z = \mu$, $\alpha = 2 - z$; moreover they are d-independent. Curiously enough, thus the $\mu = 3/2$ equation provides a peculiar example of a 2D system with 1D-KPZ exponents! Without the need of further characterization of height distributions[6] or correlation functions for this equation, this implies a change of its universality class as dimensionality increases from $d = 1$ to 2, while this is not the case for, for example, the $\mu = 7/4$ equation, which is still KPZ-like in 2D.

This fact has important consequences for the continuum modeling of systems, in particular of an experimental type, that are presumably in the KPZ universality class. Take the 1D case as an example. Equation (2) having the same symmetries as the KPZ equation, one might postulate the latter as a model description for a given experiment. But suppose the actual physical interactions lead to the occurrence of morphological instabilities (as happens only too often in surface growth experiments [28]), in such a way that a better

[6] In principle, the pseudo-spectral scheme we employed is known to outperform [44] the accuracy of the real space Euler algorithm used in [24] in reproducing a number of properties of the KPZ equation, like bare versus effective parameters, etc. Thus, it is interesting to compare the universal properties of $P(\chi)$ obtained through this scheme against previous estimates [24, 25]. As demonstrated in [25], the scaled cumulants g_n ($n \geq 1$) allow one to obtain universal quantities of $P(\chi)$, such as the ratios $R = g_2/g_1^2$, $S = g_3/g_2^{3/2}$ (skewness), and $K = g_4/g_2^2$ (excess kurtosis). For a 2D KPZ equation with parameters as in table 1, but $L = 1024$ and time $t^* = 250$, we obtain $g_1 = -1.149$, $g_2 = 0.4987$, $g_3 = 0.1578$, and $g_4 = 0.0941$, and universal ratios $R = 0.378$, $S = 0.448$, and $K = 0.378$, slightly larger (differences in the second or third significant digit) than those reported so far in the literature. This discrepancy can possibly be attributed to an incomplete convergence of the scaled cumulants for the chosen integration time t^*. A more accurate estimation of the height distribution for the 2D KPZ equation by means of the pseudo-spectral scheme is beyond the scope of this work, and will addressed in the future.

doi:10.1088/1742-5468/2013/11/P11001

which is $\langle \chi^2_{\text{GOE}} \rangle = 0.638$ [51]. Then, Γ can be obtained as

$$\Gamma = t^{-1} \frac{\langle h^2 \rangle}{\langle \chi^2_{\text{GOE}} \rangle}. \tag{1.44}$$

This is an important result, as it allows to compare not just the exponent values for a system, in order to check its universality class, but also higher order cumulants and compare them to the KPZ ones, as has been done for many continuum [51, 53, 54] and discrete models [55, 56], and experiments [57, 58].

1.5 Morphological Instabilities

This far, we have discussed systems whose surfaces evolve in time, described by the Langevin equation (1.13). Moreover, we have assumed scale-invariance that led to power-law behavior in the roughness and structure factor. However, in other cases, systems could be unstable to perturbations with certain wavelengths, or in an interval of wavelengths. This behavior usually leads to pattern formation [59] and it is seen in many experiments [60]. A well studied example is the (noisy) Kuramoto-Sivashinsky (KS) equation [59], similar to the KPZ Eq. (1.37), but just including an additional term

$$\frac{\partial h(\vec{r},t)}{\partial t} = -\nu \nabla^2 h(\vec{r},t) - K \nabla^4 h(\vec{r},t) + \frac{\lambda}{2} (\nabla h(\vec{r},t))^2 + \eta(\vec{r},t), \tag{1.45}$$

where $\nu, K > 0$. This equations describes directional solidification of dilute binary alloys [61], solidification of a pure substance at large undercooling including interface kinetics [62], sputtering by ion bombardment (IBS) [63], dynamics of steps on vicinal surfaces under MBE conditions [64, 65], etc. Crucially, the negative Laplacian introduces a competition between terms in this equation which give rise to unstable Fourier modes in the short time regime. To show this, we consider the Fourier transformed linearized KS equation which reads

$$\frac{\partial h_q}{\partial t} = \left[\nu q^2 - K q^4 \right] h_q + \eta(\vec{q},t), \tag{1.46}$$

The linear KS Eq. (1.46) has an analytical solution of the same form as the EW, given by Eq. (1.21), so that the structure factor is

$$S_q(t) = 2D \frac{e^{\omega_q t} - 1}{\omega_q}, \tag{1.47}$$

where the dispersion relation is $\omega_q = \nu q^2 - K q^4$. This function clearly differs from the EW dispersion relation, and is responsible for different dynamical behavior at linear time scales. At the very beginning of the evolution, $S_q \sim 2Dt$, there are still no space correlations so that the roughness function grows in time with a power-law where the growth exponent $\beta = 1/2$, same for the EW at early times and random deposition in general.

When the system develops significant space correlations the linear structure factor starts to depart form the EW solution. Unlike the EW dispersion relation where ω_q was strictly negative, here it contains an interval of wavelengths that provide positive solutions. Perturbing a surface with these wavelengths introduce unstable modes that grow exponentially in time while perturbations with wavelengths disappear if $\omega_q < 0$.

The dispersion relation of the linear KS equation reaches a maximum in the interval $q \in [0, \sqrt{\nu/K}]$ when $q_m = \sqrt{\nu/2K}$. In this fairly simple case the maximum is also the maximum of the structure factor, $\partial_q S_{q_m} = 0$. If the linear approximation describes well the system for later stages of the evolution, Fourier mode of the height with this wave-vector , h_{q_m}, as it grows exponentially faster than all other modes, will define a characteristic wavelength of the surface pattern. On a more general note, the maximum of the structure factor might not coincide with the maximum of the linear dispersion relation. This happens in systems where the noise variation depends on the wavelength, namely, $D(q)$ is a polynomial of q. For example, we consider the linear function, $D(q) = Dq$, which is especially important to us as this noise form is obtained after linearizing the stochastic lubrication equation [4, 17] (described in detail in Sec. 8.1). The maximum of the structure factor satisfies the relation

$$D\frac{q}{\omega_q^2}\left\{ 2\omega_q(e^{2\omega_q t} - 1) + q\partial_q\omega_q \left[e^{2\omega_q t}(2\omega - 1) + 1\right] \right\} = 0. \tag{1.48}$$

At early times, when $e^{2\omega t} - 1 \simeq 2\omega t$, the maximum growth wavelength, obtained from Eq. (1.48), depends on time as

$$q_m^2 \simeq \frac{\nu}{4K} + \sqrt{\frac{1}{8t}}. \tag{1.49}$$

The position of the main peak decreases in time from short length scales ($q \gg 1$) towards a fixed value, selected as the maximum of the dispersion relation. Therefore the characteristic wavelength of the generated pattern increases in time, and this process is called **coarsening** [66, 67]. In systems that undergo coarsening process the characteristic wavelength obeys the power-law, $q_m \sim t^n$, where in the described scenario, the KS with a conservative noise, the exponent is $-1/4$. A related coarsening exponent can occur for instance in the evolution of the average slope, which increases as a power-law of time, $m(t) = \langle \nabla h(\vec{r}, t)\rangle \sim t^p$ [60]. In general, different systems could display the same exponents (p, n), which characterize the universality class of coarsening. A more general classification of these universality classes is still under debate [60]. Non-trivial coarsening is usually related to non-linearities in the system, as they introduce correlations and mode coupling.

In systems that are unstable within linear regimes such as the KS system, the structure factor does not develop unstable nodes indefinitely. Due to significantly high slopes, at some point in the evolution the non-linear terms of the equation start to act, tending to smooth the surface and stabilize the behavior asymptotically. Specifically, in the case of the KS equation, the non-linear term is of the same as in the KPZ equation. Hence, the asymptotic behavior of the morphologically unstable KS equation displays scale invariance in the KPZ class [68, 69]. Actually, on scales much larger than the linear characteristic length $\lambda = 2\pi/q_m$, a disordered scale-invariant KPZ-like surface is observed, while reducing the scale to the characteristic one a regular pattern stands out.

2

FKPP traveling waves

The Fisher-Kolmogorov-Petrovsky-Piscunov (FKPP) equation is one of the most celebrated partial differential equations to describe reaction-diffusion systems and it has many applications in biology and chemical systems. The equation describes the invasion of a stable state into an unstable one, in real life describing e.g. how bacteria colonies move through a food source, or the spreading of advantageous genes [9, 11]. Such dynamics are mathematically represented by an interesting property of this equation to have a special class of solutions, traveling waves or fronts, whose form does not change in time but just travels in space. The deterministic dynamics of such systems have been studied in detail and our objective is to see how a more realistic case, which includes internal microscopic fluctuations, would affect the dynamics. Microscopic fluctuations can play an important role in the macroscopic behavior of reaction-diffusion (RD) systems. Although usually neglected in theoretical descriptions they can, for instance, give rise to instabilities [70], allow the system to reach new states which are not available in the deterministic description [7, 71], or produce spatial correlations which in turn dominate the macroscopic system behavior [72, 73]. This is particularly true at onset for transitions from metastable or unstable phases, in which microscopic noise due to thermal or density fluctuations can be amplified to macroscopic time and length scales [74, 75]. A prominent context, both from the experimental and from the theoretical points of view, is provided by front propagation in RD systems, as in the invasion of an unstable phase by a stable one [76]. As stated above, for deterministic systems (where the number of particles in the system is large but finite), this is paradigmatically described by the FKPP equation [9–11].

In this Chapter we give a brief overview on how reaction-diffusion processes are

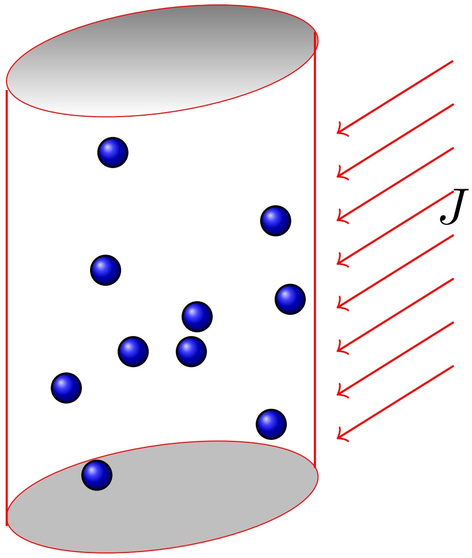

Figure 2.1: Particles inside an arbitrary volume.

modeled. Then we introduce the Fisher-Kolmogov equation as a mean-field approximation derived from reaction-diffusion death-birth processes, together with some basic properties of the solutions. A correction due to the discrete nature of these microscopic processes leads to the same FKPP equation, just with an additional stochastic term that represents density fluctuations. Finally we will present some of the important results that inspired us to study such systems.

2.1 Introduction to the FKPP equation

2.1.1 Reaction-diffusion processes

Reaction-diffusion processes describe many physical systems in which a field, such as a concentration or temperature, changes in space and time, dynamics being frequently described by partial differential equations. To derive the equation that describes changes in space and time of e.g. concentration in some domain we will consider an arbitrary volume V which is enclosed by surface S, see Fig. 2.1. The change of the concentration field in time depends on the flux, J, across the surface S, which represents the number of particles that enter (exit) the domain per unit time and unit surface. Moreover, particles can be created or annihilated as a consequence of e.g chemical reactions, hence we have to introduce the rate of creation or annihilation of particles inside the volume. If we define $\rho(x, t)$ to be the concentration field of particles we can express the change of concentration in time as

$$\frac{\partial}{\partial t}\int_V \rho(x,t)dv = -\int_S Jds + \int_V f dv, \tag{2.1}$$

where J represents the flux through the surface S within which the volume V is bounded and f is the rate of creation or annihilation of particles, also known as reaction kinetics [11], as will be used in this work. The concentration is assumed to be a continuous function, which for small number of particles is far from a good approximation. Describing the concentration as a discrete function is an improvement that leads to a noise term, which will be explained in detail for the case of the FKPP equation in Sec. 2.2. Coming back to Eq. (2.1), if we apply Gauss-Ostrogradsky formula to the flux term we get

$$\int_S Jds = \int_V \nabla J dv,$$

hence we can rewrite Eq. (2.1) as

$$\int_V \left[\frac{\partial \rho(x,t)}{\partial t} + \nabla J - f\right] dv = 0. \tag{2.2}$$

The form of the flux J requires a model. It certainly depends on the material properties and inter-molecular forces. One of the simplest and widely used forms is the classical diffusion process, known as Fickian diffusion [11], whereby mass diffuses from higher to lower density regions. Therefore the current J is modeled as a gradient,

$$J = -D\nabla\rho(x,t), \tag{2.3}$$

where D is the diffusion constant which depends on the properties of the material. Introducing the gradient (2.3) into Eq. (2.2) and, due to the fact that V is an arbitrary volume, we have:

$$\frac{\partial \rho(x,t)}{\partial t} = \nabla D \nabla \rho(x,t) + f. \tag{2.4}$$

In the simplest approximation the diffusion coefficient D does not change in space, so that Eq. (2.4) becomes

$$\frac{\partial \rho(x,t)}{\partial t} = D\triangle\rho(x,t) + f. \tag{2.5}$$

The simplest case in which there is no reaction kinetics, $f = 0$, is called simple diffusion. On the other hand, there are forms of the reaction term which, together with the diffusion term, describe dynamics where the shape of the solution does not change in time, except for a coherent displacement along a given direction. Such solutions are called traveling wave solutions. In general, for a one-dimensional system described by Eq. (2.5), these kind of solutions are assumed to move at speed c, which provides a relation between time and space coordinates, namely

$$\rho(x,t) = \rho(x-ct). \tag{2.6}$$

Introducing the variable $z = x - ct$, the time derivative can be written as

$$\frac{\partial \rho(x,t)}{\partial t} = -c\frac{d\rho(z)}{dz},$$

and the space derivative is

$$\frac{\partial^2 \rho(x,t)}{\partial x^2} = \frac{d^2\rho(z)}{dz^2}.$$

By the assumption that the function is a traveling wave, the partial differential equation in (2.5) becomes an ordinary differential equation,

$$c\frac{d\rho(z)}{dz} + D\frac{d^2\rho(x,t)}{dz^2} + f = 0. \tag{2.7}$$

For example, in the case of simple diffusion ($f = 0$) this leads to

$$\rho(z) = A + Be^{-\frac{c}{D}z}, \tag{2.8}$$

where A and B are constants to be determined from the initial and boundary conditions. The traveling wave solution is bounded for every z, hence B has to be zero. Then, ρ is a constant and is not a proper traveling wave. Therefore, the existence of traveling wave solutions, as a property of certain physical systems, strictly depends on the kinetic reaction term.

2.1.2 The FKPP equation

Processes that are frequently described well by the FKPP equation are chemical reactions, in which particles are predominantly transported by thermal diffusion. We will first describe some of these processes that lead to the FKPP equation, in order to motivate the importance of this model.

Describing a chemical reaction in detail is often impossible. In general, what we could do is split the process into steps and ignore everything that happens between the steps. In this way we will certainly lose some information that influences the next state of the system, but at least we will be able to predict the evolution of the system approximately. As far as a chemical reaction is concerned, a state can be described by the number of particles in the system, and we aim to build a model that explains the change of the particle number in time, using as little information as possible.

In chemical reactions, atom and molecular species are usually represented by capital letters A, B, C, etc. and the chemical reaction is usually presented in terms of creation or annihilation of certain particle species (death-birth processes). In this way we do not take into account the full nature of the chemical processes, which simplifies the model

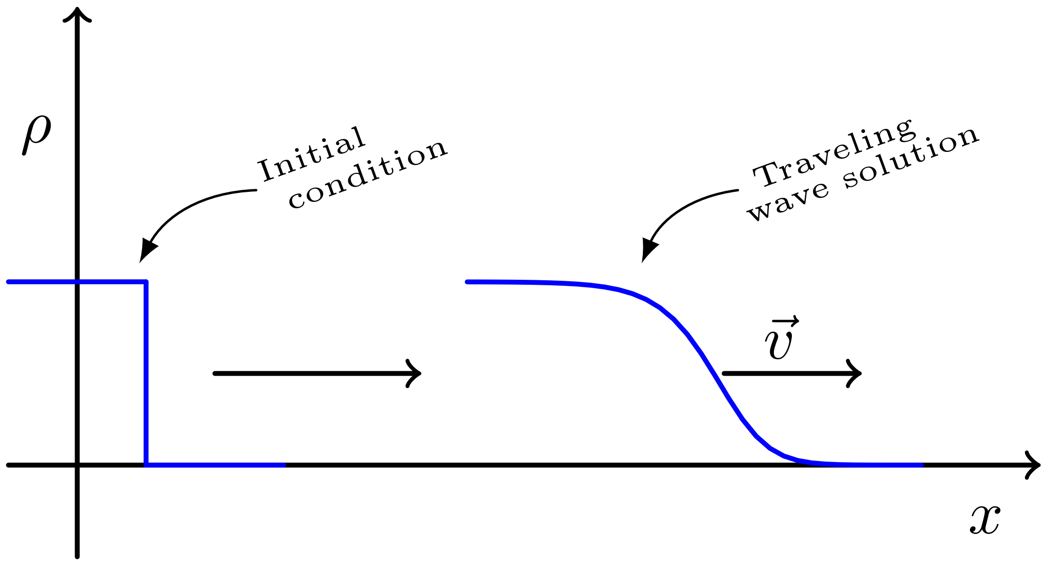

Figure 2.2: From a steep enough initial condition, a traveling wave solution is formed. We always use (unless stated otherwise) the step function as an initial condition for the density ρ.

and makes it easier to simulate the time evolution of the system. Consider now a system described by the following processes [12]:

$$\begin{aligned} A &\to 2A && \text{decoagulation,} \\ 2A &\to A && \text{coagulation.} \end{aligned} \tag{2.9}$$

The first reaction is also called offspring production and the second coalescence. One way to model these types of reactions is to use mean field theory. Basically, we assume that the particles are homogeneously distributed in space and that the rate of a reaction for a given temperature is proportional to the product of concentrations of the reaction species. Assuming that the frequency rate k, in the mean field approximation decoagulation occurs with a frequency coagulation proportional to $k_1\rho(x,t)$. The same approximation of the coagulation leads to a frequency proportional to $k_2\rho^2(x,t)$. Finally we can write down the rate of change of the concentration, caused by both coagulation and decoagulation processes, as

$$\partial_t \rho(x,t) = k_1\rho(x,t) - k_2\,\rho^2(x,t), \tag{2.10}$$

where the negative sign reflects the loss of particles due to coagulation. The kinetic reaction term $f = k_1\rho - k_2\rho^2$ was proposed by Fisher [9] to describe the spreading of advantageous genes in a population. With this term the reaction-diffusion equation we want to study is:

$$\frac{\partial \rho(x,t)}{\partial t} = D\triangle\rho(x,t) + k_1\rho(x,t) - k_2\rho^2(x,t). \tag{2.11}$$

Eq. (2.11) is just a mean-field continuum description of the process (2.9). A more realistic description can be achieved just by adding a noise term [77], which will be discussed in the next section.

For now, to simplify the notation without loosing generality we will use $k_1 = k_2 = 1$. Eq. (2.11) is named after Fisher, Kolmogorov, Petrovsky and Piscunov due to the analytical results that Kolmogorov, Petrovsky and Piscunov obtained trying to solve it [10]. He found the kind of initial conditions for which a traveling wave solution will occur. Namely if $\rho(x,0) = \rho_0(x) \geq 0$, so that

$$\rho_0(x) = \begin{cases} 1 & \text{if } x \leq x_1 \\ 0 & \text{if } x \geq x_2, \end{cases} \tag{2.12}$$

where $x_1 < x_2$, and $\rho_0(x)$ is continuous in the interval $[x_1, x_2]$, then $\rho(x,t)$ evolves to a traveling wave solution. For different initial conditions, the solution could be completely different and does not have to be of the traveling wave form. In order to have traveling waves, we always use the step function as an initial condition for $\rho(x,t)$, see Fig. 2.2. Especially important is the initial value of the function ρ at both ends of the interval, when $x \to \pm\infty$.

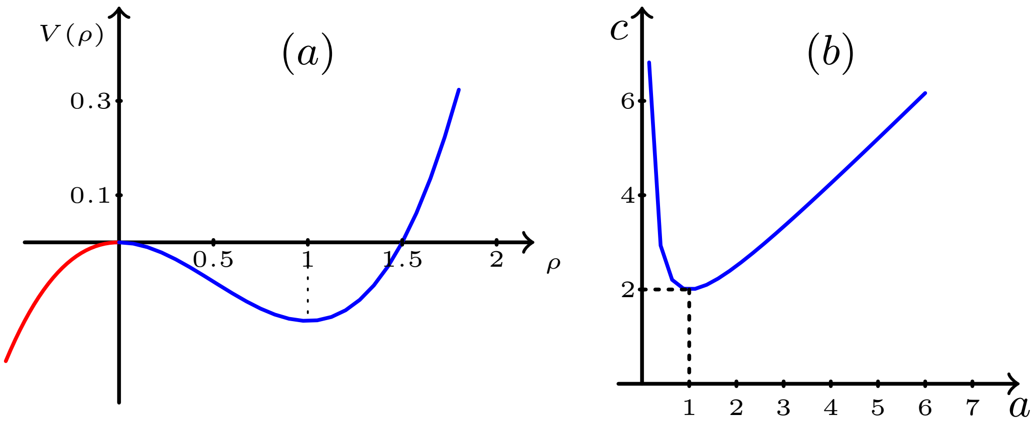

Figure 2.3: (a) The potential function of the Fisher reaction term displaying an unstable $(x = 0)$ and a stable state $(x = 1)$. The red part of the curve $(\rho < 0)$ is physically irrelevant. (b) Velocity potential (2.26) for a dimensionless $(D = 1)$ Fisher equation.

Once the traveling wave solution forms, it travels at the minimum velocity $v = 2\sqrt{D}$ [7, 11, 75]. This type of solutions are called *pulled* fronts [6]. Their main property is that the minimal velocity can be found by linearizing Eq. (2.11). This basically means that the leading edge ($\rho \sim 0$) is responsible for the dynamics of such systems. Unlike *pulled* fronts, *pushed* [78] fronts are determined by nonlinearities and their velocity is always larger than the minimal one. Physically, they connect metastable states, while *pulled* fronts invade unstable states. Different regions of density determine the velocity of *pulled* and *pushed* fronts. Although the behavior could be similar, perturbations could affect the dynamics in completely different manners.

The minimal velocity can be obtained in the following way. First, to simplify notation we introduce the change of variable $x^* = xD^{-1/2}$. In one-dimensional space Eq. (2.11) becomes

$$\frac{\partial \rho(x^*, t)}{\partial t} = \frac{\partial^2 \rho}{\partial x^{*2}} + \rho - \rho^2. \tag{2.13}$$

Due to the form of the reaction potential energy ($-\partial_\rho V = f$, and $V(\rho) = \rho^3/3 - \rho^2/2$), it is easy to see that there are two steady states $\rho = 0$ and $\rho = 1$ which are, respectively, unstable and stable, see Fig. 2.3. Therefore, we expect our solution to be a traveling wave that diffuses from the unstable to the stable state. Now, if we apply a change of variables as in Eq. (2.6), $z = x - ct$, our equation becomes an ordinary differential equation:

$$\rho'' + c\rho' + \rho - \rho^2 = 0. \tag{2.14}$$

We will assume that at one end of the interval the concentration is in the stable state, while it is in the unstable state at the other end. We can study function ρ in the (ρ, ρ_1) plane, where $\rho_1 = \rho'$, hence we rewrite Eq. (2.14) as

$$\frac{\partial \rho_1}{\partial \rho} = \frac{-c\rho_1 - \rho + \rho^2}{\rho_1}. \tag{2.15}$$

Again, we have two singular points, $(0, 0)$ and $(1, 0)$, which correspond to the unstable and stable solutions, respectively. Both numerator and denominator of Eq. (2.15) are zero at these singular points, while we expect the solution to be analytic around these points, so that we can expand it in a Taylor series. Then, we only need the linear term to discuss how the function behaves. For the point $(0, 0)$, we rewrite Eq. (2.15) in an equivalent form:

$$\frac{d\rho_1}{dz} = -c\rho_1 - \rho, \qquad \frac{d\rho}{dz} = \rho_1. \tag{2.16}$$

We have a coupled system of equations and we can again rewrite it in matrix form

$$\begin{pmatrix} \frac{d\rho_1}{dz} \\ \frac{d\rho_1}{dz} \end{pmatrix} = \begin{pmatrix} -c & -1 \\ 1 & 0 \end{pmatrix} \begin{pmatrix} \rho_1 \\ \rho \end{pmatrix}. \tag{2.17}$$

To decouple the equations, we solve the eigenvalue problem

$$\begin{pmatrix} c - \lambda_i & -1 \\ 1 & -\lambda_i \end{pmatrix} \begin{pmatrix} v_{1i} \\ v_{2i} \end{pmatrix} = \begin{pmatrix} 0 \\ 0 \end{pmatrix}, \tag{2.18}$$

obtaining the eigenvalues

$$\lambda_\pm = \frac{1}{2}\left[-c \pm \sqrt{c^2 - 4}\right], \tag{2.19}$$

which correspond to the eigenvectors

$$\vec{v}_\pm = \frac{1}{\sqrt{1 + (c - \lambda_\pm)^2}} \begin{pmatrix} 1 \\ c - \lambda_\pm \end{pmatrix}. \tag{2.20}$$

Hence the solution of the system of equations (2.16) is

$$\begin{pmatrix} \rho_1 \\ \rho \end{pmatrix} = c_+ \vec{v}_+ e^{\lambda_+ z} + c_- \vec{v}_- e^{\lambda_- z}. \tag{2.21}$$

We see that for, $c < 2$, the eigenvalues are complex numbers and the solution oscillates around the origin. Depending on the value of λ, it can follow different trajectories in space phase such as stable and unstable spirals or ellipses. On the other hand, for $c \geq 2$ both values of λ are negative and all solutions tends to $(0, 0)$ when $z \to \infty$ along the directions $\vec{v}_+$ and $\vec{v}_-$, hence the point $(0, 0)$ is stable. These kind of singularity is called a stable-node.

At the singular point $(\rho, \rho_1) = (1, 0)$, we shift ρ through the change of variable $\rho = \rho' - 1$, so that the singular point becomes $(0, 0)$ again. Now, Eq. (2.15) becomes

$$\frac{d\rho_1}{d\rho'} = \frac{-c\rho_1 + \rho' + \rho'^2}{\rho_1}, \tag{2.22}$$

so that the matrix equation reads

$$\begin{pmatrix} -c - \lambda_i & 1 \\ 1 & -\lambda_i \end{pmatrix} \begin{pmatrix} v_{1i} \\ v_{2i} \end{pmatrix} = \begin{pmatrix} 0 \\ 0 \end{pmatrix}. \tag{2.23}$$

Repeating all the steps we took for the first singular point, we obtain the eigenvalues

$$\lambda_\pm = \frac{1}{2}\left[-c \pm \sqrt{c^2 + 4}\right]. \tag{2.24}$$

Both eigenvalues are real, but they have different signs, $\lambda_+ > 0$ and $\lambda_- < 0$. When $z \to \infty$, the first term of the solution (2.21) tends to $(0, 0)$ while the other one tends to infinity. Therefore, the point $(0, 1)$ is a saddle point. Finally, it can be shown that for every $c \geq 2$ there is a curve in the phase plane (ρ_1, ρ) that connects $(0, 0)$ and $(1, 0)$, such that $\rho > 0$. This holds for the rescaled FKPP equation (2.13), hence if we rescale back we get

$$c \geq 2\sqrt{D}, \tag{2.25}$$

namely, the minimal speed depending on the diffusion coefficient [11].

As mentioned above, the minimal speed can be also obtained by linearizing Eq. (2.11) and introducing the variable $z = x - ct$, where c is the expected velocity of the front. The equation can be solved analytically in the region of small ρ ($\rho \gg \rho^2$), where the solution is expected to decay exponentially $\rho(z) \sim e^{-az}$. Now, if such a solution is introduced back into the linearized equation, we obtain the relation for the velocity

$$c = Da + \frac{1}{a}, \tag{2.26}$$

where the minimum is at $c = 2\sqrt{D}$, see Fig. 2.3. The exponential decay of the solution will be considered in the next sections, in which fluctuations play an important role.

2.2 Introduction to the stochastic FKPP equation

As was mentioned in Sec. 2.1.1, the whole process of constructing a PDE to describe reaction-diffusion systems is followed under the assumption that the function that describes the dynamics (like the concentration or density) is continuous in space and time. Systems described by the FKPP equation are usually microscopic and at certain length scales they are completely discrete. However, this fact can be taken into account by introducing a noise term which converts a PDE into a stochastic PDE (more details in [79]). First, we will motivate the introduction of the correct noise term and then a more rigorous proof will be provided.

2.2.1 Heuristic approach

The stochastic FKPP model can be derived from the kinetic reactions seen as stochastic random processes. Let us assume that there are n_t particles in a given volume V at a given time t. The reaction term is the same as in Sec. 2.1.2, just the concentration function can not be assumed to be continuous. Particles reproduce at some rate k_1' ($A \to 2A$ process) and an interaction between two particles results into annihilation of one of them ($A + A \to A$ process) which happens at rate k_2'. Note that in Sec. 2.1.2 the rates were representing concentration change, while here the change is in the number of particles. After a time interval Δt, the new number of particles ϵ is a random number extracted from the Poisson distribution

$$P(\lambda, \epsilon) = \frac{\lambda^\epsilon}{\epsilon!} e^{-\lambda}, \tag{2.27}$$

so that the total number of particles at the next time step $t + \Delta t$ is

$$n_{t+\Delta t} = n_t + \epsilon \Delta t. \tag{2.28}$$

The mean value of the Poisson distribution (2.27) is λ. The mean actually corresponds to the average number of particles of the birth-death process, thus we have

$$\lambda = k_1' n_t - k_2' n_t^2. \tag{2.29}$$

For relatively large λ, the Poisson distribution can be well approximated by the Gaussian distribution, $P(\lambda, \epsilon) = \mathcal{N}(\epsilon; \mu = \lambda, \sigma^2 = \lambda)$. Now Eq. (2.28) can be rewritten as

$$\frac{n_{t+\Delta t} - n_t}{\Delta t} = k_1' n_t - k_2' n_t^2 + \sqrt{k_1' n_t - k_2' n_t^2}\, \eta, \tag{2.30}$$

where η, is a normal-distributed random number with zero mean and unit variance,

$$\begin{aligned} \langle \eta(x,t) \rangle &= 0, \\ \langle \eta(x,t) \eta(x',t') \rangle &= \delta(x - x')\delta(t - t'). \end{aligned} \tag{2.31}$$

In the limit $\Delta t \to 0$ and dividing everything by the volume V, we obtain

$$\frac{\partial \rho}{\partial t} = k_1\rho - k_2\rho^2 + \sqrt{\frac{k_1\rho - k_2\rho^2}{V}}\,\eta, \tag{2.32}$$

so that $k_1' = k_1$ and $k_2' = Vk_2$. Note that k_1 and k_2 are the same rates as in Sec. 2.1.2 and again for simplicity we use $k_1 = k_2 = 1$. Also, the concentration ρ is normalized so that $N \sim V$. If we let the system diffuse, we finally obtain the stochastic Fisher-Kolmogorov-Petrovsky-Piscounov (sFKPP) equation [70]

$$\frac{\partial \rho}{\partial t} = D\triangle\rho + \rho - \rho^2 + \sqrt{\frac{\rho - \rho^2}{N}}\,\eta. \tag{2.33}$$

2.2.2 Detailed derivation

Any chemical process changes the value of the concentration (density) every time reactions occur. A finite particle system can be represented by a birth-death process as done when the FKPP equation was introduced. Here we will not apply the mean field approach but we will rather describe these processes in full through a master equation like (for more details see [2], Chapter 5D). We assume that at position i on a grid we have n_i particles so that the total number of particles is $N = \sum n_i$ and the concentration is $\rho_i = n_i/V$. Then for the creation process $A \to 2A$ that takes place at a rate k_1' we can write down master equation that expresses the change in the probability $P(n_i, t)$ of having n_i particles at time t through the probability of having $n_i - 1$ particles minus the probability of having n_i particles at time t, so that the equation is

$$\frac{\partial P(n_i;t)}{\partial t} = \frac{k_1'}{V}(n_i - 1)P(n_i - 1;t) - \frac{k_1'}{V}n_i P(n_i;t). \tag{2.34}$$

The annihilation process, $2A \to A$ at rate k_2' leads to

$$\frac{\partial P(n_i;t)}{\partial t} = \frac{k_2'}{V}(n_i + 1)n_i P(n_i + 1;t) - \frac{k_2'}{V}(n_i - 1)n_i P(n_i;t). \tag{2.35}$$

A process that leads to the stochastic FKPP equation is the combination of two more general reactions, $A + B \to A + A$ at rate k_1', and $A + B \to B + B$ at rate k_2'. It was demonstrated in [77, 80] that these processes and the processes $A \to 2A$ and $2A \to A$ are described by the same master equation. We assume that the reaction preserves the total particle number $N = N_A + N_B$. Combining the annihilation and creation processes for species A, we obtain the master equation

$$\frac{\partial P_n(t)}{\partial t} = \frac{k_1'}{V}(n-1)P_{n-1} - \frac{k_1'}{V}nP_n - \frac{k_2'}{V}\frac{n(n-1)}{2}P_n + \frac{k_2'}{V}\frac{n(n+1)}{2}P_{n+1}. \tag{2.36}$$

A fundamental result of stochastic processes is that a diffusion process can always be approximated by a jump process and not otherwise [81, 82]. Therefore, using van Kampen's system size expansion, Eq. (2.36) can be approximated by the Fokker-Planck equation

$$\frac{\partial P(\rho,t)}{\partial t} = -\frac{(k_1' - k_2')N}{V}\frac{\partial}{\partial \rho}\rho(1-\rho)P(\rho,t) + \frac{1}{2}\frac{k_1'+k_2'}{V}\frac{\partial^2}{\partial \rho^2}\rho(1-\rho)P(\rho,t). \quad (2.37)$$

Using the associated Fokker-Planck equation [79] to Eq. (2.37), we find a stochastic differential equation of the form:

$$\frac{\partial \rho(t)}{\partial t} = \gamma\rho(1-\rho) + \sigma\sqrt{\rho-\rho^2}dW, \quad (2.38)$$

where

$$\gamma = (k_1' - k_2')\frac{N}{V} \quad \text{and} \quad \sigma^2 = \frac{k_1'+k_2'}{V}.$$

In the thermodynamic limit $N \to \infty$ and $V \to \infty$ such that $N \sim V$ and the noise is weak $\sigma \sim 1/\sqrt{N}$ [77]. The right hand side of Eq. (2.38) actually represents a reaction kinetic term for a reaction-diffusion equation. For the spatially homogeneous processes $A \to 2A$ and $2A \to A$, adding the diffusion term we finally obtain the reaction-diffusion equation

$$\frac{\partial \rho(t)}{\partial t} = D\triangle\rho + \gamma\rho(1-\rho) + \sigma\sqrt{\rho-\rho^2}\,\eta(x,t), \quad (2.39)$$

which is again the stochastic Fisher-Kolmogorov-Petrovsky-Piscounov equation (sFKPP) [10]. Here, $\eta(x,t)$ is a normal-distributed random number with zero mean and unit variance, see Eq. (2.31). For an infinite number of particles, the sFKPP equation becomes the FKPP equation. We already mentioned that the leading edge (where $\rho \simeq 0$) drives the wave solution of the FKPP equation, so any small fluctuations in the front of the wave can severely influence the dynamics. Therefore, we leave only the linear power of ρ in the noise term and rewrite Eq. (2.39) as

$$\frac{\partial \rho}{\partial t} = D\triangle\rho + \rho(1-\rho) + \sigma\sqrt{\rho}\,\eta(x,t), \quad (2.40)$$

where in the case of the chemical process $A \to 2A$ and $2A \to A$ we define $\sigma = N^{-\frac{1}{2}}$. Therefore the fluctuations strength actually depends on the number of particles in a system. The more particles are present the weaker the noise is which is, expected as the density becomes approximated better by a continuous function. In any case, fluctuations can not be neglected as no matter how small the noise strength is, they will affect the dynamics of the traveling waves, as will be studied in detail in the following Sections and Chapters.

2.3 Stochastic traveling waves

Adding the stochastic term to the FKPP equation hinders the applicability of some of the analytical tools seen in the previous sections. There have been many works describing the influence of stochasticity into the dynamics of traveling waves. One of the crucial results is the change in the velocity, given by Brunet-Derrida formula [7] which we discuss below, together with additional results on two dimensional fronts which motivated us to try to provide a better explanation of the dynamics occurring in the sFKPP systems.

2.3.1 Velocity of the sFKPP traveling waves: Brunet-Derrida formula

In their work [8], Brunet and Derrida investigated how a small cutoff in the traveling wave solution affects the velocity of the FKPP front (given in Sec. 2.1.2) in one dimensional systems. Namely, they assumed that the number of particles is an integer number so that the concentration can not be smaller than the concentration of a single particle in the volume. They introduced a small number ϵ below which the concentration identically becomes zero. The idea was to introduce a cutoff function which limits the reaction term in the FKPP equation,

$$\frac{\partial h}{\partial t} = \frac{\partial^2 h}{\partial x^2} + (h - h^2)a(h), \tag{2.41}$$

where a is the cutoff function so that

$$a(h) = \begin{cases} 1 & \text{if} \quad h > \epsilon \\ 0 & \text{if} \quad h < \epsilon. \end{cases} \tag{2.42}$$

Simulating Eq. (2.41) numerically, Brunet and Derrida, showed that the velocity of the traveling wave depends on the cutoff parameter ϵ as

$$v_{\text{cutoff}} = v_0 - \frac{C}{\ln^2 \epsilon}, \tag{2.43}$$

where v_0 represents the velocity of the continuum model (without cutoff), constant C was found to be $C \sim \pi$, and N represents the total number of particles per unit volume, such that $\epsilon = 1/N$. They also confirmed the result by simulating a discrete stochastic model [83]. Different numerical algorithms [84, 85], described in Chapter 3, confirmed the validity of the Brunet-Derrida formula (2.43). A phenomenological explanation for the correction term was given in [86], by showing that the correction is

$$v - v_0 - \frac{C}{\ln^2 N} = O\left(\frac{\ln \ln N}{\ln^3 N}\right), \tag{2.44}$$

where v is the velocity of a stochastic front. Finally, the Brunet-Derrida formula together with the correction has been rigorously proved by Muller, Mytnik and Quastel in [87].

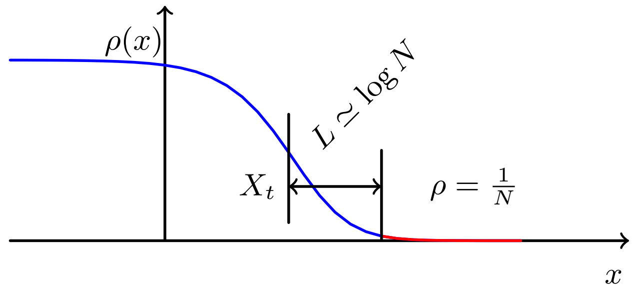

Figure 2.4: Typical solution of the FKPP equation. The Brunet-Derrida cutoff theory sets the concentration to zero for concentration values smaller than $1/N$, the red part of the curve.

The most important implication of the Brunet-Derrida formula is that, no matter how small the number of particles is, the noise will still significantly change the velocity of the front, due to the slow decay of the correction $1/\ln^2 N$ for $N \gg 1$. All the conclusions made come from the analysis of the particle model [88], and not the sFKKP equation, although the conclusions hold for the latter as well. The idea of Ref. [86] inspired us since it suggests the existence of correlations between the macroscopic and microscopic regions of the front. Therefore the basic ideas will be presented here.

Unlike deterministic Fisher fronts, stochastic ones have *compact support* [89]. If the initial solution is stable ($\rho = 0$) for $x \geq b$ and unstable ($\rho = 1$) for $x \leq a$, such that $-\infty < a < b < \infty$, then at any time t there will be $a(t)$ and $b(t)$ such that for $-\infty < a(t) < b(t) < \infty$, we have that $\rho(x < a(t)) = 1$ and $\rho(x > b(t)) = 0$. Moreover, in the large time limit the function $b(t)$ will grow linearly. This is an important difference with respect to deterministic Fisher fronts, where $b(t)$ instantly becomes infinity due to the exponential form of the solution. The *compact-support property* provides a justification for the cut-off theory and other works [75, 90].

If the number of particles is really large, the noise does not play any role around the "macroscopic" front position, where $\rho \sim 1/2$. Then the only influence noise could have is at the tip of the front where $\rho \sim 1/N$. The phenomenological approach of Brunet and Derrida is based on the following facts. Sufficiently strong fluctuations create particles at a distance δ ahead of the tip of the front (where ρ reaches zero). In that region the density grows exponentially [$\rho \sim exp(-az)$, see Sec. 2.1.2] resulting into a slowing-down of the diffusion processes. The non-zero value of δ will produce a change in the front position in a neighborhood of size $R(\delta)$. The probability distribution for particle creation at a distance δ, is supposed to be exponential due to the exponential decay of the deterministic solution,

$$p(\delta)d\delta \sim e^{-a\delta}d\delta. \tag{2.45}$$

The position of the front is affected by these random particle creations, only when they actually happen, so that the front position X_t is

$$X_{t+\delta t} = \begin{cases} X_t + v_{\text{cutoff}}\Delta t + R(\delta), & \text{with prob. } P(\delta) = \frac{\delta t}{\tau} p(\delta) d\delta, \\ X_t + v_{\text{cutoff}}\Delta t, & \text{with prob. } 1 - \int_{\delta_0}^{\infty} \frac{\delta t}{\tau} p(\delta) d\delta, \end{cases}$$

where $P(\delta)$ is the probability of a relevant fluctuation during the time Δt and v_{cutoff} is the predicted velocity given by the formula (2.43). Fluctuations will produce relevant changes in the front position only for δ values larger than some δ_0. Here, τ is the typical time lapse between two relevant fluctuations. Then, the change in the averaged position is

$$\partial_t \ln\langle e^{\lambda X_t}\rangle = \lambda v_{\text{cutoff}} + \frac{1}{\tau}\int p(\delta)[e^{\lambda R(\delta)} - 1]d\delta. \tag{2.46}$$

Calculating the average in this way allows us to calculate all cumulants by expanding the equation into a power series of λ. The first-order contribution provides the correction of the velocity

$$v - v_{\text{cutoff}} = \frac{1}{\tau}\int p(\delta)R(\delta)d\delta, \tag{2.47}$$

where v is the velocity of a stochastic front. Now, the problem is how to calculate the function $R(\delta)$. The exponential decay of the function $p(\delta)$ was intuitive, but for $R(\delta)$ one has to argue using numerical predictions. As already shown in the simulations of [90, 91], the relaxation time scales as L^2, where L denotes distance between the front ($\rho \sim 1/2$) and the tip ($\rho \sim 1/N$) position, see Fig. 2.4. +Due to the exponential shape of the solution and the predicted probability $p(\delta)$, Brunet and Derrida postulated the relation between the particles created ahead of the tip of the front and the change they produce in the macroscopic part of the front, as

$$R(\delta) = \frac{1}{a}\ln\left(1 + C\frac{e^{a\delta}}{L^3}\right). \tag{2.48}$$

Implementing this relation back into the integral (2.47), we obtain the correction term as a function of L,

$$v - v_{\text{cutoff}} \sim \frac{1}{a}\frac{\ln L}{L^3}. \tag{2.49}$$

From $h(X_t + L, t) = 1/N$ one easily finds that $L \sim \ln N$, see Fig. 2.4. This result is rigorously proved in [87].

The phenomenological theory gives a good description of the mechanisms that slow down the front. Strong enough fluctuations happen from time to time and affect the velocity of one-dimensional fronts. The question that arises is how the dynamics of two-dimensional fronts evolve in time when fluctuations are accounted for and what mechanisms define the morphology of such fronts. These questions are the main topic of the research on Fisher fronts presented in this thesis, hence some previous results will be presented in the next section.

2.3.2 Stochastic traveling waves in 2d

The interesting effect that fluctuations produce by slowing down $1d$ traveling waves becomes even more interesting in $2d$, where a non-trivial surface morphology occurs for the front. Here we present two arguments to establish the universality class of the sFKPP morphology.

In one dimensional systems we were following the motion of a point on the sFKPP wave solution (usually $\rho = 1/2$) in order to study the dynamics of this type of fronts. In two dimensions, that point extends to an equipotential curve, which is completely straight for all times if the system is deterministic and the initial condition is a step function $[\rho(x, y, t_0) = \Theta(x)]$. When fluctuations are present the curve becomes rough, inducing non-trivial morphology of the wave, see Fig. 2.5. Unfortunately predicting the morphology is not a trivial task due to the lack of analytical tools to deal with the problem. One of the ways to approach it is to find similarities between the sFKPP surface and well known and studied surface growth models. In Ref. [92] an attempt was made to assign the KPZ [34] universality class [1] (described in detail in Sec. 1.4) to the sFKPP equation. Specifically, an equation similar to sFKPP (just with a different noise term) was analytically transformed into the KPZ equation, and then the result was generalized for various noise terms including the one from the sFKPP equation.

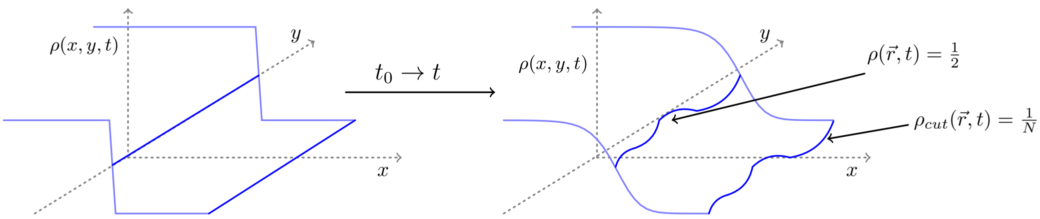

Figure 2.5: Stochastic Fisher front shape developed from a step function initial condition, where solid blue lines represent equipotential lines $\rho = 1/2$ and $\rho = 1/N$. In deterministic systems both lines remain flat.

As a result, a **conjecture** is formulated in [92]: Fisher waves in $d + 1$ dimensions (d-space dimension, and 1- time dimension), propagating into an unstable state belong to the $(d + 1) + 1$ dimensional KPZ universality class, even though the front is described by a d dimensional interface.

The conjecture was proved for a special case of two-dimensional *pulled fronts* systems, described by the FKPP equation with multiplicative noise,

$$\frac{\partial \phi}{\partial t} = D\nabla^2\phi + \phi - \phi^2 + \phi\eta, \tag{2.50}$$

where $\phi = \phi(x, y, t)$. This equation was suggested to describe stochastic growth models in the universality class of the **Reggeon** field theory [41]. The important region for the dynamics in (2.50) is at the tip of the front ($\phi \sim 0$), where the quadratic term can be neglected. We introduce the change of variables

$$\begin{aligned} &\epsilon = x - vt, \qquad dx = d\epsilon, \\ &y' = y \\ &t' = t, \qquad dt = -\frac{1}{v}d\epsilon + dt', \end{aligned} \tag{2.51}$$

and define $\phi = e^{-\lambda\epsilon}\psi(\epsilon, y', t')$, where coefficients λ and v are well-known from the deterministic Fisher equation:

$$\lambda = \frac{1}{\sqrt{D}} \qquad \text{and} \qquad v = 2\sqrt{D}.$$

Now we rewrite Eq. (2.50), and for simplicity we drop primes, so that

$$\left(-v\frac{\partial}{\partial\epsilon} + \frac{\partial}{\partial t}\right) e^{-\lambda\epsilon}\psi = D\left(\frac{\partial^2}{\partial\epsilon^2} + \frac{\partial^2}{\partial y^2}\right) e^{-\lambda\epsilon}\psi + e^{-\lambda\epsilon}\psi + e^{-\lambda\epsilon}\psi\eta \tag{2.52}$$

Rewriting this equation and eliminating the term $e^{-\lambda\epsilon}$ we obtain

$$\frac{\partial\psi}{\partial t} = D\left(\frac{\partial^2}{\partial\epsilon^2} + \frac{\partial^2}{\partial y^2}\right)\psi + \psi + \psi\eta = D\nabla^2\psi + \psi + \psi\eta. \tag{2.53}$$

Now, implementing the Cole-Hopf transformation $\psi = e^h$ into the equation, one finally gets directly the KPZ equation for two independent space variables ($2+1$ dimensions),

$$\frac{\partial h}{\partial t} = D\nabla^2 h + D(\nabla h)^2 + \eta. \tag{2.54}$$

Therefore, the statistics of the interface of a $(2+1)$-dimensional *pulled front* with multiplicative noise belong to the KPZ universality class in $2+1$ dimension. While the same approach would not transform the sFKPP equation into the KPZ equation, the result was nevertheless generalized for the sFKPP system as well.

The conjecture was supported in [93] by numerical simulations of the $A \to 2A$, $2A \to A$ particle model. However, the simulations were performed under conditions in which the average density per correlated volume was very small, i.e. the intrinsic fluctuations were very large (strong noise). Thus the front was far from being described by the Fisher fronts. Actually, strong-noise systems have different dynamics, and even the velocity scales differently [94]. It was shown in [95] that actually the interface fluctuations of the particle model in $d+1$ where described by the d-dimensional KPZ universality class. To check the validity of the conjecture and have a better understanding of the role that thermal fluctuations play, we next undertake simulations of the sFKPP equation in $2+1$ dimensions, using a special numerical algorithm to simulate stochastic PDEs which has been adapted to the sFKPP equation. This allows us to perform simulations in the limit of weak intrinsic noise, which was unavailable to computationally expensive particle models.

3

Numerical method for the sFKPP equation

In this Chapter we present the algorithm that we have employed in order to simulate the sFKPP equation numerically. This algorithm was proposed in [84, 85]. It integrates numerically the sFKKP equation using a splitting-step method. The necessity for this kind of algorithm comes from the fact that a naive discretization of the equation using e.g. standard Cauchy-Euler scheme can not ensure positivity of the solution for all times steps. Namely, we recall the stochastic sFKPP equation

$$\frac{\partial \rho}{\partial t} = D\frac{\partial^2 \rho}{\partial x^2} + \rho - \rho^2 + \sqrt{\sigma\rho}\eta(t), \tag{3.1}$$

so that the centered finite difference approximation of the space derivative gives a discrete equation of the form

$$\rho_i(t+\Delta t) = \rho_i(t) + D\frac{\Delta t}{\Delta x^2}\left[\rho_{i+1}(t) + \rho_{i-1}(t) - 2\rho_i(t)\right] + \\ + \Delta t(\rho_i(t) - \rho_i^2(t)) + \sigma\sqrt{\rho_i}\,\Delta W_i, \tag{3.2}$$

where $\Delta x = x_{i+1} - x_i$, $\Delta t_i = t_{i+1} - t_i$, and $\Delta W_i = W(t_{i+1}) - W(t_i)$, where $W(t_i)$ is a Wiener process (more details in [79, 96, 97]). The deterministic part of the equation will have a non-negative solution for a non-negative initial condition if the following stability condition is fulfilled, i.e. the sum of RHS terms that contain $\rho_i(t)$ has to be greater than zero:

$$\Delta x > \sqrt{2D\Delta t}. \tag{3.3}$$

Unfortunately, this may not be sufficient to provide non-negativity of the full solution, as the noise term could lead to negative. In order to overcome this problem, first we will explain the splitting step method for stochastic differential equations [95] and then the "splitted" equations will be solved separately.

3.1 Splitting-step method

After we have derived the equation to model the reaction diffusion process $A \to 2A$, $2A \to A$ we have to discretize it in order to implement a simulation algorithm. The problem is as discussed before that just sampling white noise random numbers could lead to a negative solution that makes no sense mathematically and physically. Therefore, we need to take a different approach. Instead of integrating the Langevin equation directly we could in principle, find the evolution of the probability distribution function which satisfies its associated Fokker-Planck equation [98] (for the relation between the Langevin and its associated Fokker-Planck equation, see [79]). The idea of this approach it to see whether the distribution function, as a solution to the Fokker-Planck equation, includes negative solutions or not. Unfortunately, this is not as easy as it seems due to the difficulty to solve the Fokker-Planck equation associated with the full sFKPP equation. The technique we have used to solve the full sFKPP equation numerically is the splitting step method [95] and here we present it for Langevin equations. In general if we have a stochastic differential equation of the form

$$dX(t) = [\alpha(X(t), t) + \beta(X(t), t)]dt + \sigma(X(t), t)dW(t), \tag{3.4}$$

where α and β are functions, we split it into two equations. The first one is usually selected in order to be solved exactly (analytically) and the second one numerically. Therefore, this method is also known as a semi-analytical method. Assuming that there is a solution to the equation

$$dX_1(t) = \beta(X_1(t), t)dt + \sigma(X_1(t), t)dW(t), \tag{3.5}$$

we obtain the probability distribution of the function X_1. We use it to solve the remaining part of the equation:

$$dX_2(t) = \alpha(X_2(t), t)dt. \tag{3.6}$$

Hence, the solution of the first equation (3.5) is a stochastic process Y_t which has the initial condition $Y_t = X(t)$ and after the time lapse Δt has the value $Y_t = X_1(t + \Delta t)$. Now, the value Y_t is used as an initial condition for the second process $\widetilde{Y}_t$ described by Eq. (3.6), which is then solved analytically or using any appropriate numerical algorithm. The solution $Y_{t+\Delta t} = \widetilde{X}_2(t+\Delta t)$ represents the numerical solution of Eq. (3.4) after time step Δt, which is then used as an initial condition $X_1(t + \Delta t) = Y_{t+\Delta t}$ for the next time step evolution. In [95] there is a detailed proof that the algorithm converges.

3.2 Algorithm for the sFKPP

The splitting step method discussed in the previous section allows us to divide the sFKPP equation (3.1) on two parts that could be solved by either analytical or numerical techniques [84]. Our choice was to completely separate the stochastic term from the deterministic ones as the equation for only stochastic term can be solved analytically [80]. Hence, the first equation becomes

$$\frac{\partial \rho}{\partial t} = \sqrt{\sigma \rho}\, \eta(t). \tag{3.7}$$

The inclusion of the linear term ρ into this equation would also lead to an analytical solution [80]. The solution of Eq. (3.7) provides a prediction which has to be corrected by solving the reminder of the equation, which in our case is the deterministic part,

$$\frac{\partial \rho^*}{\partial t} = D\frac{\partial^2 \rho^*}{\partial x^2} + \rho^* - \rho^{*2}. \tag{3.8}$$

Therefore this algorithm is also called a predictor-corrector algorithm. A numerical approximation of Eq. (3.8) can be easily solved and the new solution ρ^*, for any (non-negative) value of ρ, will remain non-negative, again if Condition (3.3) is fulfilled.

First we solve the stochastic equation (3.7) by employing the associated Fokker-Planck equation [80], which will provide the distribution function for the solution ρ. In this case $a = 0$ and $b = \sqrt{\sigma\rho}$, hence the associated Fokker-Planck equation is

$$\partial_t p(\rho, t|\rho_0, t_0) = \frac{\sigma}{2}\partial_\rho^2\, \rho\, p(\rho, t|\rho_0, t_0). \tag{3.9}$$

The initial condition for the Fokker-Planck equation is the initial function ρ_0, which can be written as $p(\rho, t_0|\rho_0, t_0) = \delta(\rho - \rho_0)$. In order to eliminate the dependence on σ we rescale Eq. (3.9) through the change of variable $\rho \to \rho/\sigma$. As ρ has to be a non-negative function, the probability distribution has to be zero for negative values of ρ. We transform Eq. (3.9) using the Laplace transform. For easier notation and manipulation we introduce the change of variables

$$\psi(\rho, t) = \rho\, p(\rho, t|\rho_0, t_0). \tag{3.10}$$

Bearing in mind the non-negativity of ρ, the Laplace transform of the time derivative of a function is

$$\partial_t \psi(s) = s\psi(s) - \psi(t = 0) = s\psi(s) - \rho_0\delta(\rho - \rho_0); \tag{3.11}$$

Then, the transformed equation (3.9) is

$$\sigma\rho\frac{\partial^2 \psi(s)}{\partial \rho^2} - s\psi(s) = \rho_0\delta(\rho - \rho_0). \tag{3.12}$$

This differential equation is of the Bessel type. Introducing the change of variable $u = 2\sqrt{\rho}$ it becomes the proper Bessel equation

$$\left(\frac{\partial^2}{\partial u^2} - \frac{1}{u}\frac{\partial^2}{\partial u^2} - s\right)\hat{\psi}(s) = \frac{u_0}{2}\delta(u - u_0), \tag{3.13}$$

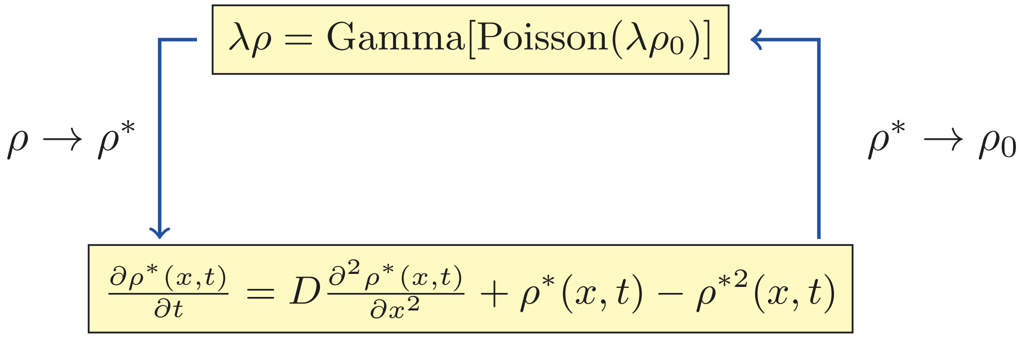

Figure 3.1: Scheme of the splitting-step sFKPP algorithm; the upper quadrant predicts the solution and the lower quadrant corrects it.

for which the solution reads

$$\psi(s) = 2\sqrt{\rho\rho_0}\, K_1(2\sqrt{s\rho_>})\, I_1(2\sqrt{s\rho_<}) + 2\sqrt{\frac{\rho_0}{\rho s}}\, K_1(2\sqrt{s\rho_0})\, \delta(\rho). \tag{3.14}$$

Here, $\rho_>$ and $\rho_<$ represent, respectively, a value of ρ that is larger or smaller than ρ_0, while K_1 and I_1 are modified Bessel functions. Performing the inverse Laplace transform, we obtain the solution for the probability density,

$$P(\rho, t) = \lambda e^{-\lambda(\rho_0+\rho)}\sqrt{\frac{\rho}{\rho_0}} I_1(2\lambda\sqrt{\rho_0\rho}) \tag{3.15}$$

where we have defined

$$\lambda = \frac{2}{\sigma^2(t-t')} = \frac{2}{\sigma^2\Delta t}.$$

In order to simplify Eq. (3.15), we use the Taylor expansion of the Bessel functions. The equation then reads

$$P(\rho, t) = \sum_{n=0}^{\infty} \frac{(\lambda\rho_0)^n e^{-\lambda\rho_0}}{n!} \frac{\lambda e^{-\lambda\rho}(\lambda\rho)^{n-1}}{\Gamma(n)}. \tag{3.16}$$

Recalling the Poisson distribution [79]

$$P(x = n; \lambda) = \frac{\lambda^n e^{-\lambda t}}{n!}, \tag{3.17}$$

and the Gamma distribution

$$P(x, k, \theta) = \frac{x^{k-1} e^{\frac{x}{\theta}}}{\theta^k \Gamma(k)}, \tag{3.18}$$

we see that Eq. (3.16) can be interpreted in such a way that the first ratio inside the sum represents the Poisson distribution that $\lambda\rho_0$ has a value n, while the second one represents the Gamma distribution with parameters $\theta = 1$ and $k = n$. Therefore we could numerically determine the next value of ρ after a time step Δt by sampling random numbers from both the Poisson and the Gamma distribution functions,

$$P(\rho, t|\rho_0, t_0) = \text{Gamma}[\rho, \text{Poisson}(\lambda\rho_0), 1], \tag{3.19}$$

in order to get the predicted value of $\lambda\rho$. In this way we are sure that the distribution function will yield non-negative values of ρ only.

Now we have found the probability distribution function for Eq. (3.7) and, by sampling random numbers, we are able to predict the next state. Then by putting it simply into the deterministic part of the sFKPP equation, (3.8), we can correct our solution and obtain the value of ρ after time step $2\Delta t$. Setting up an iterative procedure as sketched in Fig. 3.1, we can model how the system changes from one state to the other one in specified period of time.

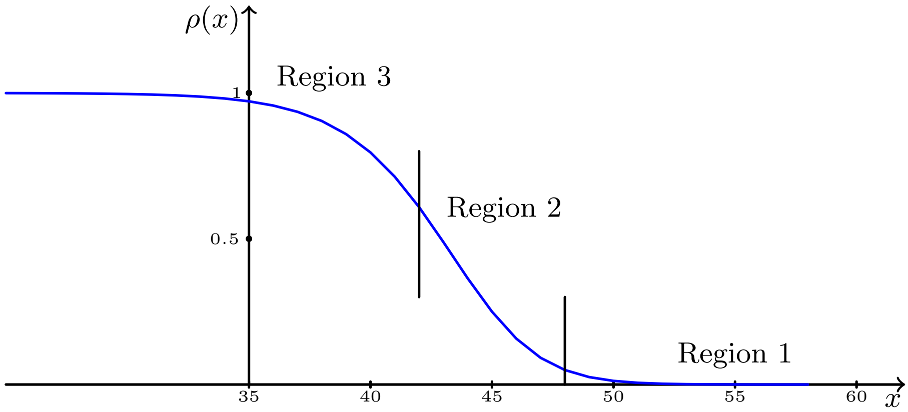

Figure 3.2: Shape of the traveling waves due to internal fluctuations divided onto a three regions.

As defined in Sec. 2.2.2, σ represents the number of particles, $\sigma = N^{-1/2}$. Thus, in the systems we want to study the parameter λ is typically very large and Gamma of a Poisson distribution can be approximated by a Gaussian distribution, which takes us back to the Langevin equation (3.1). In this way we save a large amount of cpu time, as sampling Gaussian random numbers is much faster than sampling Gamma or Poisson distributions. For the random number generator we employ, which is defined in [99], we obtain that sampling Gaussian random numbers is at least 5 times faster. In order to further speed up simulations we split our traveling wave into three regions, as graphically presented in Fig. 3.2:

- Region 1: For every point on the left side of the front where $\rho > 1/2$ internal fluctuations are too small to cause any change in the shape of the solution, hence in this region we will only integrate the deterministic part of the sFKPP equation.

- Region 2: From the middle point of the front, $\rho = 1/2$, up to the point where $\lambda\rho$ is of order 10^3, instead of sampling the Gamma or Poisson distributions we integrate the Langevin equation
$$\rho^* = \rho_0 + \sigma\sqrt{\rho}\,\Delta t \mathcal{N}(0,1), \tag{3.20}$$
where $\mathcal{N}(0,1)$ is a normal distribution with zero mean and unit variance.

- Region 3: For every $\lambda\rho < 10^3$, we sample the Gamma-of-Poisson distribution as defined in (3.19).

We have tested the algorithm for one dimensional system by integrating the full front using Eq. (3.19) as a predictor step. Comparing to the cpu time needed to integrate just the deterministic FKPP equation, the algorithm is more than 100 times slower. However, splitting the wave into the three regions works just two times slower than integrating the deterministic equation. This is a significant improvement, bearing in mind that the two-dimensional stochastic equation will require an integration time that is further multiplied by the lateral size.

4

Universality Class of sFKPP fronts

Due to many interesting results (some of them described in Chap. 2) that show how even really weak fluctuations affect the dynamics of Fisher fronts our aim is to study the latter of $2d$ sFKPP fronts, in order to check validity of the conjecture stated in Sec. 2.3.2 (Ref. [92]) in the case of weak noise. Through the conjecture a universality class is assigned to the stochastic Fisher fronts. Moreover, we go one step further in order to improve our understanding as to why the universality class of the fronts is the one we obtain. Here, results are obtained by simulating the sFKPP equation

$$\frac{\partial \rho}{\partial t} = D\triangle\rho + \rho(1-\rho) + \sigma\sqrt{\rho}\,\eta(x,t), \tag{4.1}$$

in the case of various weak noise strengths using the algorithm described in Chap. 3. The domain is a grid of size $L_\perp \times L_\parallel$. All the simulations are done using the same initial condition, a step function, so that the wave is meant to travel along the $x_\perp$ direction,

$$\rho_0(x,y,t_0) = \begin{cases} 1 & \text{if } x_\perp \leq 0 \\ 0 & \text{if } x_\perp \geq 0. \end{cases} \tag{4.2}$$

Boundary conditions along the $x_\parallel$ direction are periodic and no-flux (zero derivative) in the $x_\perp$ direction. If not stated otherwise the diffusion constant is always one. We follow the *front* interface defined by the equipotential line $x_\perp = h_\mathrm{f}(x_\parallel, t)$ where $\rho(h_\mathrm{f}(x_\parallel,t), x_\parallel, t) = 1/2$. As fluctuations become dominant at values $\rho \sim 1/N$, we also define the *edge* interface $h_\mathrm{e}(x_\parallel, t)$ by the equipotential line where $\rho(h_\mathrm{e}(x_\parallel,t), x_\parallel, t) = 1/N$, see Fig. 4.1.

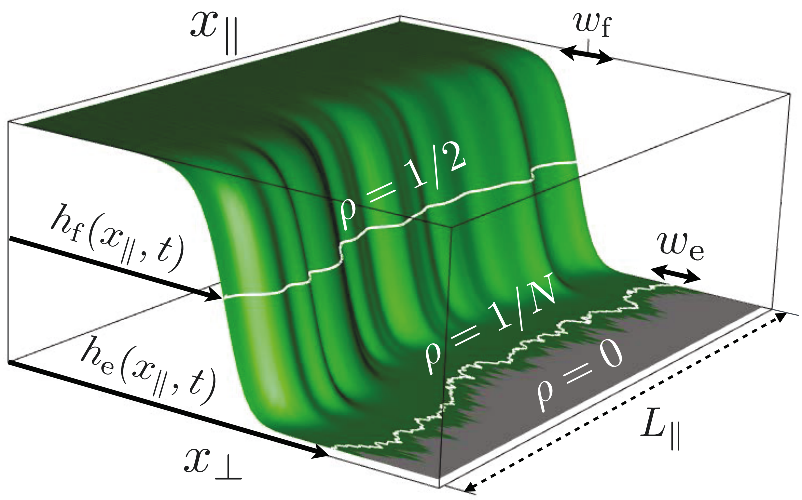

Figure 4.1: Stochastic Fisher front in $d_E = 3$ $(2 + 1)$, as obtained by numerical simulations of the sFKPP equation, with indication of notation and quantities introduced in the text. White lines correspond to equipotential lines at $\rho = 1/2$ (front interface) and $\rho = 1/N$ (edge interface).

The simulations of the sFKPP equation, we performed using the algorithm described in Chapter 3. The simulation code is written in the programming language C++; random number generators have been taken from [99]. Graphs were partly done in X-Grace and partly in R-project. Power spectrum analysis requires Fourier transform, which, due to numerical results from simulations, has to be discrete Fourier transform, so we have employed the Fast Fourier algorithm [99] given by a set of the functions in C as can be found in *www.fftw.org*. We performed the cross-correlation analysis in order to study the relation between the equipotential curves, which will be discussed in Sec. 4.3. The calculations were done in R-project.

4.1 KPZ universality class

As discussed in Chap. 2 weak noise (systems with large number of particles per unit volume) do not affect the macroscopic region of a front explicitly. The surface in that region is macroscopically smooth and well described by the noiseless equation along the $x_\parallel$ direction. This suggests that even if the sFKPP equation could be correctly Cole-Hopf transformed to the KPZ equation (see Sec. 2.3.2) of the same dimensionality, the noise in the KPZ should only depend on the $x_\parallel$ direction. Naively, it implies that the universality class should have one dimension less than the sFKPP equation itself. To confirm this numerically we follow both macroscopic front $h_f(x_\parallel, t)$ and microscopic edge $h_e(x_\parallel, t)$, see Fig. 4.1, one-dimensional equipotential interfaces that travel in time with a roughly constant velocity (which is given by the Brunet-Derrida formula, Sec. 2.3.1, although we have seen a slight change we left the validity of this formula in $2d$ an open question), but which also roughen as a result of noise fluctuations. To assess these dynamics [1], we study the roughness of the interface,

$$w^2(t) = \langle [h(x_\parallel, t) - \overline{h}(t)]^2 \rangle, \tag{4.3}$$

and the structure factor,

$$S(q) = \langle \hat{h}_q(t) \hat{h}_{-q}(t) \rangle, \tag{4.4}$$

where $\hat{h}_q(t)$ is the Fourier transform of $h(x_\parallel, t) - \overline{h}(t)$, the bar denotes space average over $x_\parallel$, and $h = h_{\mathrm{f,e}}$. Our simulations show (see Fig. 4.4) that interface fluctuations are very large, even for small noise. In fact, $S(q, t)$ coincides for both interfaces at small $q < q_\times$, which means that, although $h_{\mathrm{f}}(x_\parallel, t)$ is much smoother than $h_{\mathrm{e}}(x_\parallel, t)$ at small spatial scales $q > q_\times$ (see Fig. 4.1), both interfaces display the same large-scale fluctuations. We find that the characteristic distance above which both interfaces display the same fluctuations scales as

$$1/q_\times \sim \log N \qquad \text{(see Fig. 4.2(a))}.$$

This can be intuitively expected, as it coincides with the actual distance separating the two interfaces. Much beyond that characteristic length, the *internal* 2D structure of the front becomes irrelevant, as it is perceived as a one-dimensional object.

Furthermore, these large-scale fluctuations are well described by the KPZ universality class for one-dimensional rough interfaces. In particular, we find that [1]

$$S(q) \sim 1/q^{2\alpha+1} \quad \text{with} \quad \alpha \simeq 1/2, \tag{4.5}$$

$$w^2(t) \sim t^{2\beta} \quad \text{with} \quad \beta \simeq 1/3 \tag{4.6}$$

see dashed lines in Fig. 4.2. Indeed, 2D KPZ behavior characterized by $\alpha \simeq 0.39$ and $\beta \simeq 0.24$ [100] provides a much poorer description of the numerical data, see the respective dot-dashed lines in Figs. 4.2(a) and 4.2(b). This result corroborates the finding in [88]: fluctuations of $d_\parallel$-dimensional FKPP fronts indeed belong to the KPZ universality class for $d_\parallel$-dimensional interfaces. But it also highlights a potential problem with system size: for large q, fluctuations of $h_{\mathrm{f}}(x_\parallel, t)$ are very small and the asymptotic KPZ regime is only achieved for very large systems sizes.

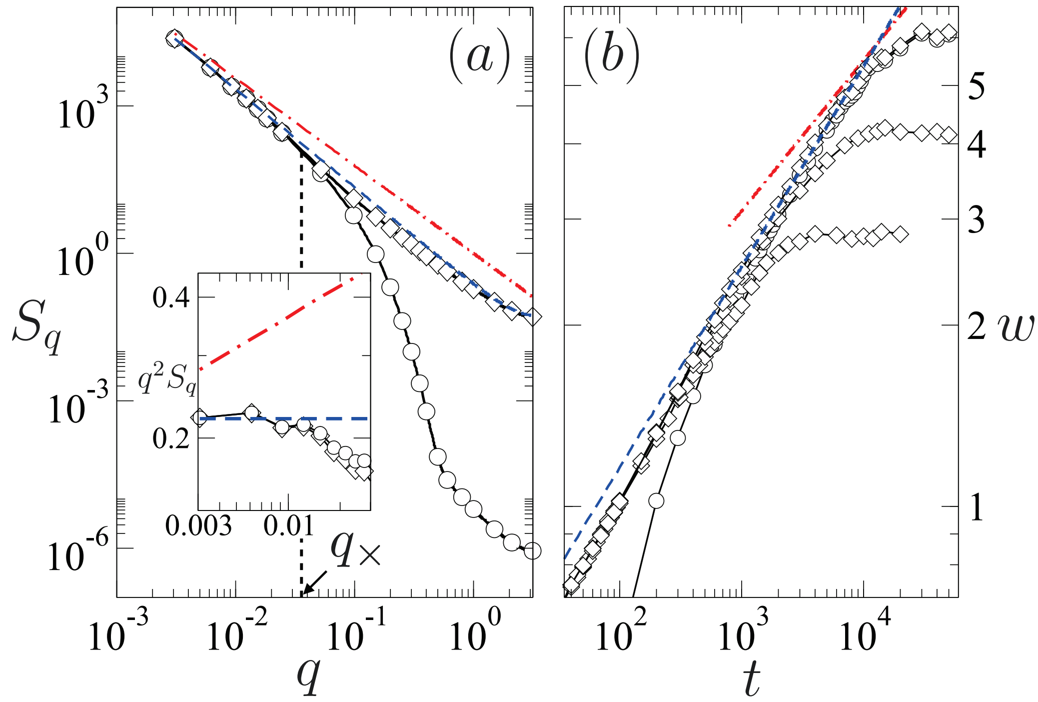

Figure 4.2: (a) Structure factor of the front (circles) and edge (diamonds) interfaces, together with the behavior of the 1D (blue dashed) and (red dot-dashed, asymptotic) KPZ behaviors. System size is $L_\parallel = 1024$. Inset: rescaled structure factor $q^2 S_q$ as a function of q. For small q, the front and edge interfaces both show 1d KPZ behavior $S_q \sim q^{-2}$. Lines correspond to those in the main panel. (b) Time evolution of the roughness of the edge interface for $L_\parallel = 2048, 1024$, and 512 (diamonds, top to bottom) and roughness of the front interface for $L_\parallel = 2048$ (circles) compared to the 1D (blue dashed) and 2D (red dot-dashed) KPZ scaling behavior. In all cases $N = 10^6$. Solid lines are guides to the eye. All units are arbitrary.

4.2 Tracy-Widom distribution in sFKPP fronts

In the previous section we argued that the growth exponents of an equipotential interface, as a result of the evolution of traveling waves given by the sFKPP equation in two space dimensions, belongs to the one-dimensional KPZ universality class. We showed good agreement only for very large system sizes, see Fig. 4.2(b). In order to provide a more complete characterization, recall from Sec. 1.4 that the full probability distribution of surface height fluctuations is currently known for the KPZ universality class in one dimension. Specifically, we recall that the analytical solution for the height field reads

$$h(x,t) = vt + ct^{\beta}\chi, \tag{4.7}$$

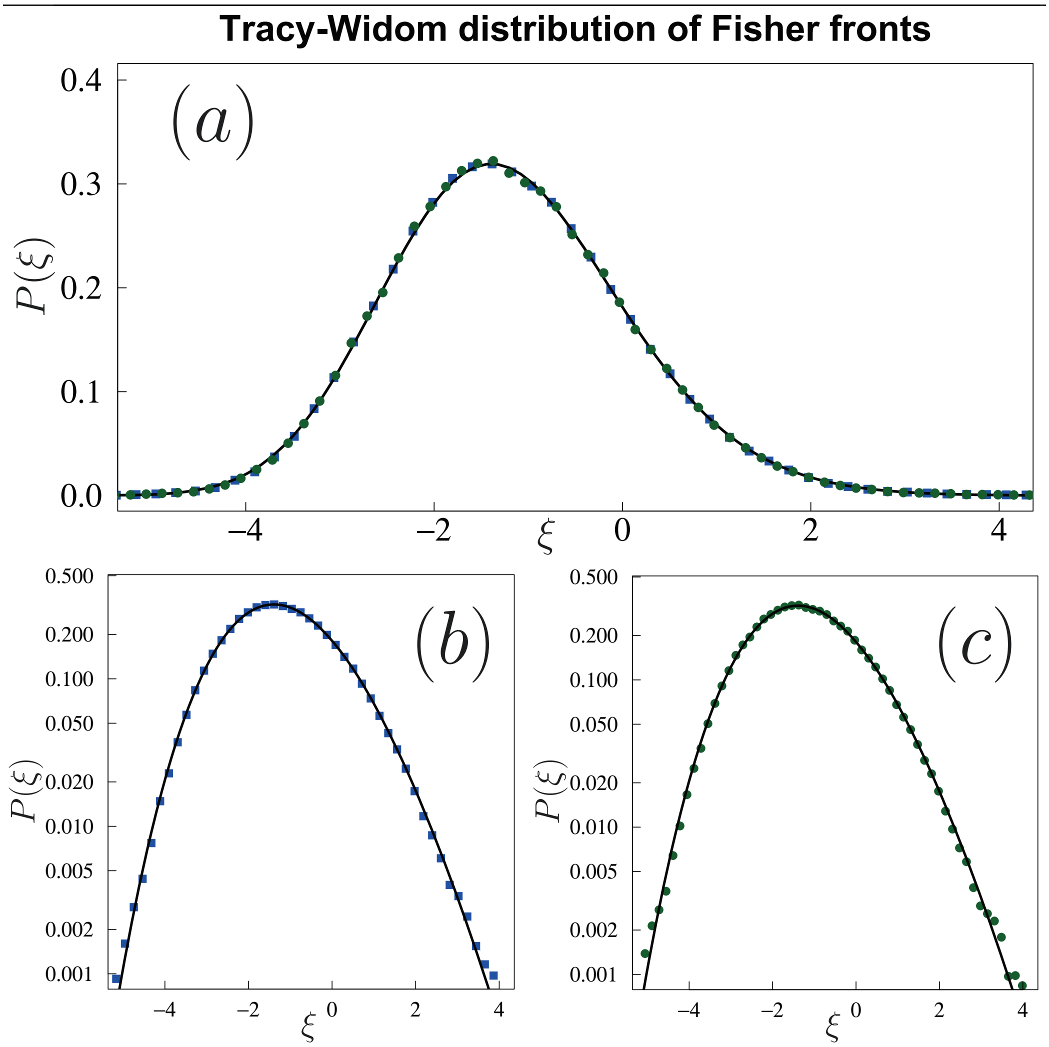

Figure 4.3: (a) Tracy-Widom distribution: Comparison between analytical solution (black line) for the TW-GOE distribution and the numerical solution of the *front* (blue squares) and the *edge* (dark green circles) distribution during the KPZ-like growth. (b) and (c): log $P(\xi)$ representation of the graph (a) for *front* and *edge* respectively

where $\beta = \frac{1}{3}$ for the KPZ equation in the growth regime and χ is a random variable which follows the Tracy-Widom distribution in the Gaussian Orthogonal Ensemble (TW-GOE) [47]. Therefore, in our case, we have calculated the distribution function of the relative *front* and *edge* positions at times where the system roughness on average grows as a power-law $w(t) \sim t^{1/3}$. In order to have the best possible comparison the largest system size is taken ($l_y = 2048$). The interval is $t \in [2000, 7000]$. We obtain a satisfactory comparison with the analytical form of the TW-GOE distribution function (see Fig. 4.3), in view of our current limitations in terms of statistics and computing time.

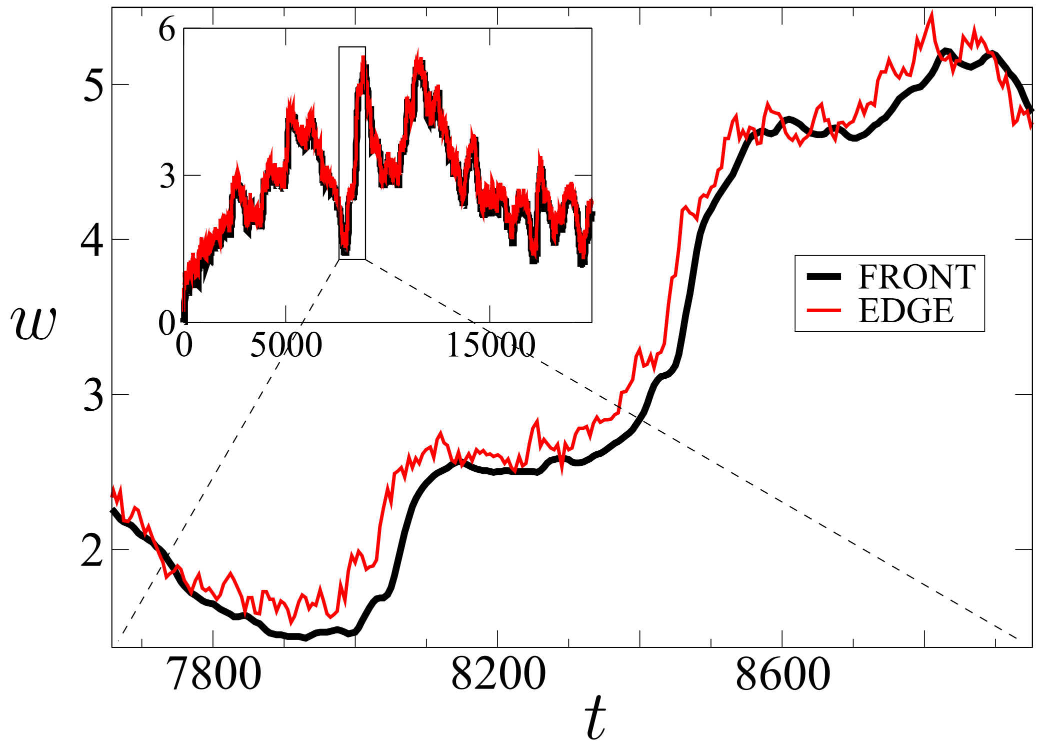

Figure 4.4: (a) Roughness time series for the edge (thin red solid line) and front (thick black solid line) interfaces, for a single noise realization of the sFKPP equation. Inset: Full dynamics. For the full evolution see video in [160].

4.3 Propagation

We have calculated growth exponents of the one-dimensional microscopic and macroscopic equipotential interface (Fig. 4.1) of the sFKPP in order to assign it to a universality class in the case of weak noise. Due to the exponential form of the solution the latter plays important role only in microscopic region of the wave (see Sec. 2.3). We saw in Fig. 4.2 that the structure factors of the both interfaces match perfectly in the large-scale correlation region (small q). Hence, one could conclude that the relationship between $h_{\mathrm{f}}(x_{\parallel}, t)$ and $h_{\mathrm{e}}(x_{\parallel}, t)$ does not only happen at large scales for aggregated variables like $w^2(t)$ and $S(q, t)$. Motivated by the phenomenological theory [86] described in Sec. 2.3.1, in which the fluctuations of the $d = 1$ front position in the sFKPP equation were explained by large and rare fluctuations at the front edge, we study how the fluctuations of the front and edge interfaces are related. Fig. 4.4 shows the dynamics of the roughness $w(t)$ of both interfaces, for a single noise realization. As we can see, the large-scale fluctuations of $h_{\mathrm{f}}(x_{\parallel}, t)$ come closely behind those at the edge, which suggests that any disorder that microscopically happens at the edge propagates back and eventually occurs at the front interface. Here, microscopical disorder means that a strong enough fluctuation creates particles at a

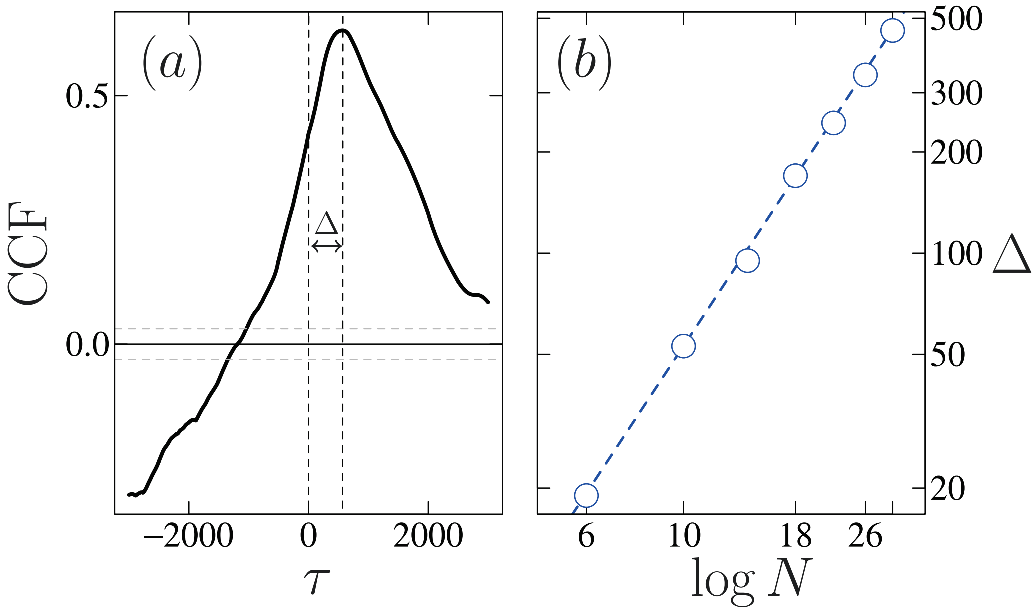

Figure 4.5: (a) Cross-correlation function between front and edge roughness time-series, for a single noise realization and $N = 10^{30}$. The time to the first maximum defines the lag Δ, see main text. (b) Values of Δ (circles) for different values of N, and $L_y = 512$. The line is a fit to $\Delta \sim \log^{\gamma} N$, where $\gamma = 1.97$. Statistical errors are smaller than the symbol size. All units are arbitrary.

distance macroscopically seen ahead of the edge position. There are two ways that one could describe how similar these curves are. Collapsing the front roughness function to the edge gives the time shift between them. Here, in order to estimate how significant the result is we have computed the cross-correlation between the $w(t)$ time series at both interfaces

$$\mathrm{CCF}(\tau) = \tilde{w}_{\mathrm{f}} * \tilde{w}_{\mathrm{e}}[\tau] = \sum_t \tilde{w}_{\mathrm{f}}(t)\tilde{w}_{\mathrm{e}}(t+\tau),$$

where $\tilde{w}_i(t)$ is the normalized unit variance and zero mean time series constructed from $w_i(t)$. The CCF has a peak at a time lag $\tau = \Delta$, which depends on N. An accurate regression yields

$$\Delta \sim \log^{\gamma} N, \quad \text{where} \quad \gamma = 1.97 \pm 0.03,$$

see Figs. 4.5(a,b). Interestingly, this time scale has the same scaling as the relaxation time of perturbations in $d = 1$ FKPP fronts found in [101], which could explain the origin of the former: fluctuations produced at the edge of the front propagate into the macroscopic front $h_{\mathrm{f}}(x_{\parallel}, t)$ within a time which is set by the relaxation rate of fluctuations in the system. These findings suggest a similar picture to the one found in [86] for one less dimension: the fluctuations of $h_{\mathrm{f}}(x_{\parallel}, t)$ are dominated by those at $h_{\mathrm{e}}(x_{\parallel}, t)$, which in our case turn out to be described by the 1D KPZ universality class.

4.4 Scaling rule

We simulate the sFKPP equation for different number of particles N which implies different amplitude of fluctuations, hence in a log-log scale we obtain structure factors which are shifted with respect to one another, as shown in Fig. 4.6. We found the coefficients so that when collapsing curves the distance between this curve and other curves for different σ is minimum. We are interested in how macroscopic behavior scales, which means long distance correlations (small values of q) so we compare the curve until the point $q_\times$ that separates the macroscopic from the microscopic behavior. Due to universality class of Fisher fronts as just determined, the front and edge scaling properties can be calculated using the analytical formula for structure factor of the KPZ universality class in one dimension,

$$S(q) \sim \frac{T_{\text{eff}}}{q^2} \tag{4.8}$$

where, T_{eff} represents the strength of fluctuations, also called an *effective "temperature"* due to analogy with KPZ-like models where fluctuations are mostly thermal.

Finally, we study how front fluctuations depend on the strength of the noise $1/N$. To this end we compare the $S(q)$ curves obtained for different values of N. We find (see Fig. 4.6) that data can be collapsed in the small-q region using N-dependent factors, A_N, and B_N, such that

$$S(q)/A_N \;=\; f(qB_N), \tag{4.9}$$

where $f(x)$ is an N-independent function that behaves as $f(x) \simeq C/x^2$ for small arguments. Moreover, from Fig. 4.6(b) we find

$$A_N, B_N \sim \log N, \tag{4.10}$$

which justifies in particular that $q_\times$ as defined in Fig. 4.4 scales as

$$q_\times \sim 1/\log N.$$

Furthermore,

$$S(q) \sim CA_N/(B_N^2 q^2),$$

suggesting that the interface feels an *effective "temperature"*

$$T_{\text{eff}} = CA_N/B_N^2,$$

and hence

$$T_{\text{eff}} \sim \frac{1}{\log N}. \tag{4.11}$$

The effective "temperature" of FKPP fronts thus decays very slowly as $N \to \infty$. Note that, even at Avogadro numbers of particles $N \simeq 10^{23}$ for which microscopic noise might be expected to be negligible, we get a value for T_{eff} that is still moderate and implies observable macroscopic fluctuations. Once again, fluctuations in FKPP equations produce strong corrections to the expected deterministic behavior.

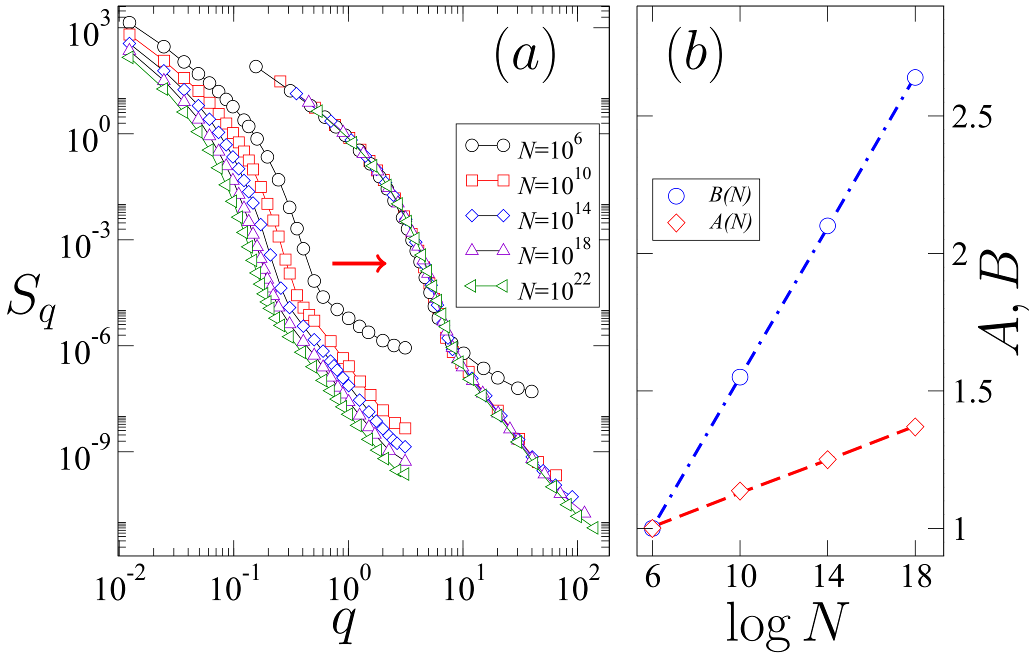

Figure 4.6: (a) Structure factor of the front interface for different values of N, together with rescaled curves obtained by collapsing all curves to the $N = 10^6$ data in the macroscopic region $q \ll 1$; see main text for details. (b) Rescaling factors of S_q and q as functions of N (symbols) together with linear fits (lines). Statistical errors are smaller than the symbol size. All units are arbitrary.

4.5 Conclusions

In summary, we have studied the macroscopic fluctuations of Fisher fronts in the relevant, real-life context of three Euclidean dimensions. What we have found is that the modification to the front velocity due to microscopic fluctuations, as anticipated by Brunet and Derrida [7], is not the only strong correction to the dynamics. Actually, the width of the front is also substantially affected, featuring fluctuations which again scale as $1/\log N$. Hence, the discrete nature of density fluctuations at a microscopic level induces large, observable randomness at large scales. This implies that there is no weak-noise or deterministic regime in real-life Fisher fronts. Moreover, we have found that the macroscopic front line evolves like a low-pass filter of the edge fluctuations and thus both objects share the same universality class for large spatial and temporal scales. In particular, since the edge is a one-dimensional entity undergoing dynamics which is not constrained by conservations laws [1], we find that front and edge's fluctuations both feature 1D KPZ scaling. Incidentally, kinetic roughening in the KPZ universality class has been recently found in systems for which (stochastic one-dimensional) FKPP-like waves are advocated, such as range expansion of genetically diverse bacterial populations [102, 103]. Note that the KPZ behavior that we obtain corresponds to $h_{\mathrm{f,e}}$, and not to the variable ρ that satisfies the sFKPP equation (4.1). It is to be expected that, if one were able to write down the dynamical equation for the effective variables $h_{f,e}$ (which in principle seems a non-straightforward result for pulled fronts of the sFKPP equation) then the information about the steady-state properties of the KPZ equation could be relevant to their long time behavior. This includes the non-equilibrium potential [39] ensuing in its variational formulation and exact results on KPZ universality [50]. Note that such type of effective equation was actually derived in [92] for other type of noise in the FKPP equation as show in detail in Sec. 2.3.2, but our results show that the generalization of this result does not hold in the sFKPP equation (4.1) were intrinsic fluctuations dominate.

Since stochasticity is inevitable at the edge of $3d$ traveling waves, our results show that there is no weak-noise or deterministic regime in real-life Fisher fronts. Note that, due to the universality properties that ensue in reaction-diffusion front propagation, one expects Eq. (4.1) to describe the evolution of a large class of systems, including e.g. those in the celebrated directed percolation universality class [104], or even to arise in the process of obtaining the normal form for suitable stochastic multi-scale systems. This is in principle a delicate process in which full separation between fast and slow dynamics can nonetheless be achieved under appropriate conditions [105, 106, 157]. Overall, our conclusion on the lack of weak-noise regime in Fisher fronts has an important consequence about the relevance of the deterministic FKPP equation as a model to explain the observations in experimental setups: since FKPP waves are always stochastic, are the observed results affected by a macroscopic noise?

5

Stochastic Lubrication equation

This chapter as well as the following ones are dedicated to wetting and dewetting processes. Thin fluid films are usually metastable and due to small perturbation, they dewet and break into drops [19, 107, 108]. The dynamics of such processes are still far from being understood and the need for an accurate description is essential in industry and several branches of science [109–111]. Description of the microfluidic flow leads to better understanding and analytical predictions in biological systems. Industrial interests are to make thin metal and polymer films in which somehow the converse processes take place, where a droplet placed on a surface starts to spread out to fill the substrate.

These kinds of problems are usually treated thermodynamically, in order to find more favorable state of a fluid, or by the Navier-Stokes equations to describe the full fluid dynamics. In general, they are far too complicated to be solved exactly. Nevertheless, in many special cases they are an amenable to analytical approaches, while still describing well certain natural and experimental environments.

We are specially interested in the lubrication equation [112], a special case of the Navier-Stokes equations when the liquid film is thin. Numerical solutions of the lubrication equation reproduce wetting and dewetting properties, as seen in experiments with liquid metals and polymers, Fig. 5.1. However, in certain setups the lubrication equation fails to reproduce time and length scales or pattern formation as observed in experiments.

The lubrication approximation assumes continuum density function which leads to smooth fluid surface. On microscopic scales this assumption is too strong as fluid particles due to finite number and size move and collide with each other randomly. These kind

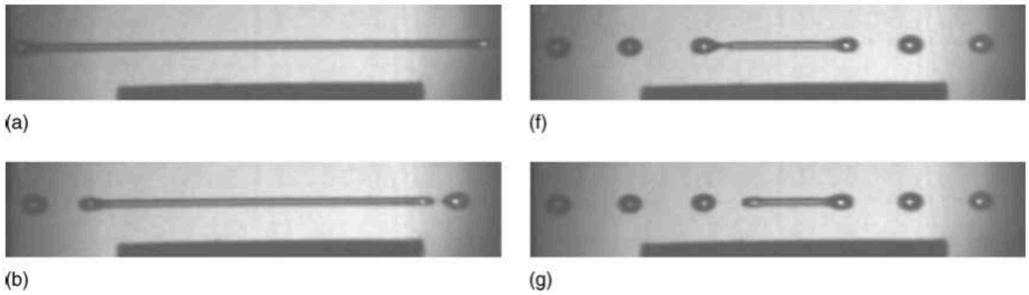

Figure 5.1: Example of time evolution of a thin liquid metal film that breaks into droplets due to the dewetting properties of the fluid. Picture taken from [108] is a result of the experiment performed in [19].

of interactions introduce randomness in the fluid pressure which leads to an additional, stochastic pressure term in the Navier-Stokes equations. In this chapter we show how to include these effects, i.e. derive the stochastic lubrication equation from the stochastic Navier-Stokes equations.

5.1 Stochastic Navier-Stokes equations

Fluids are complex systems that contain many particles whose interactions are too complicated to be modeled even in the simplest form. These particles also interact with the surface that bounds the fluid, which usually is solid substrate under the fluid and a gas state above. These microscopic interactions are such that on scales larger than the typical particle size, they can be approximated by continuous functions, as a fluid displays well defined, smooth macroscopic surface [2, 37]. Therefore, the fluid dynamics can be modeled from the following assumptions: A total fluid volume can be divided into small volume elements, where each element contains a large number of particles which macroscopically have the same velocity. Moreover, the velocity of a fluid at any point is a well defined distribution function. Together with the pressure and fluid density, they determine completely the dynamics of the fluid. With these assumptions one can easily derive the Navier-Stokes equations from Newton's second law. Namely, the fluid elements interact through their enclosing surfaces so that on each element a resulting sum of surface forces is applied. Due to gravity, magnetic and electric field, etc. volume (also called body) forces occur within the volume of a fluid element . Writing the sum of surface and volume forces Newton's second law predicts the following behavior of such element:

$$\Delta m \frac{d\vec{v}}{dt} = \vec{F} = \oint \vec{P}_{\vec{n}}\, d\vec{S} + \vec{F}^{\text{vol}}, \tag{5.1}$$

Here, $\vec{P}_{\vec{n}}$ is the pressure tensor and $\vec{n}$ direction perpendicular to the surface element dS. $\vec{F}^{\text{vol}}$ represents the volume forces, Δm being the mass of element. Usually, only the

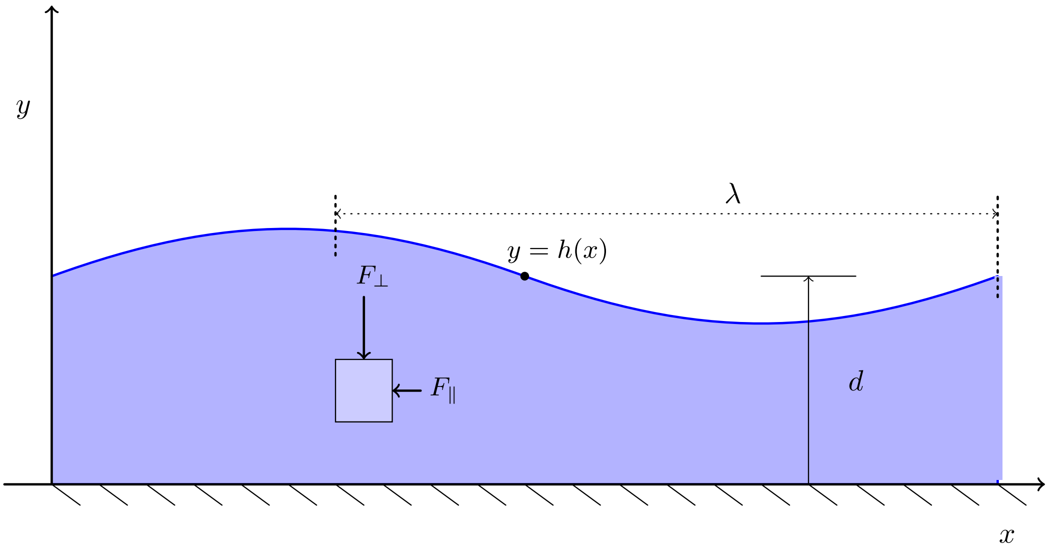

Figure 5.2: A surface of a liquid thin film in $2d$ where the upper boundary is free. There is no slip at the bottom boundary $\vec{v}(y=0) = 0$. Lubrication approximation: Characteristic wavelengths λ in the free surface are orders of magnitude larger than the average film thickness d.

gravity force is considered $\vec{F}^{\text{vol}} = \Delta m \vec{g}$ although there are studies of the influence of i.g. magnetic forces [113, 114]. The mass Δm can be rewritten as a volume integral of the density of the fluid in which. Using the Gauss-Osctrogradsky theorem we convert the surface integral in Eq. (5.1) to volume integral so that Eq. (5.1) becomes

$$\iiint_V \rho \frac{d\vec{v}}{dt} \, dV = \iiint_V \sum_{j=1}^{3} \text{div} \left(\tilde{P}^T \vec{e}_j \right) \, dV + \iiint_V \rho \vec{g} \, dV \tag{5.2}$$

This relation should hold for any choice of the volume shape so that the functions inside the integral satisfy the equality

$$\rho \frac{d\vec{v}}{dt} = \sum_{j=1}^{3} \text{div} \left(\tilde{P}^T \vec{e}_j \right) + \rho \vec{g}. \tag{5.3}$$

The total time derivative on the LHS of Eq. (5.3) could be rewritten using the chain rule, so that the equation becomes

$$\rho \frac{\partial \vec{v}}{\partial t} + \rho \, (\vec{v} \cdot \nabla) \vec{v} = \sum_{j=1}^{3} \text{div} \left(\tilde{P}^T \vec{e}_j \right) + \rho \vec{g}. \tag{5.4}$$

This equation is known as **Euler's**. A real physical problem appears now as we have to model the pressure tensor. Ideal fluids have only non-zero diagonal elements. If the fluid is isotropic these elements are equal. On the other hand real fluids have interactions between particles and also between layers. First, a fluid element moves through the fluid against the neighbour elements causing in general two friction effects. The layers parallel to the moving direction will move due to the friction force. Second, moving against the neighbor elements tend to compress the particles inside and increase the density, which relaxes by pushing neighbouring fluid elements in all directions. These two effects can be accounted for as a sum of friction forces, both in the direction of movement and perpendicular to that direction. When these two effects are significant the fluid is considered **viscous**. If the friction is the same in every direction the force only depends on the change in velocity, so that we write a tensor element in the following form

$$P_{ij} = -p\delta_{ij} + \eta\left(\frac{\partial u_i}{\partial x_j} + \frac{\partial u_j}{\partial x_i}\right) + S \tag{5.5}$$

where η is the shear viscosity of the fluid and p is hydrostatic pressure. This is the basic model of the pressure tensor that leads to the Navier-Stokes equations. To give more realistic description we assume that the pressure is not a smooth function but rather it fluctuates and these effects we include in the term S. The tensor element takes random values such that the mean is given by Eq. (5.5) where $\langle S\rangle = 0$ and the width depends on the temperature of the system. Higher the temperature is, stronger the fluctuations are. The simplest situation corresponds to Gaussian white noise, as originating from thermal fluctuations in the distribution of molecular velocities [37] so that the additional element S_{ij} in the pressure tensor is

$$\begin{aligned}\langle S_{ij}(\vec{r},t)\rangle &= 0,\\ \langle S_{ij}(\vec{r},t)S_{lm}(\vec{r}',t')\rangle &= 2\eta k_B T\delta(\vec{r}-\vec{r}')\delta(t-t')(\delta_{il}\delta_{jm}+\delta_{im}\delta_{jl}).\end{aligned} \tag{5.6}$$

Within the simplest approximation, fluid flow is assumed to be incompressible, i.e. the density remains constant everywhere. Although, every change in pressure or velocity affects the local density, these changes are usually negligible as the system relaxes to maintain the density constant. The equation of continuity (derived in [37])

$$\partial_t\rho + \rho\mathrm{div}\vec{v} + v\mathrm{grad}\rho = 0 \tag{5.7}$$

implies that $\mathrm{div}\vec{v} = 0$. Introducing Eq. (5.5) with the noise tensor $\mathbf{S}$ into Eq. (5.4) and rewriting the derivatives, we obtain the stochastic Navier-Stokes equations [4, 17],

$$\nabla\cdot\vec{v} = 0, \tag{5.8}$$

$$\rho\frac{\partial\vec{v}}{\partial t} + \rho(\vec{v}\cdot\vec{\nabla})\vec{v} = \eta\triangle\vec{v} - \nabla(p-\Pi) + \nabla\cdot\mathbf{S} + \rho\mathbf{g}, \tag{5.9}$$

In Eq. (5.9) we have also introduced the disjointing pressure Π, which accounts for the liquid-solid interaction. Macroscopically, the disjoining pressure corresponds to a change in free energy due to the introduction of a free surface, as compared with that of the fluid bulk [115]. Microscopically, it originates from the interaction between substrate and fluid molecules, e.g. via van der Waals (vdW) forces, and becomes particularly important for thin liquid films. The lubrication approximation of vdW is deferred to Sec. 5.3, after the stochastic thin film equation has been derived.

5.2 Stochastic lubrication approximation

Here we derive the stochastic lubrication equation applying the lubrication approximation to the stochastic Navier-Stokes equations (5.9) in two space dimensions as there is no loss in generality, see Fig. 5.2. The fluid film thickness is denoted by $h = h(x,t)$, where x is the in-plane coordinate, and we assume that the disjoining pressure only depends on the thickness, $\Pi = \Pi(h)$. The film lies on a solid flat substrate while the upper surface remains free. The lubrication approximation assumes that the film thickness is much smaller than the typical wavelengths of the surface $\lambda \gg d$, see Fig. 5.2. As we will see, this implies that all the physics lies at the free surface so that we can re-express the Navier-Stokes equations in terms of the surface height function $h(x)$ only. We do not include the effects of phase changes and we assume no-slip boundary condition at the fluid-solid interface. In $2d$ the velocity field reads $\vec{v} = (u, v)$. Here to simplify the derivation process we will ignore the gravity force. The x and y components of Eq. (5.9) become

$$x: \quad \frac{\partial u}{\partial t} + u\frac{\partial u}{\partial x} + v\frac{\partial u}{\partial y} = -\frac{1}{\rho}\partial_x p + \frac{\eta}{\rho}\nabla^2 u + \partial_x S_{xx} + \partial_y S_{xy}, \tag{5.10}$$

$$y: \quad \frac{\partial v}{\partial t} + u\frac{\partial v}{\partial x} + v\frac{\partial v}{\partial y} = -\frac{1}{\rho}\partial_y p + \frac{\eta}{\rho}\nabla^2 v + \partial_y S_{yy} + \partial_x S_{yx}. \tag{5.11}$$

These equations describe the dynamics of the interior of the fluid film. If the fluid does not evaporate, the boundary condition at the free surface is

$$\frac{d(y - h(x))}{dt} = 0 \qquad \text{which leads to} \qquad \frac{\partial h}{\partial t} = v - u\partial_x h. \tag{5.12}$$

Moreover, the pressure tensor at the free surface is the balance of two contributions. The first one represents the pressure difference between liquid and the vapor states. The pressure difference is related to the curvature of a surface by the Young-Laplace formula [115],

$$\Delta P = \gamma / R_1, \tag{5.13}$$

where the constant γ denotes surface tension which depends on the fluid material, and R_1 is the radius of curvature which can be calculated from the height function as

$$\frac{1}{R_1} = \frac{\partial_x^2 h}{\sqrt{1 + (\partial_x h)^2}^3}. \tag{5.14}$$

The lubrication approximation implies small slopes, so to lowest order we have $R_1^{-1} \simeq \partial_x^2 h$. The second pressure contribution is disjoining which accounts for solid-liquid interactions (long-ranged force) so that at the boundary the total pressure is

$$\mathbf{P}_{\vec{n}} = \left(-p\delta_{ij} + \eta\left(\frac{\partial u_i}{\partial x_j} + \frac{\partial u_i}{\partial x_j}\right) + S_{ij}\right)\vec{n} = (\gamma\partial_x^2 h + \Pi)\,\vec{n}, \tag{5.15}$$

Now we convert Eqs. (5.10) and (5.11) into dimensionless equations rescaling the x and y coordinates (wavelength and film thickness) so that $x = \lambda x'$ and $y = dy'$ and we introduce a small parameter $\epsilon = d/\lambda$. The velocity u can be expressed in dimensionless units by selecting a characteristic value U so that

$$u = \frac{dx}{dt} = \lambda \frac{dx'}{dt} = U\frac{dx'}{dt'}. \tag{5.16}$$

In this way we obtain the scaling relation for the time coordinate $t = \lambda t'/U$ and we calculate the other velocity $v = dUv'/\lambda = \epsilon U v'$. Now a real physical problem arises as we cannot derive mathematically the scaling relation for the pressure p. The similar problem arose when the KPZ equation was rescaled in Sec. 1.4. We needed intuitively to introduce proper scaling relations. Here we apply a similar logic to define a scaling relation for the surface tension γ and the temperature in the noise term defined in Eq. (5.6). Namely, the pressure at the free boundary (surface tension) is the dominant term as it determines the shape of a fluid layer so we set a scaling relation so as to avoid an explicit dependence on ϵ in the surface tension. To do so, we first introduce the rescaled pressure $p = Pp'$ and then we fix the parameter P. The same reasoning applies to the noise, $S_{ij} = \tilde{S}_{ij}S'_{ij}$ and we ignore primes

$$\begin{aligned} x: \qquad \frac{\rho U^2}{\lambda}\frac{\partial u}{\partial t} &= -\frac{P}{\lambda}\partial_x p + \frac{\eta U}{d^2}(\epsilon\partial_x^2 + \partial_y^2)u + \\ &\quad + \frac{\tilde{S}_{xx}}{\lambda}\partial_x S_{xx} + \frac{\tilde{S}_{xy}}{d}\partial_y S_{xy} \end{aligned} \tag{5.17}$$

$$\begin{aligned} y: \qquad \epsilon\frac{\rho U^2}{\lambda}\frac{\partial v}{\partial t} &= -\frac{P}{d}\partial_y p + \frac{\epsilon\eta U}{d^2}(\epsilon\partial_x^2 + \partial_y^2)v + \\ &\quad + \frac{\tilde{S}_{yy}}{d}\partial_y S_{yy} + \frac{\tilde{S}_{yx}}{\lambda}\partial_x S_{yx}. \end{aligned} \tag{5.18}$$

The parameter $\rho U d/\eta$ is called **Reynolds number** [3, 37]. It is a dimensionless number that represents the ratio of inertial to viscous forces. The assumptions used to derive the stochastic thin film equation hold for the liquids that have small Reynolds numbers, where viscosity is not negligible. In Eq. (5.17) the most relevant terms are the viscous force $\eta U/d^2\partial_y^2 u$ and the noise term $\tilde{S}_{yx}/\lambda\partial_x S_{yx}$. Now we introduce scaling for P to match the viscous force $P = \eta U\lambda/d^2$. Physically it means that the viscous forces determine the pressure. To find $\tilde{S}_{ij}$ we use the noise relation (5.6) and we rescale it using $T = \tilde{T}T'$ so that it becomes

$$\langle S_{xx}(x,t)S_{xx}(x',t')\rangle = 4\eta k_B T'\frac{\tilde{T}U}{\lambda^2}\delta(x'-x'')\delta(t'-t''), \tag{5.19}$$

$$\langle S_{yx}(x,t)S_{xx}(x',t')\rangle = 2\eta k_B T'\frac{\tilde{T}U}{\lambda^2}\delta(x'-x'')\delta(t'-t''), \tag{5.20}$$

where $\tilde{S}_{xx} = \tilde{S}_{xy} = \sqrt{\eta k_B \tilde{T}U}/\lambda$. Comparing the two noise terms in Eq. (5.17) we ignore the first one since $\lambda \gg d$. Now we match the remaining noise term with the viscous force and we get the right scaling for the temperature $\tilde{T} = \eta U/k_B\epsilon^2$. The noise terms in Eq. (5.18) (y direction) scale like

$$\langle S_{yy}(y,t)S_{yy}(y',t')\rangle = 4\eta k_B T' \frac{\tilde{T}U}{d\lambda}\delta(y'-y'')\delta(t'-t''), \quad (5.21)$$

$$\langle S_{yx}(y,t)S_{yx}(y',t')\rangle = 2\eta k_B T' \frac{\tilde{T}U}{d\lambda}\delta(y'-y'')\delta(t'-t''), \quad (5.22)$$

so that $\tilde{S}_{yy} = \tilde{S}_{yx} = \sqrt{\eta k_B \tilde{T} U/d\lambda}$. Again, the term that contains $\tilde{S}_{yx}$ is much smaller than the other noise term ($\tilde{S}_{yy}$). Finally, the remaining noise term can be ignored comparing to the viscous form ($P \gg \tilde{S}_{yy}$). Also the terms on the LHS can be ignored so the only dominant term is the pressure. Eqs. (5.17) and (5.18) now become

$$x: \qquad \partial_x p = \partial_y^2 u + \partial_y S_{xy}, \quad (5.23)$$

$$y: \qquad \partial_y p = 0. \quad (5.24)$$

As already said, the fluids we describe are incompressible so that $\vec{\nabla}\cdot\vec{v} = 0$ leads to

$$\partial_x u = -\partial_y v \quad \Longrightarrow \quad \partial_x \int_0^y u\, dy = -v(y). \quad (5.25)$$

Here, no-slip boundary condition, $\vec{v}(y=0) = 0$ has been used. From Eq. (5.24) we see that the pressure does not depend on y explicitly. Therefore we integrate Eq. (5.23) along the vertical coordinate three times between zero to y and we get

$$\frac{y^3}{3}\,\partial_x p = \int_0^y u(y)dy + \int_0^y \int_0^y S_{xy} dy dy'. \quad (5.26)$$

If we derive this equation with respect to x the first term on the RHS becomes $-v$, see Eq. (5.25). Now we recall the boundary condition at the free surface (5.12) and for $y = h(x)$ we obtain

$$\partial_x \frac{h^3}{3}\,\partial_x p = -\partial_t h - u\partial_x h + \partial_x \int_0^y \int_0^y S_{xy} dy dy'. \quad (5.27)$$

Changing back to dimensional variables, the lubrication reads to [17]

$$\eta\partial_t h = \partial_x \left\{ \frac{h^3}{3}\,\partial_x \left[-\gamma\partial_x^2 h - \Pi(h) + \rho g h\right] + \int_0^h dy \int_0^y dy'\, S(x,y',t) \right\}, \quad (5.28)$$

where $S = \mathbf{S}_{xy}$ is the only component of the fluctuating stress tensor that appears at the lowest non-trivial order in the lubrication expansion. As usual [112], the first three terms inside the brackets on the RHS of Eq. (5.28) represent the surface tension, the disjoining pressure, and the gravity force, respectively. Note that, due to the delta-correlations in the fluctuating stress tensor, defined in (5.6), the variance of the noise term in Eq. (5.28) reads

$$\int_0^h dy \int_0^h dy' \int_0^y dy_1 \int_0^{y'} dy_2 \,\langle S(x_1,y_1,t_1)S(x_2,y_2,t_2)\rangle =$$
$$= \frac{\eta k_B T}{3} h^3 \delta(x_1-x_2)\delta(t_1-t_2), \quad (5.29)$$

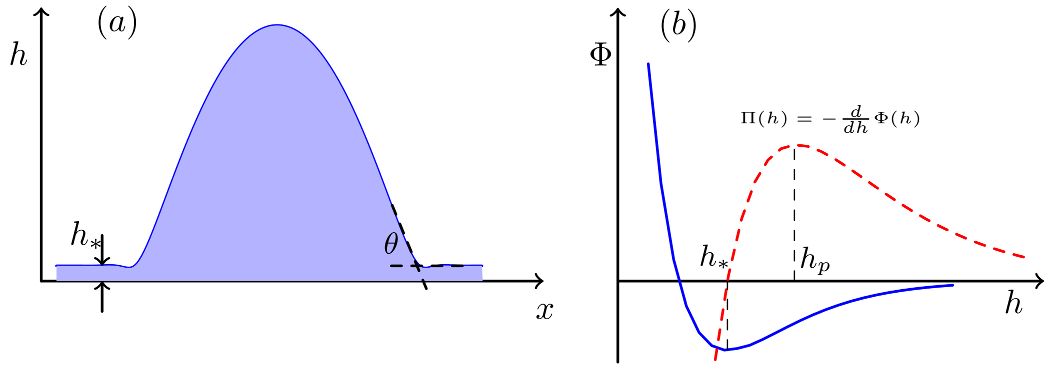

Figure 5.3: a) A droplet with a microscopic liquid layer of thickness h_* partially wets the substrate setting a contact angle θ. b) Potential energy of the vdW interaction (blue line) and its derivative (disjoining pressure, red dashed line).

so that the stochastic lubrication equation (SLE) can be finally written as

$$\eta \partial_t h \;=\; \partial_x \left\{ \frac{h^3}{3}\, \partial_x \left[-\gamma \partial_x^2 h - \Pi(h) + \rho g h \right] + \sigma\, h^{3/2}\, \epsilon(x,t) \right\}, \tag{5.30}$$

where $\sigma = \sqrt{\eta k_B T/3}$ and $\epsilon(x,t)$ is a Gaussian white noise with zero mean and unit variance. For $\sigma = 0$, the well-known deterministic thin film equation is retrieved. The term $h^3/3$ can be seen as describing non-linear diffusion. The exponent 3 comes from the fact that no-slip boundary conditions are used. In general, the diffusion term h^n where $n \leq 3$ describes different physical systems [116]. Physically the case $n = 3$ corresponds to a quadratic increase in velocity over the y axis. We note that there are other ways to derive Eq. (5.30). For instance, by linearizing the deterministic thin film equation and using the fluctuation-dissipation theorem, one is led to the same noise term as in Eq. (5.30) [4]. Likewise, a detailed Fokker-Planck analysis of Eq. (5.28) leads to the conclusion that it describes the same stochastic process as Eq. (5.30). Finally, note that the stochastic lubrication equation (5.30) shows the full dimensional dependence on physical parameters. Particular instances of this equation are studied in detail in the following chapters. Numerical simulations will be performed in appropriate dimensionless units, which will be specified in each particular case.

5.3 Disjoining pressure

A liquid film on a solid substrate forms a contact angle θ [115, 117–120] which can take all the values in the interval $[0, \pi]$. Zero contact angle corresponds to a complete wetting scenario, while angles in the interval $(0, \pi/2)$ indicate that the fluid wets the substrate partially. The case where the contact angle is larger than $\pi/2$ is called dry state. Physically

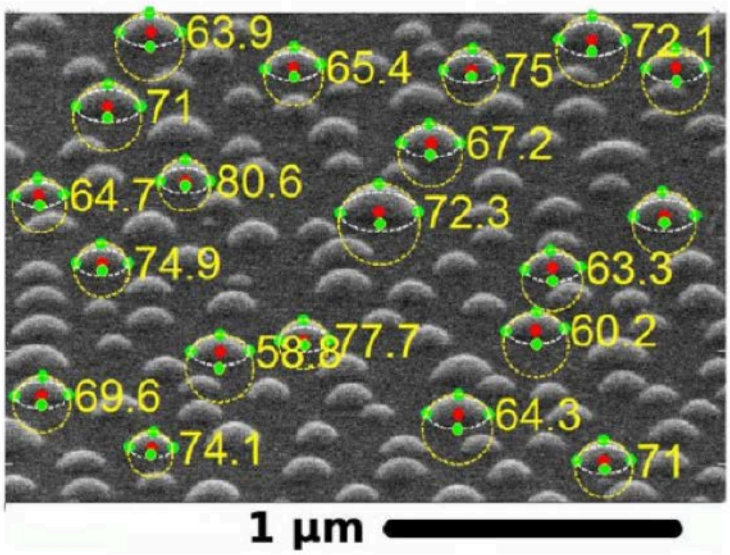

Figure 5.4: A thin solid metal film was exposed to a laser pulse and melted. The dewetting process formed doplets and everything was solidified again when the contact angles were measured. Surprisingly there is a huge variation in contact angle and the authors leave open the dependence of contact angle on the droplet size. Picture from *González et al* [20].

the only difference to partially wetting states is that the vapor and liquid states are interchanged. A well-defined contact angle formes to minimize the free energy of liquid-solid, γ_{SL}, liquid-vapor, γ_{LV} (namely, the surface tension coefficient γ), and solid-vapor, γ_{SV}, interactions. The equilibrium state is energetically the most favorable state of these interactions. The Young's equation [117] gives the microscopical contact angle (on a scale larger than long-ranged intermolecular forces [120]):

$$\gamma_{SV} = \gamma_{SL} + \gamma \cos\theta. \tag{5.31}$$

The spreading parameter $S = \gamma_{SV} - \gamma_{SL} + \gamma$ is defined to describe how strongly the liquid can spread on a surface. Fluids within the lubrication approximation have different morphology so that Young's equation has to be redefined. Namely, it was seen in experiments that films which have partially wetting equilibrium states as a result of spreading or dewetting processes form drops of finite static contact angle between the fluid and the substrate. In such cases, the contact line does not reach the substrate but it rather forms a microscopic layer that is maintained in the state of stable equilibrium due to intermolecular forces. This layer is hardly recognized as the length scales are usually smaller than the wavelength of visible light [108]. Moreover, drops communicate via this layer, which leads to drop coalescence and coarsening [121–126]. The layer itself actually reduces the interactions to liquid-solid and liquid-vapor. The surface tension describes the liquid-vapor interaction while the so-called disjoining pressure accounts for all the molecular liquid-solid interactions [119]. The pressure form sets a microscopic equilibrium height for the corresponding macroscopic layer, also called precursor film. Due to the complexity of intermolecular interactions the disjoining pressure is modelled phenomenologically [108, 127–131]. The liquid and the substrate interact through dipole-dipole interaction, also known as van der Waals (vdW) interaction, in which the potential can take various forms, like e.g. exponential or a step function.. We use, a theoretically simpler, power-law form, $w(r) \sim 1/r^n$. The case, $n = 6$ represents London's dispersion interaction energy between two identical particles, atoms, or molecules [132]. For that case the integral over the whole area gives a decay with respect to the film thickness $\pi(h) \sim A/l^3$, where A is proportional to the Hamaker constant [119]. Positive A corresponds to a repulsive force so that the film tends to increase its thickness. Similarly, an attractive potential can also have power-law form, although more complex forms are have been also studied [127, 131, 133]. In general, the form of the disjoining pressure [108] which is most commonly used reads

$$\Pi(h) = k\left[\left(\frac{h_*}{h}\right)^n - \left(\frac{h_*}{h}\right)^m\right], \tag{5.32}$$

where h_* represents the microscopic layer thickness at which the pressure is zero (energetically the most favorable). Indeed, the first term on the RHS of Eq. (5.32) is repulsive while the second term is attractive, leading to a stable film thickness at $h = h_*$. The pressure also reaches a local maximum at h_p, for which $\Pi'(h_p) = 0$, see Fig.5.3b. The exponents $n > m > 1$ are usually chosen to reproduce physical properties of the system. The surface tension force spreads the drop filling the substrate with the fluid, while the disjoining pressure tends to maintain the microscopic precursor thickness. The interplay between them introduces a fixed macroscopic contact angle, see Fig. 5.3, which is calculated by adjusting the Young-Laplace formula (5.13) for thin films [134]. When the forces are balanced the total pressure at the boundary is zero

$$p = -\gamma c - \Pi(h) = 0, \tag{5.33}$$

where c is the curvature given by Eq. (5.14), which for easier calculus can be rewritten as

$$c(h) = \frac{d}{dh}\left[(1 + \partial_x h^2)^{-1/2}\right]. \tag{5.34}$$

Integrating Eq. (5.33) over h from the microscopic precursor thickness h_* up to some large value H one obtains (note that the partial derivative, $\partial_x h = \tan h$, represents zero contact angle at the precursor and θ at the height H)

$$\cos\theta = 1 - \frac{1}{\gamma}\int_{h_*}^{H} \Pi(h)dh. \tag{5.35}$$

The integral on the RHS (when $H \to \infty$) actually represents the spreading parameter. The disjoining pressure above the precursor line is always negative as the attractive force is dominant which corresponds to positive spreading parameter and a partial wetting scenario. For arbitrary coefficients m and n the integral is

$$\Omega(h) = -\int_{h_*}^{h} \Pi(h) dh \;=\; -\,kh_* \left[\frac{1}{n-1} \left(\frac{h_*}{H} \right)^{n-1} - \frac{1}{m-1} \left(\frac{h_*}{H} \right)^{m-1} \right] \Bigg|_{h_*}^{H} = \\ = -\,kh_* \left[u(H) - u(h_*) \right], \tag{5.36}$$

where $u(h \to \infty) = 0$ and $u(h_*) = (m-n)/[(m-1)(n-1)] = M$. Finally, we get the Young-Laplace equation for thin films

$$\cos\theta \;=\; 1 - \frac{Mkh_*}{\gamma}. \tag{5.37}$$

This relation gives a fixed contact angle depending on the surface tension and Hamaker constant, and the election of exponents in the vdW potential (5.32), is derived assuming that only surface tension and vdW force determine the shape of the surface. The question that arises now is how fluctuations would affect this relation. This was one of the key topics of this thesis and the whole analysis is given in Chap. (7).

6

Numerical integration of the SLE

6.1 The algorithm for the $2d$ SLE

The stochastic lubrication equation (SLE) we derived in the previous chapter is a fourth-order partial differential equation that describes the time evolution of the film thickness. The complexity of the terms stands out when standard numerical schemes are applied. In this chapter we describe the algorithm we have employed to simulate the evolution when fluctuations are taken into account. For simplicity, we use a non-dimensional form of the SLE (5.30). The rescaling we have implemented and physical systems of reference are described in detail in the last section of this chapter. We ignore gravity as, being second order in space, it can be easily implemented explicitly once the algorithm is complete. The non-dimensional SLE we consider is

$$\eta\partial_t h \;=\; \partial_x \left\{ D(h)\,\partial_x \left[-\partial_x^2 h - \Pi(h)\right] + \sigma\, h^{3/2}\,\epsilon(x,t) \right\}, \tag{6.1}$$

where the diffusion coefficient is $D(h) = h^3/3$. A detailed derivation of the non-dimensional equation from the SLE is given the last section of this chapter. We could have ignored the disjoining pressure but we have left it for physical reasons. Regarding the positivity preserving solutions, the problem to develop an algorithm is somehow similar to the one we faced when developing algorithm to simulate the sFKPP equation (Chapter 3). Again, the numerical solution of Eq. (6.1) could change the sign even if the initial condition is positive everywhere. The problem lies in the region where diffusion vanishes ($h \to 0$)

especially when the system is discretized [135]. There are many ways to overcome this problem by regularizing the diffusion term or by introducing a relaxing, no slip-boundary condition which leads to modified diffusivity. Here, we use a simple implicit algorithm based on a precursor film so that the surface height remains non-zero everywhere. It was seen that liquid films have a macroscopic thin-film layer (see the last paragraph in the previous chapter) so we could simply define that layer to be our precursor film.

We first discretize space choosing a grid with L points where the distance between neighboring points is Δx. We need to linearize the fourth-order term, so that we can solve it numerically. We use a centered finite difference scheme in which the first derivative of h at a point i on the grid is a difference between two midway points $i + 1/2$ and $i - 1/2$. We introduce discretized terms f_i and g_i on the RHS of Eq. (6.1) as

$$\partial_t h \, + \, f_i + g_i = 0, \quad \text{where} \quad f_i = \left[\partial_x \, \frac{h^3}{3} \, \partial_x^3 h\right]_i \tag{6.2}$$

$$\text{and} \quad g_i = \partial_x \left\{ \frac{h^3}{3} \, \partial_x \Pi(h) \, + \, \sigma \, h^{3/2} \, \epsilon(x,t) \right\}_i . \tag{6.3}$$

Due to the fourth derivative, function f_i will be treated implicitly while function g_i can be treated explicitly without loss of precision of the solution. The function f_i depends on the five neighboring grid points,

$$f_i = \sum_{j=-2}^{2} a_j h_{i+j}. \tag{6.4}$$

where the coefficients a_j contain the diffusion terms $D(h)$. The full list of the coefficients a_j is given in Appendix A.1. The positivity-preserving property of the numerical scheme depends on the correct choice of the discretization for the diffusion terms [136,137]. In our case, the existence of a precursor film allows us to simply use centered finite-differences to define the diffusion at the midway points, namely,

$$D_{i\pm 1/2} = \frac{1}{2} \left[D(h_i) \, + \, D(h_{i\pm 1}) \right] . \tag{6.5}$$

The time derivative is also discretized using the standard method so that finally, the fully discretized equation (6.1) reads

$$\frac{h_i^{\nu+1} - h_i^{\nu}}{\Delta t^{\nu}} \, + \, \theta f_i^{\nu+1} + (1-\theta) f_i^{\nu} + g_i = 0 \tag{6.6}$$

The superscript ν denotes time step and $\Delta t^{\nu} = t^{\nu+1} - t^{\nu}$. The function $f_i^{\nu+1}$ is evaluated at the current time step $t^{\nu+1}$, while f_i^{ν} is at the previous one, t^{ν}. Three typical values that θ takes are

- $\theta = 0$: explicit, forward Euler scheme.
- $\theta = 1$: implicit, backward Euler scheme.
- $\theta = 1/2$: implicit, Crank-Nicholson scheme.

Here, we always use $\theta = 1/2$. Another important element to be implemented are the boundary conditions. As the surface evolution at every point depends on the two neighbors from each side we have to add two ghost points to each end point of the grid, see Fig. 6.1. In our case we use zero-flux boundary conditions, namely both the first and the third derivatives at the points 0 and L are set to zero.

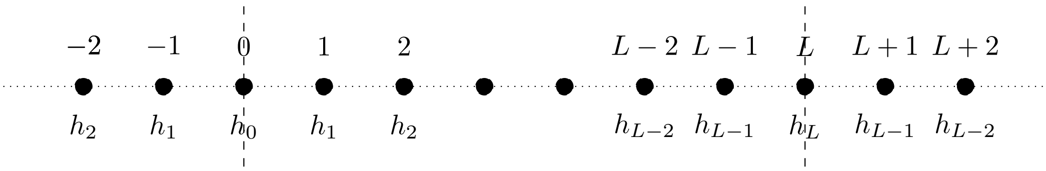

Figure 6.1: A grid with two ghost points and zero-flux boundary conditions.

The problem now is how to integrate Eq. (6.6), as the function $f_i^{\nu+1}$ also depends on the solution at the current time step, making the equation a non-linear algebraic system of equations for the unknown variables $h_i^{\nu+1}$. To solve this, we use the Newton-Kantorovich iterative method [138]. We define a functional

$$F(h_i^{\nu+1}) = h_i^{\nu+1} - h_i^{\nu} \; + \; \Delta t^{\nu}\theta f_i^{\nu+1} + \Delta t^{\nu}(1-\theta) f_i^{\nu} + \Delta t^{\nu} g_i, \tag{6.7}$$

which is zero when $h_i^{\nu+1}$ is a solution to Eq. (6.6). We do not know the solution, but we can employ a guess for it and check how far it is from the real solution. If our initial guess is $h_i^{\nu+1}$, then there is a correction q_i, so that the solution is $h_i^{\nu+1} + q_i$, which corresponds to $F(h_i^{\nu+1} + q_i) = 0$. Now, to find the correction q_i we approximate F by a linear function of a small parameter δ_i around $h_i^{\nu+1}$ to get

$$F(h_i^{\nu+1} + \delta_i) = F(h_i^{\nu+1}) \; + \sum_{j=i-2}^{i+2} \frac{\partial F}{\partial h_j^{\nu+1}} q_j = 0 \tag{6.8}$$

where the derivative of $F(h_i^{\nu+1})$, see Eq. (6.7), is

$$\frac{\partial F(h_i^{\nu+1})}{\partial h_j^{\nu+1}} \; = \delta_{ij} + \frac{\partial f_i}{\partial h_j^{\nu+1}} \Delta t \theta \, q_j. \tag{6.9}$$

The derivatives of f_i with respect to $h_j^{\nu+1}$ are obtained through straight-forward calculus, and the values are also given in Appendix A.1. Eq. (6.7) is an algebraic coupled system of equations with unknown variables q_i. When we solve the system and find all q_i, we are "supposed" to be closer to the solution. Here "supposed" means that there is no criteria to guarantee the convergence, in particular if the initial guess is not good enough the solution of the system (6.9) could go in the wrong way. In theory if an iteration moves the solution closer to the real solution, the functional F will decrease. We use the new solution $h_i^{\nu+1} + q_i$ as an initial guess and repeat the process until finally the functional gets close to zero, which in practice is defined to be smaller than a given tolerance (in all simulations 10^{-10}).

Every equation has five unknown neighboring variables. hence we can rewrite the system in the penta-diagonal matrix form

$$\vec{r} = (\mathbf{I} + \Delta t\theta \mathbf{A})\vec{q}, \tag{6.10}$$

where $\mathbf{I}$ is the identity matrix, $\vec{r} = (F(h_i^{\nu+1}))^T$, $\vec{q} = (q_0, \cdots, q_L)^T$. The matrix $\mathbf{A}$ is constructed from the second term on the RHS of Eq. (6.9) and reads

$$\mathbf{A} = \begin{pmatrix} a_{11} & 2a_{12} & 2a_{13} & 0 & \cdots & \cdots & 0 \\ a_{21} & a_{22}+a_{23} & a_{23} & a_{23} & \ddots & & \vdots \\ a_{31} & a_{32} & \ddots & \ddots & \ddots & \ddots & \vdots \\ 0 & a_{42} & \ddots & \ddots & \ddots & a_{L-3,L-1} & 0 \\ \vdots & \ddots & \ddots & \ddots & \ddots & a_{L-2,L-1} & a_{L-2,L} \\ \vdots & & \ddots & a_{L-1,L-3} & a_{L-1,L-2} & a_{L-1,L-2}+a_{L-1,L-1} & a_{L-1,L} \\ 0 & \cdots & \cdots & 0 & 2a_{L,L-2} & 2a_{L,L-1} & a_{L,L} \end{pmatrix} \tag{6.11}$$

where a_{ij} corresponds to a function of a_{i-j} from Eq. (6.4) (one-dimensional systems), given in Appendix A.1. The coefficients at positions $(1, 2)$, $(1, 3)$, $(L, L-1)$, $(L, L-2)$, as well as the terms at $(2, 2)$ and $(L-1, L-1)$, are the result of applying the zero-flux boundary conditions to Eq. (6.9). The boundary conditions have to be also implemented into the coefficients a_{11}, a_{12}, a_{LL} and a_{LL-1} as they contain ghost points h_{-1}, h_{-2} and h_{L+1}, h_{L+2}. Note that, if instead of zero-flux, periodic boundary conditions were used, the matrix $\mathbf{A}$ would not have exactly a penta-diagonal form. The first two terms in the last row, the first term in the row above, and also the last two in the first row plus the last in the second row would be different from zero.

Now we need a proper (rapid) tool to solve the algebraic system of equations (6.10). It could be done by any iterative method such as conjugate or biconjugate gradient method but as the matrix is so well structured (penta-diagonal elements always different from zero) we could simply diagonalize the matrix $\mathbf{A}$ using the Gauss method. Finally we have everything to get a new solution $h_i^{\nu+1}$ at the time step $t^{\nu+1}$, using the previous solution h_i^{ν} as an initial condition and solving Eq. (6.6) through the iterative process (6.9). There are two additional problems one needs to be aware of. As we already said, the Newton-Kantorovich iterative method may not converge. Another problem arises if the time step is too large, which leads to large error in discretization. The time discretization assumes a linear approximation in time. Hence, the second (derivative) term in the Taylor expansion determines the error

$$e_i = \frac{(\Delta t^{\nu})^2}{h_i^{\nu}} \frac{d^2 h_i^{\nu}}{dt^2}, \tag{6.12}$$

which after the discretization becomes

$$e_i = \frac{(\Delta t^{\nu})^2}{h_i^{\nu-1}} \frac{\Delta t^{\nu-1} h_i^{\nu+1} + \Delta t^{\nu} h_i^{\nu-1} + (\Delta t^{\nu-1} + \Delta t^{\nu}) h_i^{\nu}}{(\Delta t^{\nu} + \Delta t^{\nu}) h_i^{\nu}}. \tag{6.13}$$

In general, different areas of the film have different values of the error. Therefore, we look for the maximum value of the error which we compare to some small value (usually 10^{-2} or 10^{-3}) in order to achieve good precision.

To summarize, here we give a brief description on how to implement all the elements described to build up a properly working algorithm in two space dimensions. The key process is to solve Eq. (6.10). Once the system is properly discretized and the time step Δt^{ν} is chosen, we calculate the elements of the matrix A (coefficients a_{ij} in Appendix A.1) and the vector $\vec{r}$ using the solution in the previous time step for the very first iteration or the solution after the previous iteration as the next guess ($h_i^{\nu+1} = h_i^{\nu}$). We solve Eq. (6.10) using the Gauss method and we form a new solution as $h_i^{\nu+1} = h_i^{\nu+1} + q_i$. This is an iterative process that requires the following checks:

- First we check that the new solution is not negative at any point. If this is not the case we discard it, go back to the beginning of the iterative process ($h_i^{\nu+1} = h_i^{\nu}$) and reduce the time step by half ($\Delta t^{\nu} = \Delta t^{\nu}/2$).
- If the number of iterations is larger than 4, we go back to the beginning and reduce the time step by half.
- If the solution is not negative and iteration number is smaller than 4, we check if the solution has converged (max$(F(h_i^{\nu+1} + q_i) < 10^{10})$. If it is not the case, we continue the iteration process and annotate the total number of iterations. If it has converged we need additional checks to insure that the converged solution is a good one:
  - The fluid volume has to be conserved: $|V(h^0) - V(h^{\nu})|/V(h^0) < 10^{-3}$.
  - The time derivative error e_i has to fulfill max$(e_i) < 10^{-3}$.
  - If all the conditions are fulfilled for the last 100 time steps we could increase the time step by one percent, $\Delta t^{\nu} = \Delta t^{\nu} + 0.01\Delta t^{\nu}$.

After all these conditions are fulfilled and the solution at $t^{\nu+1}$ is obtained, it becomes an initial condition for the next time step and the procedure is repeated. For stochastic systems ($\sigma \neq 0$), a problem may appear that further limits the error in the time derivative. Since at every time step we are sampling new random variables, the error (6.13) is expected to be much larger than for deterministic system. This fact may significantly slow down the simulation by requiring a smaller time step in order to achieve an error which is smaller enough.

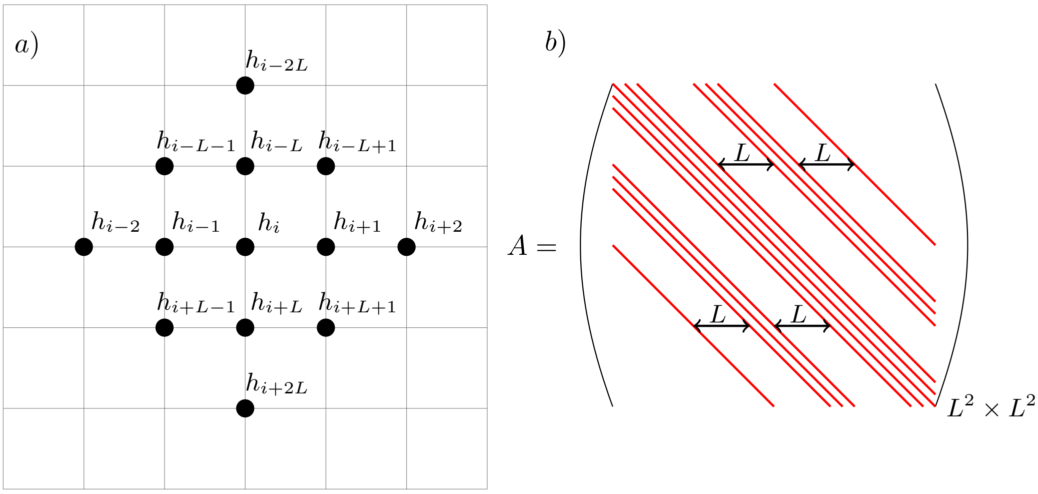

Figure 6.2: $a)$ Grid points for a $3d$ SLE. Spatially discretized points $h(x_i, y_j)$ are represented in vectorial form so that $h_{i,j} = h_{i+L\cdot j}$. $b)$ The matrix $\mathbf{A}$ for a $3d$ SLE with zero-flux boundary conditions has 13 non-zero diagonals.

6.2 $3d$ Algorithm

Here we briefly mention the novelties and the difficulties one faces in order to produce an algorithm that simulates stochastic thin liquid films in three space dimensions. The interested reader should have understood completely the previous sections in order to go through the present one.

To simulate the SLE in $3d$, the process is similar to the $2d$ case beyond one small thing that numerically increases a lot the calculation time substantially [139]. Namely, the surface tension term in $3d$ reads

$$\vec{\nabla}(D(h)\vec{\nabla}\nabla^2 h) = \frac{\partial}{\partial x}\left(D(h)\frac{\partial^3}{\partial x^3}h\right) + \frac{\partial}{\partial y}\left(D(h)\frac{\partial^3}{\partial y^3}h\right) + \\ + \frac{\partial}{\partial x}\left(D(h)\frac{\partial^3}{\partial x \partial y^2}h\right) + \frac{\partial}{\partial y}\left(D(h)\frac{\partial^3}{\partial x^2 \partial y}h\right). \tag{6.14}$$

For simplicity, we will assume that our grid is a square lattice with L^2 elements. Now we have four terms to discretize. Together they introduce 13 neighboring points to a reference one, see Fig. 6.2(a), while for $2d$ we only had 5 [recall Eq. (6.4)]. Then repeating all the steps from Eq. (6.5) to Eq. (6.10) we end up with an algebraic system of equation where the vector $\vec{r}$ has L^2 components and the matrix I and A have $L^2 \times L^2$ dimensions,

$$\vec{r} = (\mathbf{I} + \Delta t\theta(\mathbf{A_x} + \mathbf{A_y} + \mathbf{A_{xy}}))\vec{q}, \tag{6.15}$$

where $\mathbf{A_x}$ and $\mathbf{A_y}$ correspond to the first two terms on the RHS of Eq. (6.14) respectively, while $\mathbf{A_{xy}}$ corresponds to the two remaining terms (mixed derivative terms). If we define

$\vec{r} = (F(h_{11}^{\nu+1}), \cdots, F(h_{1L}^{\nu+1}), F(h_{21}^{\nu+1}), \cdots, F(h_{2L}^{\nu+1}), \cdots, F(h_{LL}^{\nu+1}))^T$, then the matrix $\mathbf{A_x}$ remains penta-diagonal, while $\mathbf{A_y}$ is transposed penta-diagonal. The mixed derivative matrix has off-diagonal, elements so that the sum $A_x + A_y + A_{xy}$ has a form as in Fig. 6.2(b). Due to the off-diagonal elements, it would be very costly to solve the system (6.15) using Gauss method. Iterative methods are better, but still this matrix is too large for the systems we want to simulate ($L \simeq 10^3$). There is an alternative method which approximates the sum of matrices

$$(\mathbf{I} + \Delta t\theta(\mathbf{A_x} + \mathbf{A_y} + \mathbf{A_{xy}})) \simeq [\mathbf{I} + \Delta t\theta\mathbf{A_x}][\mathbf{I} + \Delta t\theta\mathbf{A_y}]. \tag{6.16}$$

This method is called alternating direction implicit (**ADI**) scheme [140–144]. If we apply the approximation (6.16) to Eq. (6.15) we get

$$\begin{aligned}\vec{r} &= [\,\mathbf{I} + \Delta t\theta\mathbf{A_y}\,]\,\vec{\omega}\\ \vec{\omega} &= [\,\mathbf{I} + \Delta t\theta\mathbf{A_x}\,]\,\vec{q}.\end{aligned} \tag{6.17}$$

This is much easier to solve as we simply have to perform Gauss method twice to solve two penta-diagonal systems with L^2 unknowns.

All the checks stated in the previous section are the same here. The **ADI** method approximates the matrix $\mathbf{A}$. Usually, for a same time step in $3d$, it will take more Newton iterations to converge than it would for a $2d$ system. Still it is an important advantage as the calculation time is strongly reduced as compared to any iterative solution of Eq. (6.15).

6.3 Non-dimensional SLE

Numerical simulations are always easier in dimensionless units as one does not have to worry about scales every time a simulation is performed. Moreover, non-dimensional parameters and dynamics can be compared in general to appropriate physical systems. Here we present the rescaling we have elected to use to obtain the non-dimensional equation (6.1). First, for as easier presentation let us recall the $3d$ stochastic thin film equation

$$\eta\partial_t h \;=\; \vec{\nabla}\left\{\frac{h^3}{3}\,\vec{\nabla}\left[-\gamma\nabla^2 h - \Pi(h)\right] + \sigma\, h^{3/2}\,\epsilon(x,y,t)\right\}, \tag{6.18}$$

where $\sigma = \sqrt{\eta k_B T/3}$ and $\epsilon(x,y,t)$ is a Gaussian white noise with unit variance. We rescale all the space variables by a physical film thickness h_c and the time coordinate by a time scale t_c (which will be chosen later) so that out non-dimensional coordinates are

$$\hat{h} = h/h_c, \quad \hat{x} = x/h_c, \quad \hat{y} = y/h_c, \quad \hat{t} = t/t_c. \tag{6.19}$$

If we implement these back into Eq. (6.18) we have

$$\frac{\eta h_c}{t_c}\partial_{\hat{t}}\hat{h} \;=\; \frac{1}{h_c}\hat{\vec{\nabla}}\left\{\frac{h_c^2}{3}\hat{h}^3\,\hat{\vec{\nabla}}\left[-\frac{\gamma h_c}{h_c^2}\hat{\nabla}^2\hat{h} - \Pi(\hat{h})\right] + \sigma\, h_c^{3/2}\hat{h}^{3/2}\,\frac{1}{h_c t_c^{1/2}}\epsilon(\hat{x},\hat{y},\hat{t})\right\}. \tag{6.20}$$

To simplify the equation, we divide everything by $\eta h_c/t_c$ so that

$$\partial_{\hat{t}}\hat{h} \;=\; \partial_{\hat{x}} \left\{ h^3\,\partial_{\hat{x}} \left[-\frac{\gamma t_c}{3\eta h_c}\partial^2_{\hat{x}}\hat{h} - \hat{\Pi}(\hat{h}) \right] + \underbrace{\sigma\,\frac{t_c^{1/2}}{\eta h_c}}_{\hat{\sigma}}\,\hat{h}^{3/2}\,\epsilon(\hat{x},\hat{t}) \right\}. \tag{6.21}$$

Eq. (6.21) is a non-dimensional form of the SLE (6.18). Finally, we have to specify the time scale. We take $t_c = 3\eta h_c/\gamma$, as it sets the non-dimensional surface tension to unity. The non-dimensional disjoining pressure and the Hamaker constant then become

$$\hat{\Pi}(\hat{h}) \;=\; \frac{\hat{A}}{\hat{h}^2} - \frac{\hat{B}}{\hat{h}^3}, \tag{6.22}$$

where $\hat{A} = 3A/\gamma h_c^2$ and $\hat{B} = 3B/\gamma h_c^3$ (the relation $A = Bh_*$ sets the precursor film at h_*, Sec. 5.3). The time scale determines the non-dimensional noise strength $\hat{\sigma} = (k_B T/\gamma h_c^2)^{1/2}$. The same scaling properties are used for the $2d$ SLE in [18, 145] as the assumption that the system approximately remains translationally invariant in one direction. Similarly, in [4] $1d$ drops are assumed to be confined in a channel of width W, so that the non-dimensional noise strength is $\hat{\sigma} = (k_B T/\gamma h_c W)^{1/2}$.

We have also performed simulations of a system in the gravity-dominated regime. The results are presented in Sec. 7.2. To rescale properly the SLE for that regime we take the same steps as above, now choosing the time scale as $t_c = 3\eta/\rho g h_c$. The non-dimensional noise strength becomes $\hat{\sigma} = (k_B T/\rho g h_c^4)^{1/2}$.

6.4 Physical systems vs non-dimensional parameters

In this thesis we present numerical results for different physical situations. Therefore, it is convenient to state them here together with the values of the physical parameters which we will be considering. Note that the parameters used in our simulations are always non-dimensional.

Gravity-driven systems

We have simulated a $1d$ drop of initial height $h_0 = 1$ that spreads under the influence of gravity. In the simulations discussed in Section 7.2, the grid space is $\Delta x = 0.05$, the regularizing precursor layer of thickness is $h_* = 0.01$, and the time step is limited to $\Delta t = 0.01$. The domain size is $L = 1000$. In this case, the vdW force and the surface tension are neglected, therefore the regularizing precursor does not have a physical interpretation. It only serves to maintain positivity of the solution.

The main idea of simulating gravity-driven systems is to check the validity of the scaling assumption made in Davidovitch *et al.* [4] for surface-tension-driven systems.

Nevertheless, we have compared our parameters to the colloid-polymer mixtures studied in [146, 147], where $\rho g \simeq \gamma/h_c^2$, $\gamma \lesssim 1$ μN/m, and $h_c \simeq 10$ μm. Hence, at room temperature $T = 300$ K, the dimensionless noise amplitude is $\hat{\sigma} \simeq 0.05$, even slightly larger than the value employed in our simulations. The region where fluctuations dominate the spreading process is where they are comparable to the droplet height. Contrary to the surface-tension-dominated regime, the low orders of spatial derivatives in the gravity-dominated regime lead to large (unphysical) fluctuations in the precursor layer. In order to avoid non-positivity issues, we switch off the noise at positions where the droplet height is less than half its value at the center of the droplet.

Droplets at fixed contact angle

The influence of fluctuations on the contact angle is studied in Sec. 7.3. An initial drop of height $h_0 = 1$ is allowed to spread until a non-zero contact angle sets in, due to the interplay between surface tension and the vdW force. The parameters are $\Delta x = 0.05$, $\Delta t = 0.01$, $L = 500$. The precursor thickness is set to $h_* = 0.05$. For different values of the contact angle the non-dimensional Hamaker constant was calculated using Eq. (5.37). Here, in order to unambiguously identify the influence on the dynamics of thermal noise in the distribution of molecular velocities, we approximate γ by a temperature-independent value. In general the value of the surface tension can depend non-trivially on temperature.

In [20] dewetting of metal thin films is experimentally studied. Copper films of thickness $h_c \in [5, 15]$ nm were exposed to a laser pulse whose energy was selected to ensure that the film reaches the melting point, $T = 2000$ K. Once the film is melted, it dewets forming a pattern of drops. The experiment is performed to find the Hamaker constant of the material and also to compare different vdW potentials. The films have $\gamma = 1.3$ N/m, and $h_c \in [5, 15]$ nm, so that the non-dimensional noise strength is $\hat{\sigma} \in [10^{-2}, 3 \cdot 10^{-2}]$. A variation of 7° in contact angle is seen and the authors leave open the possible dependence of the contact angle on the drop size, which is not accounted for by the standard lubrication theory. As we will see in the next chapter, fluctuations do introduce a variability in contact angle, but only for small angle values.

7

Stochastic thin film spreading

In this chapter we present our study on droplet spreading under different physical conditions. The results presented here are published in [148]. Usually, the spreading is considered to be driven by surface tension and gravity forces, represented in the SLE model by the first and third terms inside the brackets on the RHS of Eq. (5.30) which for easier presentation we also recall here

$$\eta\partial_t h \;=\; \partial_x \left\{ \frac{h^3}{3}\,\partial_x \left[-\gamma\partial_x^2 h - \Pi(h) + \rho g h\right] + \sigma\, h^{3/2}\,\epsilon(x,t) \right\}. \tag{7.1}$$

If partial wetting (non-zero contact angle) is to be considered, one possibility is to include in the model the disjoining pressure that results from the balance between attractive and repulsive contributions to the interface potential induced by van der Waals interactions (described in detail in Sec. 5.3). Such an approach allows to describe accurately film break-up and droplet formation through the occurrence of morphological instabilities under e.g. dewetting conditions [108]. The disjoining pressure interrupts droplet spreading or contraction and sets a fixed macroscopic contact angle. We will consider such a process in Sec. 7.3. In the following section, we will focus on spreading of completely wetting droplets (zero contact angle), therefore the disjoining pressure will be omitted.

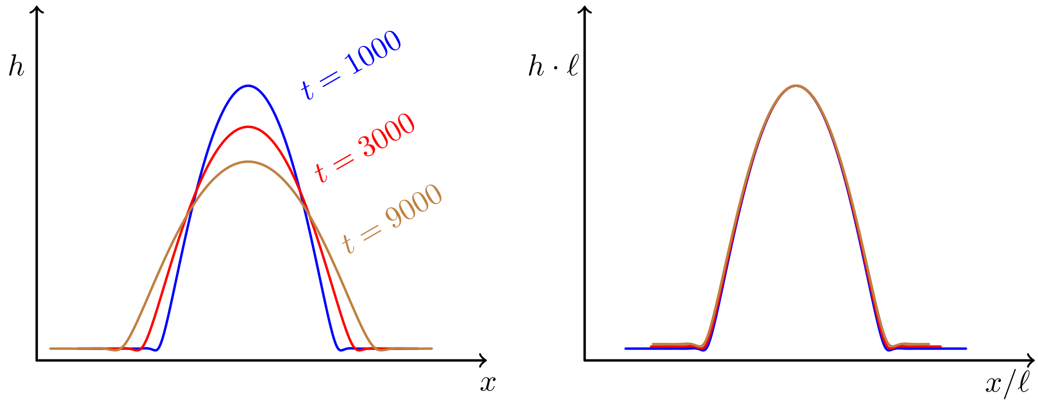

Figure 7.1: Left: The evolution of a film at different times. Right: Rescaling the width and the height of a droplet by ℓ leads to collapse of the drops.

7.1 Scaling properties of the SLE

As is well known, the spontaneous spreading of a fluid droplet under the action of deterministic forces (surface tension, gravity, etc.) leads to a power-law scaling of a typical length-scale, like e.g. the droplet width ℓ, as $\ell(t) \sim t^n$ [149]. The droplet width is usually defined as the second moment of the surface distribution,

$$\tilde{\ell}(t) = \left\langle \left[\frac{1}{V} \int dx (x - \tilde{X})^2 h(x,t) \right]^{1/2} \right\rangle = c\, t^n, \tag{7.2}$$

where

$$\tilde{X} \;=\; \frac{1}{V} \int h(x,t)\, x\, dx \tag{7.3}$$

is the instantaneous position of the droplet center, V is the total droplet volume, which remains constant in time, and $\langle \cdots \rangle$ represents an average over realizations of the noise $\epsilon(x,t)$ when fluctuations are accounted, while for the deterministic case there is no average. This is the content of Tanner's law [120, 149], where the value of the exponent n depends on the specific relaxation term which is assumed, e.g. $n = 1/7$ for surface-tension-dominated flow. Mathematically, this spreading law is related to the existence of similarity solutions to the corresponding thin film equation [135]. Using an argument on self-similarity of solutions to the SLE (7.1), in [4] stochastic fluctuations were shown to modify the spreading exponent value to $n = 1/4$ for surface-tension driven flow. Here, our goal is to generalize the arguments in [4] for a more general SLE, Eq. (7.1), neglecting (for now) the disjoining pressure contribution.

Inspired by the success of scaling analysis to describe the long-time behavior of non-equilibrium interfaces in the presence of fluctuations [1], in [4] the effect of a rescaling of coordinates and fields in the SLE with surface tension only term, was considered. In particular, in that work one considered the behavior under the change of variables

$$x = b\tilde{x} \quad t = b^z\tilde{t} \quad h = b^\alpha\tilde{h}, \tag{7.4}$$

where $b > 1$ is an arbitrary factor, and α and z are constants that remain to be fixed. Similar scaling relations were introduced in Sec. 1.3 to study continuum surface growth models. In the more general case considered here, the various terms on the RHS of Eq. (5.30) scale differently under this operation. In the rescaled coordinates, the ensuing SLE takes on the exact same form as Eq. (5.30), but with modified parameters

$$\begin{aligned} \widetilde{\gamma/\eta} &= (\gamma/\eta)\, b^{z+3\alpha-4}, \\ \widetilde{\rho g/\eta} &= (\rho g/\eta)\, b^{z+3\alpha-2}, \\ \widetilde{\sigma/\eta} &= (\sigma/\eta)\, b^{(z-3+\alpha)/2}, \end{aligned} \tag{7.5}$$

No matter at what stage of the time evolution, the fluid volume

$$V(t) \;=\; b^{1+\alpha} \int h(x,t)dx, \tag{7.6}$$

must be conserved at all times which requires $\alpha = -1$, independently of the physical forces considered. The remaining coefficient, z, can be obtained by requesting that the rescaled SLE remains unchanged, thereby imposing statistical self-invariance [1], namely, the dynamics and fluctuations of the rescaled height field

$$\tilde{h}(x,t) \;=\; b^{-\alpha}h(bx, b^z t), \tag{7.7}$$

will be indistinguishable from those of $h(x,t)$ [29]. In principle, such an invariance can strictly hold only if a single term occurs in the equation, leading to $z = 7,\ 5,\ 4$ if that term is due to surface tension, gravity, or the noise contribution, respectively. If two terms occur simultaneously, e.g. surface tension and noise, as studied in [4, 17], Eq. (7.5) provides expectations on the relevance of each term during the system evolution. Thus, $z = 7$ as dictated by surface tension implies $\tilde{\sigma} > \sigma$, suggesting that stochastic fluctuations will become more and more relevant at increasing time and length scales. We note in passing that this scaling argument can be generalized to any deterministic relaxation term in the SLE whose linearized form is proportional to $\partial_x^m h$ for any $m > 1$; it can be easily checked that the corresponding rescaled parameter grows as b^{z-3-m}, to be compared with b^{z-4} for the noise.

Consider now a spreading problem, such that a droplet of initial width $\ell(t = 0)$ evolves under Eq. (5.30). Statistical self-similarity under Eq. (7.4) implies that, if we rescale time by a factor c, the system configuration only remains statistically invariant provided length scales are rescaled by a factor $c^{1/z}$. Hence, rescaling Eq. (7.2) we obtain

$$\tilde{\ell}(\tilde{t}) = \left\langle b\left[\frac{1}{V}\int dx(x-\tilde{X})^2 h(x,t)\right]^{1/2}\right\rangle = \left(\frac{\tilde{t}}{t}\right)^{1/z}\ell(t). \tag{7.8}$$

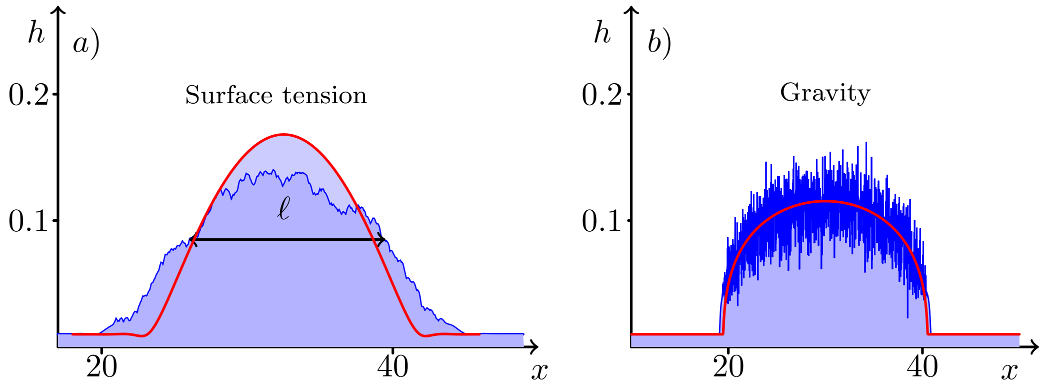

Figure 7.2: Deterministic and stochastic droplets in the surface-tension (a) and gravity (b) dominated flows, starting from the same initial condition. In both cases the thick red solid line corresponds to the deterministic solution, while the thin blue line corresponds to a single realization of a droplet, as described by the corresponding SLE. In both cases fluctuations speed up spreading, the effect being larger in the surface tension dominated system. Note the different scales employed for the horizontal x and vertical h axes.

Hence, if we fix time t to the initial time value t_0 and evolve the system up to time $\tilde{t}$ we obtain the stated power-law, $\ell(t) \sim t^{1/z}$. Indeed, when surface tension dominates, we obtain the well-known Tanner's law [149], where $\ell(t) \sim t^{1/7}$. However, as noted above, there is a long-time regime $t \gg 1$ such that noise fluctuations dominate over the deterministic relaxation. In that regime we find $\ell \sim t^{1/4}$, implying much faster spreading due to thermal fluctuations. This result was explicitly confirmed numerically in [4] by simulating the corresponding SLE, Eq. (5.30) without gravity or disjoining pressure. Figure 7.2(a) shows a comparison between droplet spreading by surface tension only, and if thermal fluctuations are additionally considered. The simulations have been carried out as in [4], in dimensionless units for which the height of the initial droplet is unity, see Fig. 7.1.

7.2 Influence of fluctuations on gravity-driven droplet spreading

The discussion from the preceding section leads one to expect a droplet spreading law of the type $\ell \sim t^{1/5}$ when the process is induced by gravity alone. Note that this is a faster spreading rate than Tanner's law for surface-tension driven flow. In turn, if we allow for thermal fluctuations, we still expect noise to dominate the long-time evolution, where the spreading law crosses to the $\ell \sim t^{1/4}$ behavior. With respect to specific situations in which such type of crossover dynamics might be observed, a natural context could be ultra-low surface tension fluids, such as suitable colloid-polymer mixtures [146, 147].

In this section we explicitly test the scaling hypothesis in such a gravity-dominated regime, in order to confirm that fluctuations change the spreading law in an observable

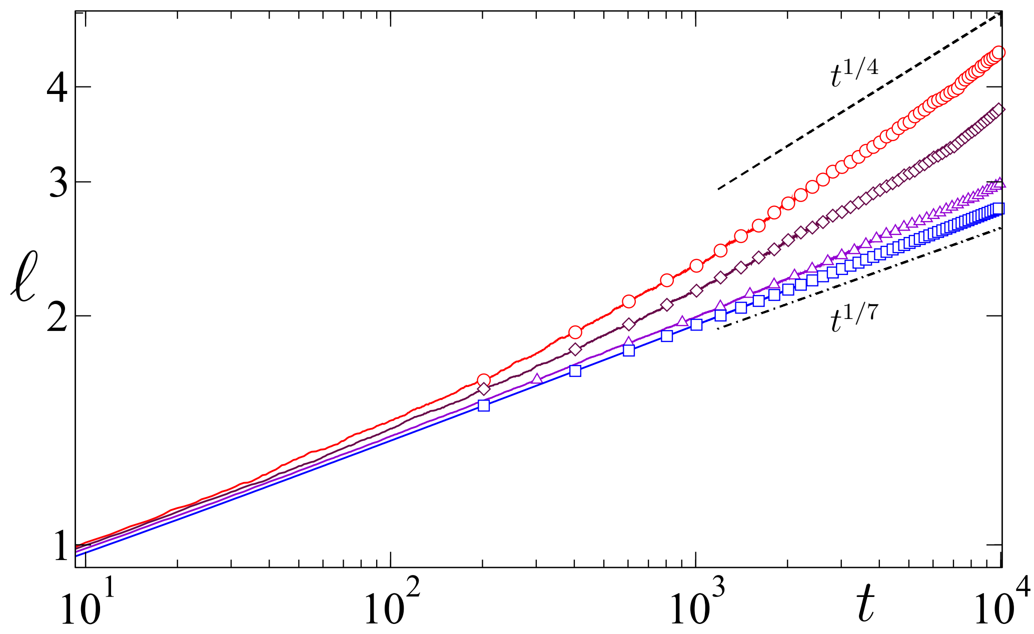

Figure 7.3: Simulations show that the width of stochastic droplet increases faster than for deterministic counterparts, obeying a power-law $\ell \sim t^{1/4}$. For the surface tension driven case, the stochastic curves are averaged over 50 realizations for each noise strength value. The parameters used are $\Delta x = 0.05$, $h_* = 0.01$, and $L = 1000 * \Delta x$, while the initial droplet profile is given by $h(x, t_0) = h_0 e^{-(x-\hat{X})^4} + h_*$ with $h_0 = 1$. Blue squares represent deterministic droplet, violet triangles $\sigma = 0.01$, maroon diamonds $\sigma = 0.022$, and red circles $\sigma = 0.032$. All lines are guides to the eye. Black dashed and dot dashed lines are theoretical predictions.

manner. Working as above in dimensionless units in which the height of the initial droplet is unity (see Appendix), the SLE we thus consider is

$$\partial_t h \;=\; \partial_x \left\{ h^3\, \partial_x h \,+\, \sigma\, h^{3/2}\, \epsilon(x,t) \right\}. \tag{7.9}$$

We employ the same kind of algorithm that was used to simulate droplet spreading driven by surface tension and noise in [4], see the Appendix. Unless otherwise stated, we have considered $\sigma = 0\ (10^{-5/2})$ for the deterministic (stochastic) simulations.

Fig. 7.2(b) illustrates the evolution of an initial droplet as in Fig. 7.2(a), but as described by Eq. (7.9). Note that, since the smoothening effect of surface tension is not present, it would not be surprising to observe shock-like spreading of the drop front. Nevertheless, slopes in Fig. 7.2(b) are not as high as suggested by naked-eye inspection, note the difference in horizontal and vertical scales. On the other hand, given that the expected spreading laws due to gravity and fluctuations are relatively similar, and in order to appreciate the expected crossover, we have used a relatively large value of σ compared to

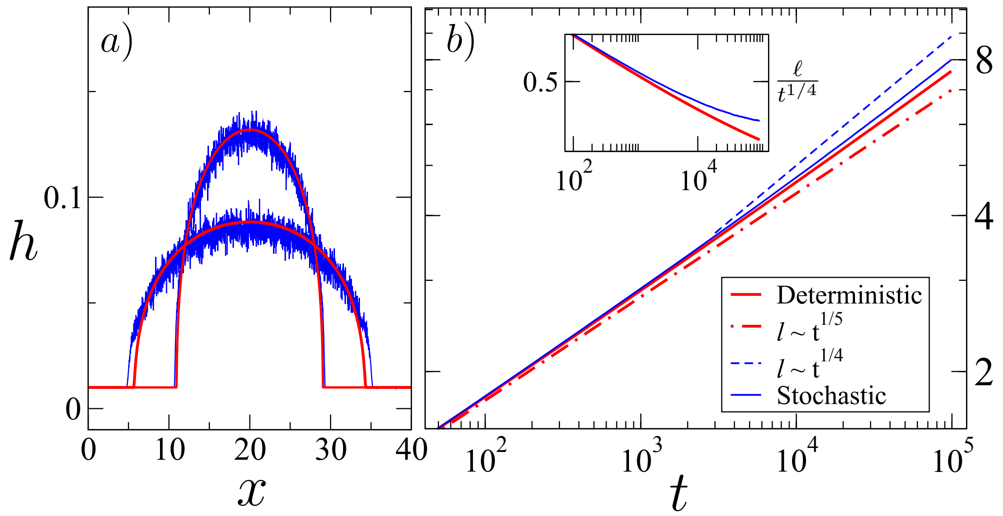

Figure 7.4: (a) Deterministic (thick red line) and stochastic (thin blue line; averaged over 15 stochastic realizations) droplets relaxing under gravity from the same initial condition, at times $t = 10^4$ and $8 \cdot 10^4$, top to bottom. (b) Droplet width vs time for the deterministic and stochastic simulations. The dot-dashed (dashed) line indicates the deterministic (stochastic) spreading law, as in the legend. The inset plots a rescaled droplet width in order to compare with the noise-dominated behavior.

the height of the precursor film, $h_* = 0.01$. Numerical results indeed indicate somewhat faster spreading for the stochastic droplets than for their deterministic counterparts, see Fig. 7.4(a). Here, we show the deterministic and the stochastic evolutions at two different times. Indeed, one can appreciate an enhancement of the droplet width in the latter case. In order to gain more quantitative understanding, we measure the average rate by which the characteristic width of the droplets, ℓ, evolves. To estimate it, we again follow [4] and consider the averaged second moment of the height profile, $\ell(t)$ defined in (7.2). As we can see in Fig. 7.1, the stochastic system departs from the deterministic behavior for $t \gtrsim 3000$, crossing over towards the purely noise-dominated regime. Notice that, due to the necessarily large value of the precursor thickness, which becomes comparable to the droplet height for long enough times, even the deterministic spreading yields the spreading exponent slightly larger than the $1/5$ expected value. In any case, there is a small but significant difference in droplet width between the deterministic and the stochastic cases, purely noise-dominated spreading being expected for sufficiently long times. As noted in Sec. 6.4, appropriate polymer-colloid mixtures exist [146, 147] which are characterized by very small (ultralow) values of the surface tension $\gamma \lesssim 1$ μN/m and capillary length ($\simeq 10$ μm). This implies thermal fluctuations with a strength which is comparable to the noise amplitude we have employed in our present simulations. Thus, they constitute potential experimental contexts in which gravity-driven spreading may be indeed enhanced by thermal noise.

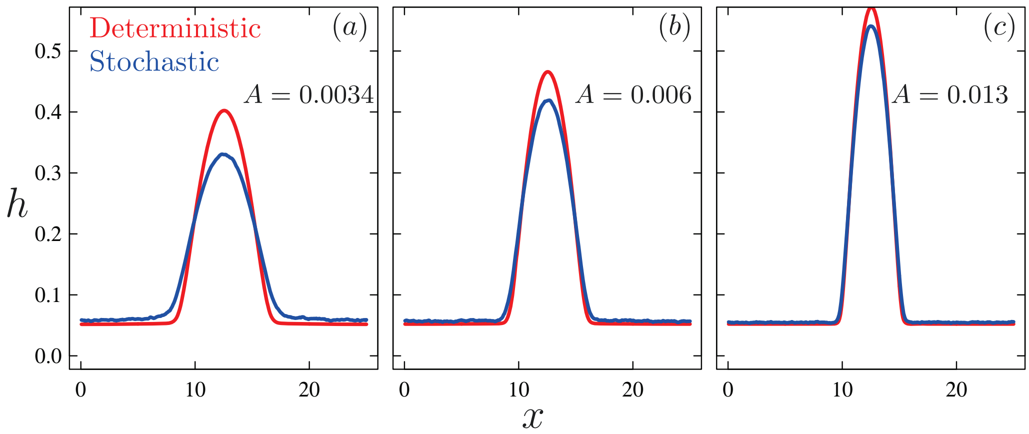

Figure 7.5: Deterministic and stochastic droplet spreading from numerical simulations of Eq. (7.11) at the stationary state. The stochastic shapes have been averaged over 100 noise realizations. Panels (a) through (c) correspond to increasing values of A, as given.

7.3 Influence of fluctuations on the contact angle

We now switch to a related situation encompassed by the SLE, Eq. (5.30), in which thermal fluctuations again can be seen to have non-negligible effects. Consider a spreading drop whose time evolution is governed by surface tension, and ignore gravity. Furthermore, consider the drop to be partially wetting, with a non-zero contact angle, θ. In this section we will discuss whether and how the presence of fluctuations influences the value of θ. One motivation for this discussion is that there are often substantial differences between the predictions of deterministic theory and experimentally measured contact angles, see e.g., [20] and the references therein. It is natural to consider whether these differences may be due to the neglect of thermal noise in the deterministic theory. In such case, a well-defined contact angle between the fluid droplet and the substrate arises as an interplay between surface tension and van der Waals forces [108, 120]. The specific form of the disjoining pressure depends on the material properties, and a variety of functional forms and parameters have been used. Here, we consider the commonly used power-law form [120] (described in Sec. 5.3),

$$\Pi(h) \approx 1/h^n - 1/h^m \qquad \text{with} \qquad (n, m) = (3, 2). \tag{7.10}$$

Hence, we consider the following SLE

$$\partial_t h = \partial_x \left\{ h^3\, \partial_x \left[-\partial_x^2 h + \frac{A}{h^2} - \frac{B}{h^3} \right] + \sigma\, h^{3/2}\, \epsilon(x,t) \right\}, \tag{7.11}$$

where A and B are material-dependent constants, and units have been rescaled so as to have an initial droplet of unit height, see Appendix. The choice $B = Ah_*$ leads to an equilibrium film (also called precursor film) of thickness h_*. The constant A is proportional to

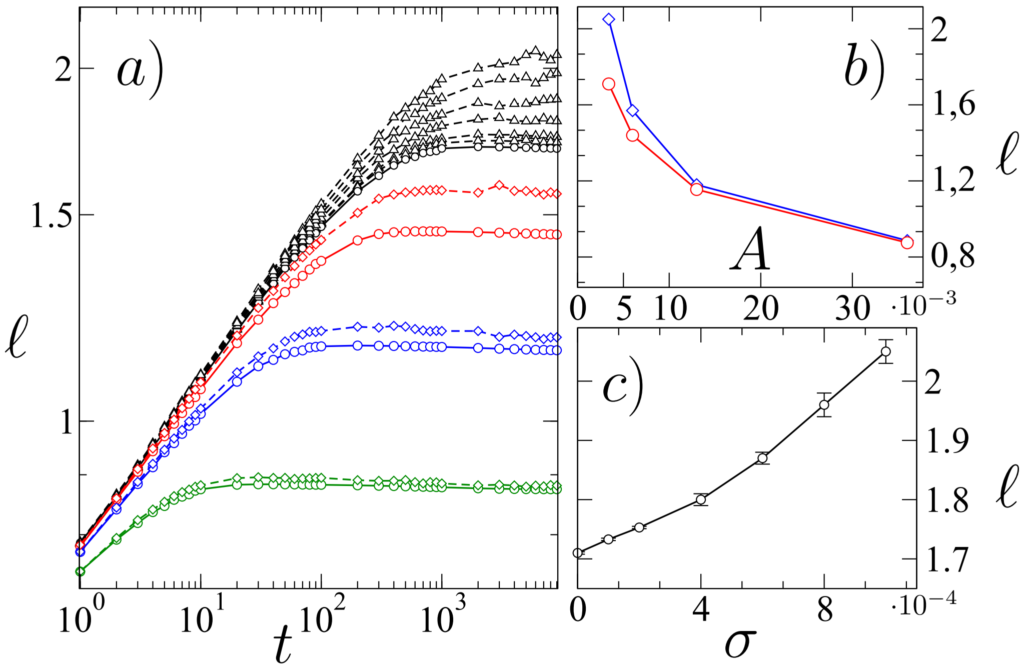

Figure 7.6: (a) Droplet width vs time for $A = 0.036, 0.013, 0.006$, and 0.0034, bottom to top. Deterministic values (circles, solid lines) remain systematically below the average stochastic values (diamonds and triangles, dashed lines). Stochastic simulations have been averaged over 100 noise realizations. The $A = 0.0034$ case (triangles, black dashed lines) was simulated for noise strengths $\sigma = 0.0001, 0.0002, 0.0004, 0.0006, 0.0008, 0.001$ (bottom to top), higher ℓ vales being obtained for higher σ. (b) Droplet width vs Hamaker constant for the deterministic (circles) and stochastic (diamonds) systems, for $\sigma = 0.001$. Statistical errors are smaller than the symbol sizes. (c) Droplet width vs noise strength σ for $A = 0.0034$. In all panels, lines are guides to the eye.

the Hamaker constant that characterizes vdW interactions [115] and is functionally related to the value of θ under the corresponding wetting conditions. The specific question we address here is how this relation is modified when fluctuations are taken into account.

To answer this question, we have simulated droplet spreading as described by the SLE, Eq. (7.11), and its deterministic limit, employing the same numerical algorithm as in the previous section (see previous Chapter, Sec. 6.4 for specific details and adjustments), the surface tension term being treated implicitly while the vdW interactions and fluctuations are treated explicitly. We use $h_* = 0.05$ and $\sigma = 0$ $(10^{-3/2})$ for the deterministic (stochastic) simulations, respectively. Special care has been taken in obtaining average shapes in the latter, taking into account that fluctuations can induce droplet motion. The idea is to calculate the droplet center of mass X as defined above, and then average droplets over noise realizations, provided all of them have been centered around this point.

Figure 7.5 shows the droplet shapes at times at which spreading has stopped and a time-independent value of the contact angle can be extracted. The results show that, on average, θ for a stochastic droplet [defined as in Fig. 7.5(b)] is smaller than the deterministic contact angle for the same system constants, γ and A. For instance, in Fig. 7.5(a) fluctuations decrease θ from 6° in the deterministic case to 4° in the stochastic system. Note that small-angle approximations to $A(\theta)$ [108] predict 15° for the deterministic case. Furthermore, Fig. 7.5 shows that the difference between the deterministic and the stochastic shapes increases for decreasing A, with the value of θ found for stochastic simulations being consistently smaller than in deterministic ones. Fluctuations also induce an increase in the effective value of the equilibrium film, h_*. As a consequence, there is a sizeable reduction in the droplet height due to volume conservation.

Figure 7.6 gives more detailed information about the influence of noise on droplet spreading. In panel (a), the deterministic and stochastic time evolutions of $\ell(t)$ are shown for different values of A. As in Fig. 7.5, larger stationary ℓ values are found for smaller values of the Hamaker constant, stochastic films being consistently wider than their deterministic counterparts, see also Fig. 7.6(b). The systematic increase of ℓ at steady-state with the noise amplitude σ is shown in Fig. 7.6(c).

7.4 Conclusions

In the present chapter we have considered the influence of thermal fluctuations on dynamics of spreading drops in two regimes: (i) gravity-dominated regime, where capillary effects have been ignored, and (ii) surface tension-dominated regime for spreading of partially wetting drop, where contact angle is introduced by disjoining pressure. In both cases we find that stochastic effects influence the dynamics, leading to faster spreading for the gravity-dominated regime, and decreasing the (deterministic) contact angle. For the former case, we corroborate the asymptotic large effect on the fluctuations found in [4] even for negligible surface tension, suggesting that spreading at large stages is always dominated by noise fluctuations. In the latter case the effect of contact angle decrease is particularly obvious for a decreasing value of Hamaker constant, suggesting a non-trivial effect whose relevance for realistic systems remains to be assessed.

Inclusion of stochastic contribution together with disjoining pressure term in the governing stochastic lubrication equation now allows for considering a number of open problems, including quantifying the influence of noise on film breakup, dewetting and pattern formation for fluid films of thickness on nanoscale, where basic ideas and some results will be presented in the following chapter. Computational investigation of these problems is studied in the following Chapter.

8

Fluctuations in Dewetting

In this chapter we present a study on the effect of fluctuations for stochastic thin films evolving under partial wetting conditions [120, 150, 151]. In many experiments thin flat films undergo a dewetting process which, up to a certain degree, is well described by linear theories. Recently, anomalies have been observed [20–22] with respect to pattern formation and drop shape and size, once the film has reached a partially wetting state.

Here, we study numerically the full non-linear SLE as fluctuations introduce changes in drop shape and distances between them, in a form that maybe consistent with experiments. Moreover, we also study the non-linear deterministic equation for different initial conditions and provide a full comparison between the linear and the non-linear stochastic and deterministic cases of lubrication equation.

We first demonstrate how linear analysis predicts the evolution using the spectral analysis. We also discuss the possible evolution depending on physical parameters in system. Then, we move to non-linear analysis and present our finding obtained from numerical simulations.

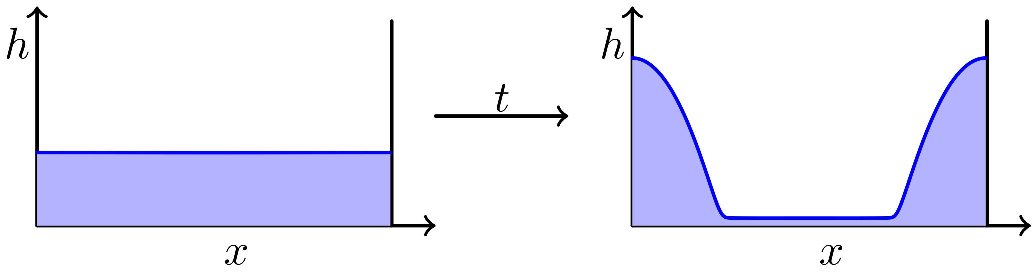

Figure 8.1: A small perturbation in the film surface, whose wavelength is unstable according to the linear theory, causes break up into drops.

8.1 Linear stability analysis

Thin liquid films and jets [151–153], both well described by the Navier-Stokes equations under the lubrication approximation, break into droplets under suitable conditions. There have been many attempts to describe the nature of breakup [107], the general conclusion being that the fluid breaks due to intrinsic properties. Actually, perturbations in the fluid surface cause the fluid to develop instabilities. Plateau [151] found that perturbations tend to reduce the surface area, so that the fluid changes its state. He also found a range of wavelengths that cause breakup. This mechanism is called spinodal or free-surface instability [108]. There is another mechanism, called nucleation-type instability [108] which is due to the presence of defects in the film or the substrate. In this chapter we will only study the first mechanism. The deterministic lubrication equation has a range of wavelengths that cause surface instabilities. This range can be found simply by linearizing the equation. Here we present the influence of thermal noise in such linear systems [18]. This was actually the initial point in our research, the evolution of the full (non-linear) SLE, neglecting gravity, which we again for simplicity present here,

$$\eta \partial_t h \ = \ \partial_x \left\{ \frac{h^3}{3}\, \partial_x \left[-\gamma \partial_x^2 h - \Pi(h) \right] + \sigma\, h^{3/2}\, \epsilon(x,t) \right\}. \tag{8.1}$$

We also recall here the considered disjoining pressure form (described in detail in Sec. 5.3) is

$$\Pi(h) = \kappa \left[\left(\frac{h_*}{h} \right)^n - \left(\frac{h_*}{h} \right)^m \right], \tag{8.2}$$

where κ is proportional to Hamaker constant, h_* is a microscopic precursor layer and h_0 averaged film height. The exponents remain the same as in the spreading study, $(n, m) = (3, 2)$.

Unlike the spreading scenario studied in Chap. 7, in which the initial film was taken far from equilibrium (the droplet kind of solution), namely with a contact angle much larger than the static contact angle, given by Eq. (5.37)), here we take a flat film with initial height h_0 (considerably higher than the precursor thickness) and we perturb it by a

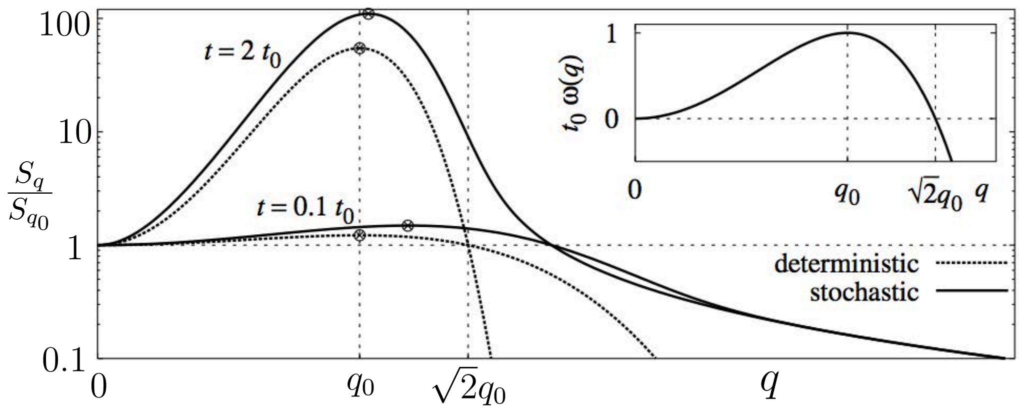

Figure 8.2: Structure factor (black lines) of the stochastic system (8.3) at two different times. For the stochastic case, the main peak moves to the left, eventually converging to q_0, while the deterministic system ($\sigma = 0$, black dotted lines) almost instantly selects the peak at q_0. Inset: Linear dispersion relation. Figure from *Fetzer et al* [18].

small sinusoidal function, so that the initial condition is $h = h_0 + \delta h$ where $\delta h \ll h_0$ see Fig. 8.1 left. If δh contains unstable wavelengths k, the instabilities will grow until the film breaks up into droplets, Fig. 8.1 right. To find the interval of unstable wave vectors k we insert the perturbed initial condition into the SLE and keep only linear terms in δh. Then, the SLE (8.1) becomes

$$\frac{\partial \delta h}{\partial t} + \gamma \nabla^4 \delta h - \Phi'' \nabla^2 \delta h + \sigma h_0^{3/2} \nabla \eta(x,t) = 0, \tag{8.3}$$

where $\Pi(h_0) = -\Phi'(h_0)$ (recall Sec. 5.3 and Fig. 5.3). The noise term becomes additive. In order to obtain unstable wavelengths we can write the perturbation as $\delta h = \epsilon h_0 e^{-ik+\omega t}$. Fourier transform the height and the noise term as

$$\delta h_q = \frac{1}{(2\pi)^2} \int \delta h \, e^{iqr} d^2q \qquad \eta(q,t) = \frac{1}{(2\pi)^2} \int \eta \, e^{iqr} d^2q \tag{8.4}$$

Using (8.3) we obtain

$$\frac{\partial \delta h_q}{\partial t} = \omega(q) h_q + \sigma h_0^{3/2} \nabla \eta(q,t), \tag{8.5}$$

where

$$\omega(q) = \frac{\gamma h_0^3}{3} q^2 \left(2q_0^2 - q^2\right), \qquad q_0 = -\frac{\Phi''(h_0)}{\gamma}. \tag{8.6}$$

Those wave-vector values q for which $\omega_q > 0$ correspond to instable perturbations, since their amplitudes grow exponentially with time. This happens for $q \in [0, \sqrt{2}q_0]$. There is a value of wave-vector, q_0, for which ω_q is maximized, see the inset in Fig. 8.2. To see how this comes about, we perform a structure factor analysis (see the definition of structure factor S_q in Sec. 1.3). For the linear equation S_q can be easily calculated analytically [145],

$$\begin{aligned} S_q &= \langle \delta h_q(t)\delta h_{-q}(t)\rangle = \\ &= (2\pi)^2\left[\tilde{S}_0(q)e^{2\omega(q)t} + \frac{\sigma^2 h_0^3}{3}\frac{q^2}{\omega(q)}\left(e^{2\omega(q)t} - 1\right)\right], \end{aligned} \tag{8.7}$$

where $\tilde{S}_0(q)$ is the initial power spectrum. We first analyze the deterministic case ($\sigma = 0$) for which Eq. (8.7) only has the first term. If our initial condition has a homogeneous structure factor $S_0(q) = c$, all wavelengths q larger than $\sqrt{2}q_0$ will disappear exponentially fast, as their linear dispersion function is negative, see the inset of Fig. 8.2. On the other hand, wavelengths in the interval $[0, q_0]$ grow in amplitude exponentially fast while the fastest growth rate being achieved at the wavelength q_0 for which ω reaches its positive maximum. This means that, as $S_{q_0,t=0}$ is flat, the maximum will be selected at the beginning of the evolution and will remain for all times, see Fig. 8.2.

Due to the white noise term stochastic linear systems develop the whole spectrum of wavelengths at the beginning of the evolution. Therefore we could simplify the analysis of stochastic systems by taking a flat film as the initial condition, which corresponds to a zero initial power spectrum ($\tilde{S}_0(q) = 0$). Hence, in Eq. (8.7) only the second term appears on the RHS. For early times $t \to 0$, and for wavelengths such that $\omega t \to 0$, the structure factor becomes

$$S_q \simeq \begin{cases} q^2 & \text{if} \quad \omega_q t \ll 1, \text{ and } q \ll q_0 \\ q^{-2} & \text{if} \quad \omega_q t \gg 1, \text{ and } q \gg q_0 \end{cases}. \tag{8.8}$$

This form is exactly the same as for the Kuramoto-Sivashinsky equation described in Sec. 1.5 with the same noise term as for the SLE. We saw that the maximum of the structure factor moves in time from infinity (no correlations) towards deterministic maximum which actually corresponds to the maximum of the dispersion relation. Moreover, the peak moves obeying a power-law, $q_m = q_0 + t^n$ with the exponent $n = -1/4$ (see the structure factor (8.7) for two different times in Fig. 8.2.

This analysis shows that for a flat structure factor initial condition (flat film with thickness h_0 perturbed by white noise fluctuations) the peak at q_0 is selected instantly in a deterministic linear system, while in a stochastic linear system the peak starts at q values larger than q_0 and moves in time towards q_0. Once it reaches q_0, it remains there. Moreover the S_q for wavelengths that give negative ω, decays exponentially in deterministic systems while in stochastic systems it decays quadratically due to the second term in the bracket on the RHS of Eq. (8.7). This is physically irrelevant as the structure factor at these wavelengths is orders of magnitude smaller comparing to the region around the peak. The stochastic peak, approaching the value q_0 for early times, describes a coarsening process and it was shown that the linear theory closely describes the evolution of polymer films which undergo coarsening in experimental setups [18], see Fig. 8.3.

The linear prediction is assumed to remain valid even in non-linear regimes of the evolution which is where the SLE defects from the Kuramoto-Shivasinsky [154]. This

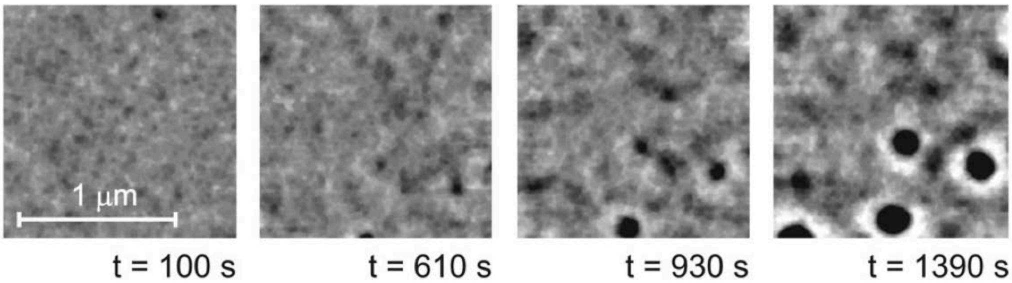

Figure 8.3: Experimental images, taken from Fetzer *et al.* [18], for different dewetting stages of a 3.9 nm polystyrene film, which show good agreement with the stochastic linear theory. The appearance of holes corresponds to the shift of the structure factor peak toward the analytically predicted value q_0, see Fig. 8.2.

assumption is not completely true as it was seen in experiments that once the film broke up and the droplets are formed, they communicate via precursor film or coalescence [155]. As a result, smaller droplets disappear in favor to larger droplets who adsorb their volume which is even energetically more favourable state [122]. This leads to decrease in characteristic wavelength (increase in characteristic distance between droplets) which is known as **coarsening process** (see Sec. 1.5). To this end, we are not only interested in non-linear regimes of droplet formation but also in the dynamics once the droplets are formed.

So far, we have analysed the cases for which the system develops instabilities, and how these instabilities evolve when fluctuations are accounted for. All this was done assuming that q_0 is positive, which is not always the case. Namely, if we implement the standard form of the vdW force [recall (5.32)] into q_0, from Eq. (8.6) we obtain

$$q_0^2 = \frac{A}{\gamma h_0}\left[m\left(\frac{h_*}{h_0}\right)^m - n\left(\frac{h_*}{h_0}\right)^n\right] \qquad (n, m) = (3, 2). \tag{8.9}$$

For this choice of potential, the system develops instabilities only if the precursor film is sufficiently small, namely, $h_* < 2h_0/3$. The condition $q_0^2 > 0$ defines the ratio h_*/h_0 for which the film is unstable for any initial thickness which is larger than $3h_*/2$. In presence of stabilazing forces such as gravity, another threshold value appears such that, for h_* smaller than such value, instabilities are also ruled out [108]. As we study nanometric and microscopic thin films for which gravity can be neglected, this latter possibility is not of our concern.

Different disjoining pressure exponent election would change the ratio between the contact angle and the characteristic wavelength in the system but it does not affect the evolution in general [20, 108]. Therefore our study is only focused on the stated choice.

8.2 Non-Linear stability analysis

In the previous chapter we have seen that, at short-times the SLE (8.1) predicts a morphological instability [59], i.e. surface tension, in competition with the destabilizing disjoining pressure, selects a typical length scale, λ, namely, the size of surface undulations. In a process reminiscent of domain coarsening in phase separation or spinodal decomposition of binary mixtures [66], and as seen in the experiments of [18], this scale increases nontrivially with time in a form which cannot be accounted for deterministically ($\sigma = 0$ in Eq. (8.1)). However, the study in [18] was limited to the linear regime, where perturbations of the flat film are small compared to its thickness and the morphology is dominated by capillary-like surface modes.

Open questions that have been arising from the linear analysis are if and how do the nonlinearities, responsible for actual droplet formation in Eq. (8.1), actually modify this time evolution. In particular, in view of the experimentally non-negligible thermal fluctuations: For instance, noise is known to modify the coarsening law of the 1D Cahn-Hilliard equation, one of the paradigmatic models in the context of spinodal decomposition [66, 156]. Here we extend the study of the effect of thermal fluctuations in the formation and evolution of droplets under partial wetting conditions. To this end, we study numerically the SLE (8.1) in the nonlinear regime. We find that thermal fluctuations unambiguously speed up the nonlinear process of droplet formation. Moreover, we show that, as compared to the deterministic case, noise also increases heterogeneity in droplet sizes and positions, while seemingly not affecting the coarsening process to a single droplet expected for asymptotic times [122, 155] which will be discussed in the following section.

We study Eq. (8.1) for the particular choice of the disjoining pressure exponents $(n, m) = (3, 2)$, that we also used in our droplet spreading study (Chap. 7). We have performed large-scale numerical simulations using a scheme [135] described in Chap. 6 that ensures non-negativeness of the solution for all times, if the initial film is positive in the full domain [137]. Specifically, our algorithm is based on the standard implicit (Crank-Nicholson) discretization [135], where surface tension is treated implicitly, while $\Pi(h)$ is treated explicitly; we employ zero-flux boundary conditions. The stochastic term in Eq. (8.1) is also dealt with explicitly, within the Stratonovich interpretation [17].

In our simulations we consider a nondimensional version of Eq. (8.1) obtained by defining $\hat{h} = h/h_c$, $\hat{x} = x/h_c$, and $\hat{t} = t/t_c$, where h_c is a typical film thickness and $t_c = 3\eta h_c/\gamma$ (for detailed derivation see Sec. 6.3). This leads to non-dimensional amplitudes $\hat{\sigma} = (k_B T/\gamma h_c^2)^{1/2}$ and to $\hat{\kappa} = \kappa h_c/\gamma$; we use the exponents $(n, m) = (3, 2)$ as in e.g. [108]. We perform the deterministic and stochastic simulations of Eq. (8.1) using a precursor thickness $\hat{h}_* = 0.01$ and the same random *initial condition*, namely, random values of the thickness with non-dimensional average $\hat{h}_0 = 0.1$ and variance $10^{-2}\hat{h}_0$. The contact angle is set to $50°$ in the expression $\hat{\kappa} = 2(1 - \cos\theta)/\hat{h}_*$ [108], leading to $\hat{\kappa} = 72$; within the long wave theory implementation, the actual contact angle (measured by the

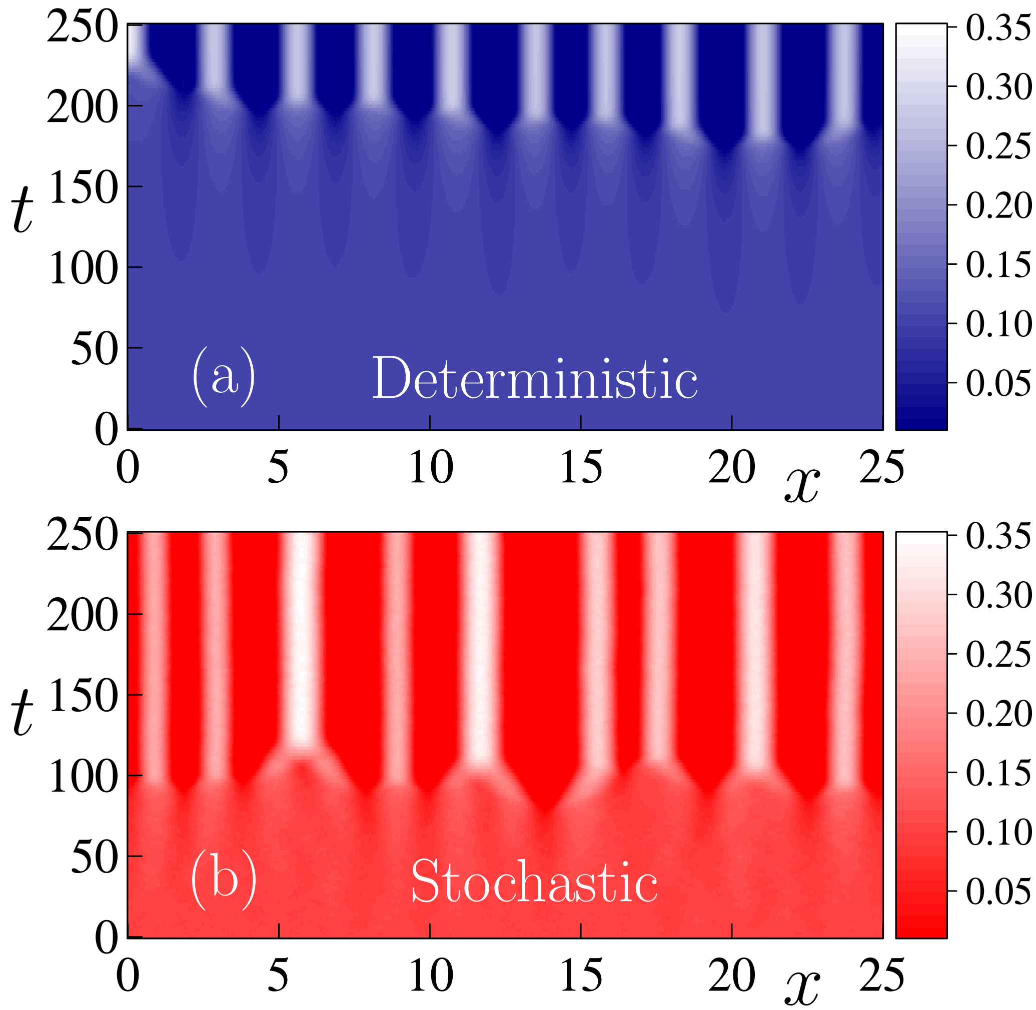

Figure 8.4: Space-time plot of droplet formation and evolution as predicted by Eq. ((8.1)) for $\sigma = 0$ (a) and $\sigma = 10^{-2}$ (b), for the same parameter values and initial conditions, see main text. Brighter (darker) color corresponds to larger (smaller) values of the film thickness $h(x, t)$.

slope of the tangent line passed through the drop profile through the point of inflection) is smaller and is close to $25°$. The spatial step size $dx = \hat{h}_*$; this choice is known to lead to accurate results [139]. The temporal step size is adaptive, following the approach described in [135]. This allows to obtain converged results with reasonable computational effort; the use of such adaptive time stepping is particularly important for the purpose of carrying out simulations for long times where coarsening effects become relevant. We use a large domain size $L \approx 31\lambda$, where λ is the most unstable wavelength obtained by linear stability analysis of deterministic version of Eq. (8.1)), discussed further below. Combined with a large number of realizations, $\simeq 200$, such a domain allows to obtain

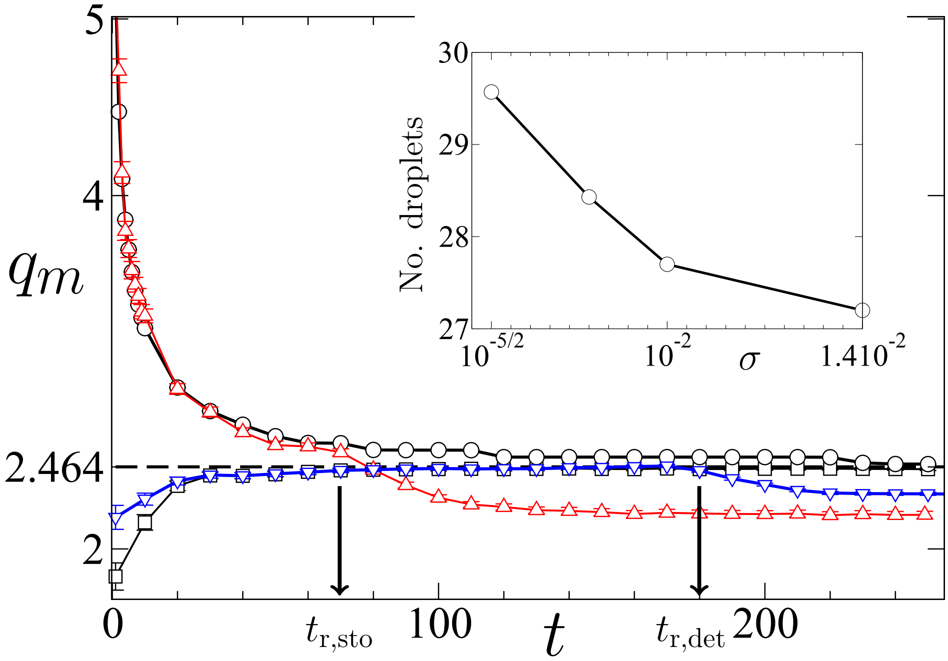

Figure 8.5: Time evolution of the position of the main maximum, $q_{\rm m}$, of the structure factor. The dashed black line indicates the deterministic linear prediction, q_0. Black circles (squares) correspond to predictions from Eq. ((8.7)) for $\sigma = 10^{-2}$ ($\sigma = 0$). Red up [blue down] triangles provide the position of $q_{\rm m,sto}(t)$ [$q_{\rm m,det}(t)$] as obtained in numerical simulations of Eq. (8.1) for $\sigma = 10^{-2}$ ($\sigma = 0$). Rupture times are signalled by arrows. All results are obtained by averaging over 200 noise realizations. Inset: Number of droplets for different noise amplitudes at $t = 220$. All lines are guides to the eye.

statistically meaningful results. The specified parameter values are closely related to the polymer films studied in [18], where the characteristic film thickness is 4 nm ($h_c = 40$ nm, so that $\hat{h}_0 = 0.1$), while $\gamma = 0.03$ N/m and the Hamaker constant $A = 2 \cdot 10^{-20}$ J yield a contact angle in the $15 - 20°$ range. For these parameter values the non-dimensional noise strength $\hat{\sigma} \simeq 10^{-2}$ corresponds to $T = 50 - 60°$ C. On the other hand, for the liquid metal thin films considered in [20], $\gamma = 1.3$ N/m, $T = 2000$ K, and $h_c \in [50, 150]$ nm, leading to $\hat{\sigma} \in [10^{-5/2}, 10^{-3}]$.

From now on, and unless otherwise stated, we work in dimensionless units and remove hats for notational simplicity. Figure 8.4 shows examples of the time evolution predicted by Eq. (8.1) in the deterministic and stochastic cases. Fig. 8.4 shows examples of the time evolution predicted by Eq. (8.1) in the deterministic and stochastic cases. Well-defined droplets (clear bands) emerge after a *rupture time* of roughly $t_{\rm r,det} = 180$ ($t_{\rm r,sto} = 80$) time units in the deterministic (stochastic) system. In the latter case there is a substantial amount of droplet merging around that time, after which activity decreases. Comparing both panels, we immediately observe that the width of the droplets (clear bands) and their locations are much more regular in the deterministic than in the stochastic case.

Although some spatial modulation exists in Fig. 8.4 at earlier times, the system behavior is less visually clear. However, at such time scales one can resort to linear stability analysis [17, 18, 108] described in the previous section. The time evolution of the system is conveniently described by the structure factor S_q, which within linear approximation [17, 18], is given by Eq. (8.7) which non-dimensional form is

$$S_q = (2\pi)^2 \left[S_0(q) e^{2\omega(q)t} + \frac{\sigma^2 h_0^3}{2} \frac{q^2}{\omega(q)} \left(e^{2\omega(q)t} - 1 \right) \right]. \tag{8.10}$$

Here, $h_q(t)$ is the Fourier cosine transform [31] of $h(x,t)$ for wavenumber q, $S_0(q)$ is the initial structure factor, h_0 is a film thickness, and the growth rate is given by the dispersion relation $\omega(q) = h_0^3 q^2 \left(2q_0^2 - q^2\right)/3$. Here $q_0^2 = -\Pi'(h_0)/2$. The wavelengths of unstable perturbations correspond to $q \in [0, \sqrt{2}q_0]$, for which $\omega(q) \geq 0$. Starting from an initial condition with mean h_0, the deterministic system very quickly selects the wavenumber $q_{\mathrm{m,det}} = q_0$ for which the growth rate $\omega(q)$ reaches its positive maximum, see black squares and blue triangles in Fig. 8.5, where we plot the time evolution of the value of wavenumber q_{m} at which the main maximum of S_q occurs. For our parameter choice, $q_0 = 2.464$. Within linear approximation, this sets the length scale of the pattern, $\lambda = 2\pi/q_0 = 2.546$, namely, the average size of surface undulations. In contrast, stochastic systems initially develop nontrivial short lengthscale (large q) correlations, so that $S_q(t)$ displays a maximum for a wavenumber value $q_{\mathrm{m,sto}}$ which decreases with time towards the deterministic value q_0, see Fig. 8.5 and [158]. The structure factor increases for the wavelengths of unstable perturbations, which belong to $q \in [0, \sqrt{2}q_0]$, for which $\omega(q) \geq 0$ (see Eqs. (8.6) and (8.9)). Starting from an initial condition with mean h_0, the deterministic system instantly selects the wave-vector $q_{\mathrm{m}} = q_0$ for which the growth rate $\omega(q)$ reaches its positive maximum. For our parameter choice, we obtain $q_0 = 2.464$. Within linear approximation, this sets the length scale of the pattern, $\lambda = 2\pi/q_{\mathrm{m}} = 2.546$, namely, the average size of surface undulations. In contrast, stochastic systems initially develop nontrivial short length-scale (large q) correlations, so that $S_q(t)$ displays a maximum for a wave vector value q_m which decreases with time towards the deterministic value q_0, see Fig. 8.5 and [158]. This is the process described in [18] as coarsening. Note that, as mentioned above, droplets have not yet formed; as seen in [158], for these times the film morphology remains largely a small-amplitude sinusoid. In addition, for stochastic simulations, $q_{\mathrm{m,sto}} > q_0$; as we will see, this inequality does not hold in the nonlinear regime.

Within the range of validity of the linear approximation, the film develops unstable modes that remain independent of one another. If the linear predictions were applicable to long times, then the number of drops eventually formed would be essentially fixed by the linear value $\lambda = 2.546$, since S_q is characterized by a well defined peak around $q = q_{\mathrm{m}}$, see black lines in Fig. 8.6.

However, experiments [20] show that the distribution of droplet sizes is relatively

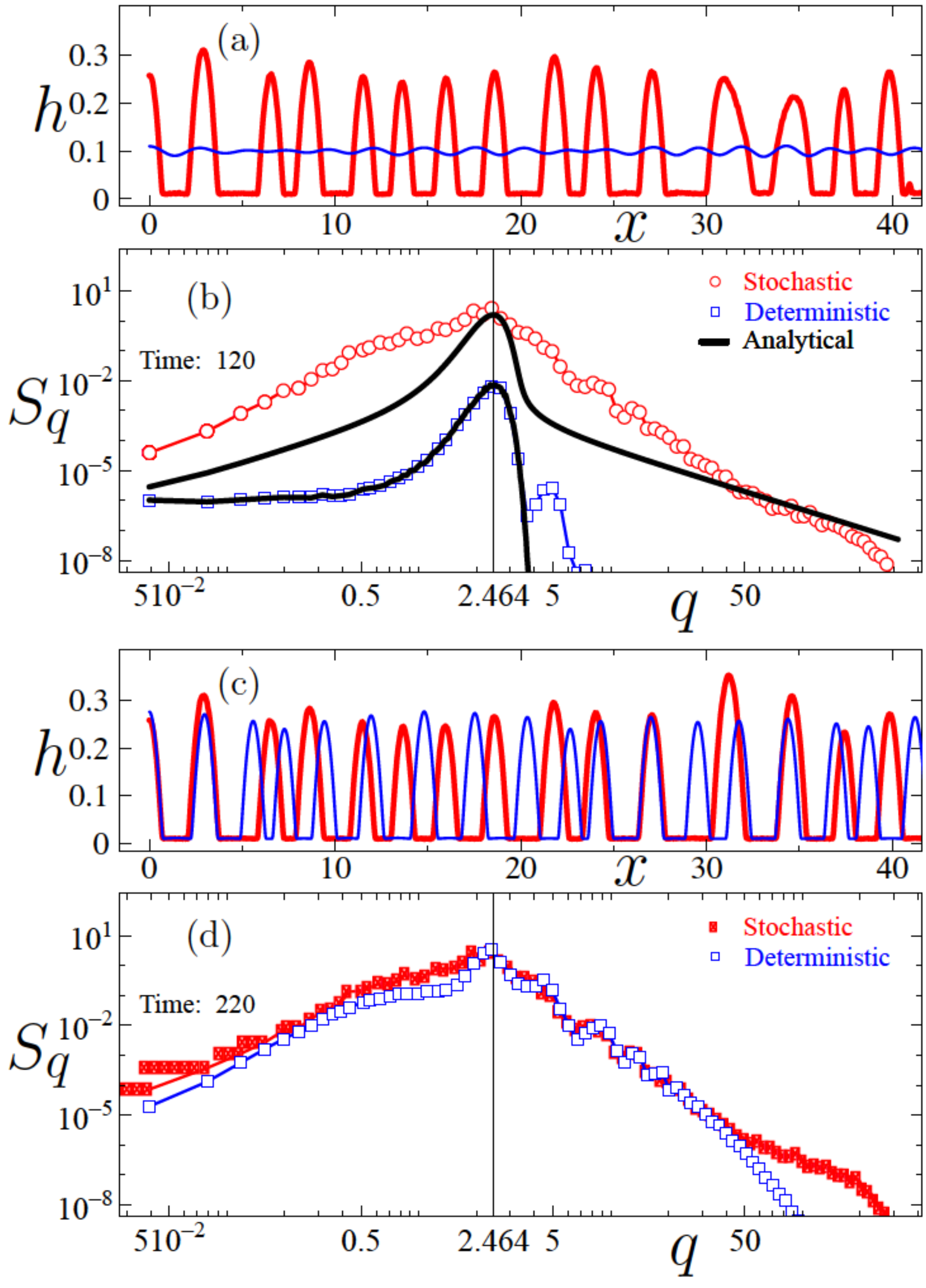

Figure 8.6: (a), (c): Surface morphologies from simulations of Eq. (8.1) for $\sigma = 0$ (blue line) and $\sigma = 10^{-2}$ (single realization, thick red line) at $t = 120$ (a) and 220 (c). (b), (d): Structure factor averaged over 200 noise realizations, at $t = 120$ (b) and 220 (d) for $\sigma = 0$ (blue squares) and $\sigma = 10^{-2}$ (red circles). The thick black lines in (b) provide the corresponding analytical predictions from Eq. (8.7). Thin lines are guides to the eye.

wide. Droplet forms differ strongly from smooth sinusoids, and they interact non-trivially (e.g. through merging and coalescing) during their evolution. On long time scales, the number of drops needs to reduce, as a single larger drop is energetically more favorable than two smaller ones [122,155]. Actually, the most stable configuration of the system is a single droplet, since the evolution described by Eq. (8.1) drives the system to the minimum of the interface Hamiltonian

$$\mathcal{H}[h] = \int \mathrm{d}x \, \left[\Phi(h) + \gamma(\partial_x h)^2/2\right] . \tag{8.11}$$

Hence, we next need to address droplet formation for times $t \gtrsim 60$, see Fig. 2, away from the linear regime. As seen in the animation provided at [158], nonlinear effects indeed set in for $t \simeq 60$. Thus, the deterministic structure factor develops higher harmonics, while the stochastic S_q also departs clearly from the linear solution, Eq. (8.7), see Fig. 8.6 for two sample times. The higher harmonics are at least one order of magnitude smaller than the main peak [158], so that they barely influence later stages of the evolution. In addition, the rupture time at which well-defined droplets form is much shorter for the stochastic ($t_{\mathrm{r,sto}} \simeq 80$) than in the deterministic ($t_{\mathrm{r,det}} \simeq 180$) case, see [158] and also Fig. 8.6(a) for $t = 120$, where droplets have appeared in the former case, but not yet in the latter.

After rupture, the S_q distribution broadens around the main peak both in the stochastic and in the deterministic systems, and for values of q on both sides of q_{m}, see Fig. 8.6(b,d) and [158]. Moreover, there is an additional boost in the rupture process so that stochastic droplets create faster than one would expect using the linear theory: Note that rupture times are signaled by a kink in the corresponding $q_{\mathrm{m}}(t)$ data. At rupture, nonlinear ripening of droplets takes place, namely, a decrease of q_{m} with time, which is more pronounced and occurs earlier in the stochastic system. In contrast to linear predictions, the deterministic system also undergoes a similar, albeit delayed process. We conjecture that disorder in droplet positions favors merging of nearby drops, inducing more rapid decrease of q_{m} in the stochastic system.

Also, for any $\sigma \geq 0$, once the drops are well formed the decrease in $q_{\mathrm{m}}(t)$ with time slows down. On average, the value of q_{m} which is eventually achieved (say, for $t \gtrsim 220$) is smaller for $\sigma \neq 0$. This behavior implies a smaller number of drops for a fixed domain in the stochastic system, see e.g. Fig. 8.6(c). Also recall Fig. 8.4, where substantial drop merging is seen for this case during times from rupture up to $t \simeq 120$. We note that, for the time scales considered so far, the final number of droplets decreases when the noise intensity (say, temperature) increases, see the inset of Fig. 8.5.

Figure 8.7, showing the distribution of drop heights and their distances, illustrates a further significant difference between stochastic and deterministic evolution: stochasticity indeed leads to much wider droplet distributions, and therefore to much more irregular patterns. Two sample morphologies are compared in Fig. 8.6(c). Also, the inset in Fig. 8.7(b) shows that the width at half maximum of the S_q distribution, Δ, is an increasing function

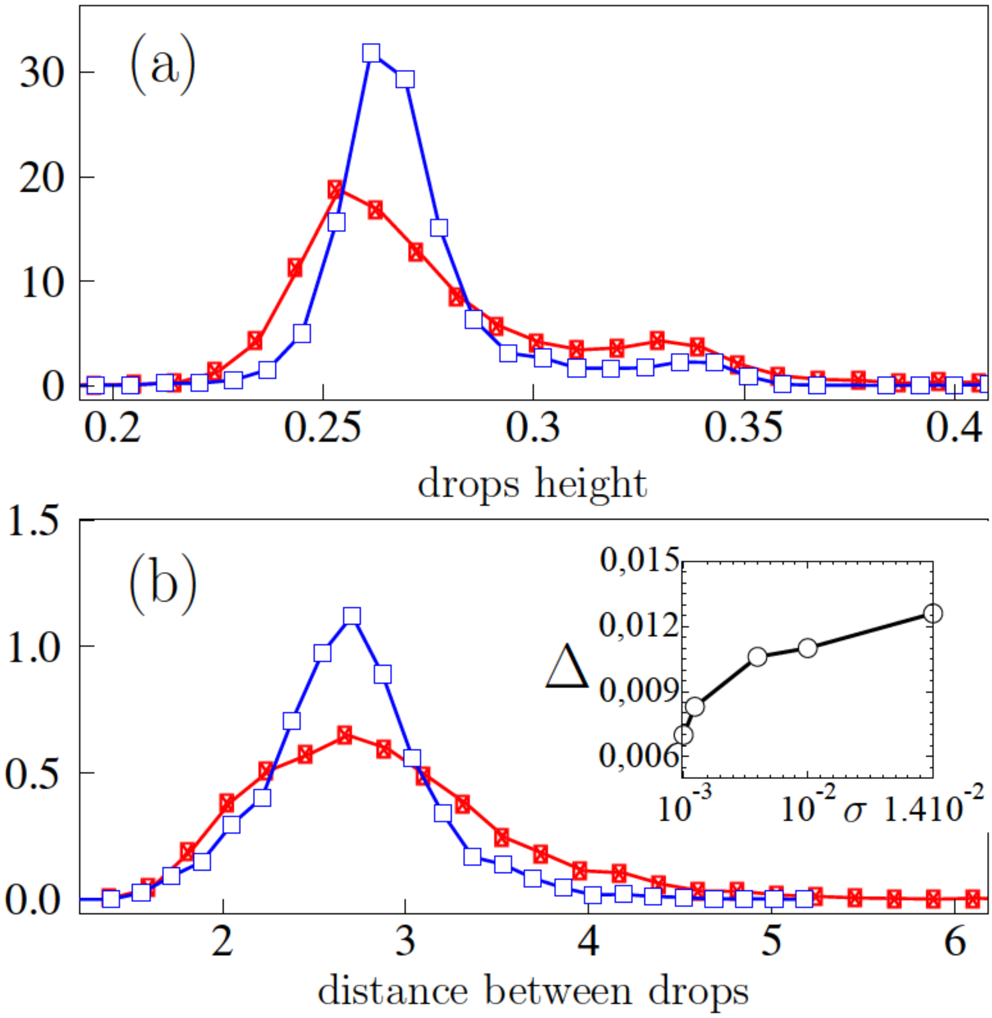

Figure 8.7: Distribution functions of drop heights (a) and inter-drop distances (b) at time $t = 220$ for $\sigma = 0$ (blue squares) and $\sigma = 10^{-2}$ (red circles). Inset: width of the main peak of S_q at $t = 220$, as a function of noise amplitude. All lines are guides to the eye.

of noise amplitude, as expected. This finding may be of significant importance in applications, where regularity of the distribution of drops is often desired. Our results suggest that decreasing noise amplitude may be the key to achieve this goal.

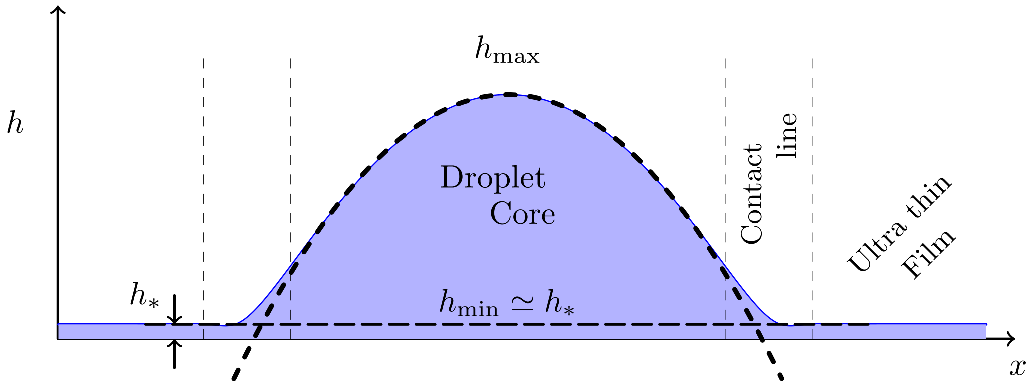

Figure 8.8: Example of a droplet profile in equilibrium, obtained from a numerical simulation of the SLE, where the thick black dashed curve is the parabolic approximation in good agreement with the droplet profile in the "Droplet Core" region. The actual value of the surface height in the region "ultra thin film" is slightly larger than the equilibrium precursor height h_*.

8.3 Coarsening

Once the drops are formed in a dewetting process described by the SLE, the system remains in a near-equilibrium state only on relatively short time scales. For later stages of the evolution the droplets exchange mass through the precursor film and the smaller ones disappear in favor of their more massive neighbors [122, 155]. Glasner and Witelski [122] showed that larger droplets are energetically more favorable so that the mass flux through the precursor film leads to disappearance of smaller droplets yielding a coarsening process. The basic steps of the argument for the SLE (8.1) are given here.

A steady-state solution of the deterministic Eq. (8.1) (for simplicity we consider $\gamma = 1$), see Fig. 8.8, implies a constant pressure everywhere on the droplet surface,

$$p = -\gamma \partial_x^2 h - \Pi(h) = \text{const.} \tag{8.12}$$

A sharp eye can spot in Fig. 8.8 a poor difference between the minimum height of the droplet h_{min} and the precursor thickness h_*. This difference implies that the disjoining pressure reaches a minimum at h_{min}, defining the constant pressure $p = \Pi(h_{\text{min}}) > 0$, since at the precursor $\partial_x^2 h \simeq 0$. For easier analysis, we consider the integral over the height so that Eq. (8.12) becomes

$$\frac{1}{2}\left(\frac{dh}{dx}\right)^2 = \Phi(h) - \Phi(h_{\text{min}}) - p(h - h_{\text{min}}), \tag{8.13}$$

where $\Pi(h) = -\Phi'(h)$. At the top of the droplet, $h_{\max}$, we have

$$\frac{dh}{dx} = 0 \qquad \Longrightarrow \qquad h_{\max} \simeq \Phi(h_*)/p, \tag{8.14}$$

where we have approximated Eq. (8.13) as $\Phi(h_{\text{min}}) \simeq \Phi(h_*)$, and $h_{\text{max}} \gg h_{\text{min}}$ and $\Phi(h_{\text{max}}) \simeq 0$. Actually, in the "droplet core" region in Fig. 8.8 as $h \gg h_*$ we can neglect the potential energy and Eq. (8.13) becomes a simple second order differential equation whose solution has a parabolic form

$$h(x) = \frac{1}{2}p(w^2 - x^2), \quad \text{where} \quad h_{\text{max}} = \frac{1}{2}pw^2. \tag{8.15}$$

The droplet width w expressed using Eq. (8.14) becomes

$$w^2 = \frac{\kappa}{2p^2}. \tag{8.16}$$

Finally, assuming that the total volume of the droplet is approximately in the droplet core region, we have

$$V = \int_{-w}^{w} h(x;p)dx \simeq \frac{\kappa^{3/2}}{3\sqrt{2}p^2}. \tag{8.17}$$

A droplet of volume $2V$ corresponds to a modified pressure $p \to p/\sqrt{2}$ and width $w \to \sqrt{2}w$. The total energy of a droplet is the sum of the surface tension and the vdW interaction,

$$E(h) = \int \Phi + \frac{1}{2}h_x^2 dx, \tag{8.18}$$

where Φ can be neglected in the droplet core. Hence, using (8.15) and (8.16) the total energy of two droplets is

$$E(\text{two droplets of volume } V) = 2\int_{-w}^{w} \frac{1}{2}p^2x^2dx = \frac{\sqrt{2}\kappa^{3/2}}{6p}, \tag{8.19}$$

while the energy of a single larger droplet of $2V$ is

$$E(\text{one droplet of volume } 2V) = \int_{-\sqrt{2}w}^{\sqrt{2}w} \frac{1}{2}\frac{p^2}{2}x^2dx = \frac{\kappa^{3/2}}{6p}. \tag{8.20}$$

One larger droplet occupies less space than two smaller ones, which leads to an even larger difference than this analysis of surface tension energies predicts. Hence, the most energetically favorable state is a single droplet morphology.

At later stages of the film evolution, when droplets are well separated, the relative movement of a droplet is small comparing to the distance between droplets and practically there is no coalescence [122], which can be seen from our long time simulations [159]. Therefore, instead of the height evolution the process can be better described by the evolution of the flux, $J = -h^3\partial_x p(h)$ through the precursor film, where the mayor contribution comes from the vdW interactions. In this way, Glasner and Witelski [122] developed a simplified model that is capable of simulating the evolution of very large-domain films. The simulations of the model show that for well-separated droplets in the deterministic system, $\hat{\sigma} = 0$, the number of droplets decreases as $N(t) \sim t^{-2/5}$, which is analytically supported by a self-similar solutions analysis [122].

In our case, we have considered much larger time scales, to probe the convergence of the stochastic system to the equilibrium single-droplet solution. Up to the times discussed in the previous section, the decrease of $q_m(t)$ seems mostly induced by droplet coalescence. This introduces relatively large distances among remaining units, recall Fig. 8.4 for long times. We have considered the evolution predicted by Eq. (8.1) for $\hat{\sigma} \neq 0$ at very long times up to $t = 10^4$ for a domain which fits 30 droplets, taking the characteristic distance between from the linear analysis prediction. Computational feasibility requires a larger precursor thickness $\hat{h}_* = 0.04$. Our results, see Fig. 8.9, indicate that fluctuations do shorten significantly the time scales on which coarsening occurs. However, they become less relevant with increasing time, to the extent that the coarsening law for $N(t)$ is not modified, at least within the accuracy of the results, see [159]. From this point of view, droplet coarsening would belong into the class of phenomena for which noise does not change the coarsening universality class [66] of the corresponding deterministic system.

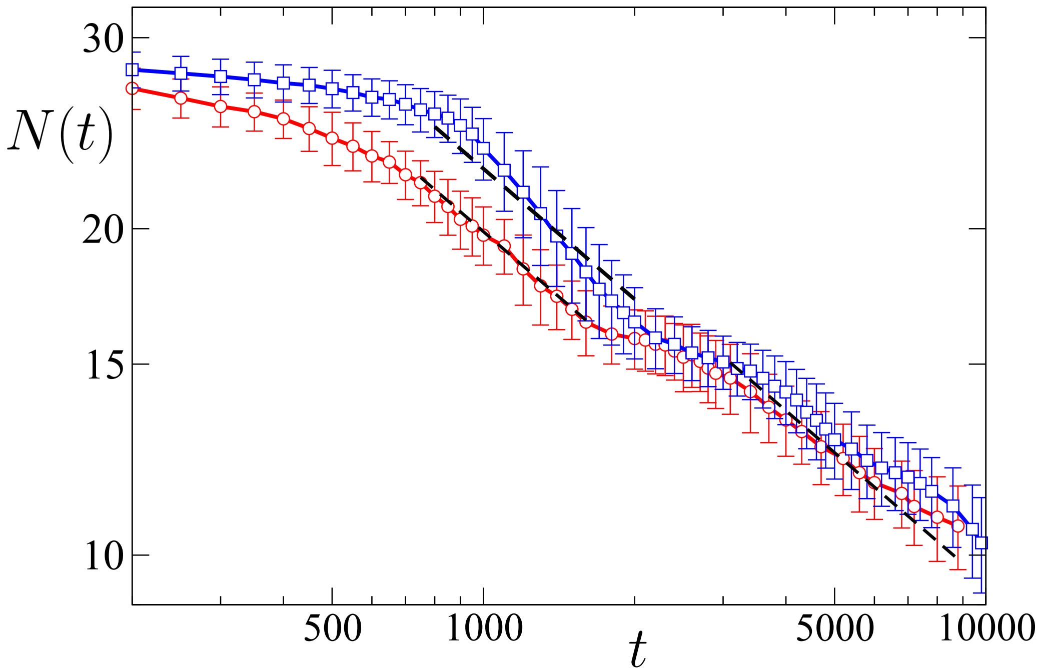

Figure 8.9: Log-log plot showing the time evolution of the number of droplets vs time, for long times up to $t = 10000$. Blue squares (red circles) correspond to deterministic ($\hat{\sigma} = 0$) and stochastic ($\hat{\sigma} = 10^{5/2}$) simulations, respectively. For reference, the dashed lines correspond to the power-law decay $N(t) \sim t^{-2/5}$ found for very large deterministic systems in [122]. Solid blue and red lines are guides to the eye.

8.4 Conclusions

In summary, we have shown that stochastic effects due to thermal noise may play a significant role in dewetting of thin fluid films, in each of the three stages of evolution considered. For very early times, stochasticity leads to a decrease of the most unstable wavenumber, $q_{\mathrm{m,sto}}$, down from the values that are large compared to the deterministic one, q_0; however, within this stage $q_{\mathrm{m,sto}}$ remains larger than q_0. After this, noise triggers an earlier onset of nonlinear effects, inducing a shorter rupture time. At these time scales, stochasticity leads to droplet coarsening, in the sense that $q_{\mathrm{m,sto}} < q_0$, in contrast to the linear regime. Finally, for much longer times, fluctuations speed up the coarsening process that will ultimately lead to formation of the single-drop, energetically favored state. Qualitatively, the deterministic coarsening law for the number of drops remains unchanged. However, *quantitatively* the time scales involved in this long-time coarsening process are significantly influenced by noise, and we conjecture that stochastic effects may be observable in careful experiments carried out with fluid films of nanoscale thickness.

Conclusions and Outlook

In this thesis we have studied the effect of fluctuations in two important paradigms of soft condensed matter physics, namely, Fisher fronts and thin fluid films. Our study of stochastic FKPP traveling waves broadens current knowledge on the influence of thermal noise onto the dynamics of these waves in two space dimensions. The FKPP equation describes the evolution of a stable state into an unstable one by creating a surface (a line in one dimension) that delimits the occupancy of the stable state. This $2d$ surface contains equipotential lines (points, in $1d$) perpendicular to the velocity direction. Due to the *pulled* nature of the FKPP front, the noise decreases the velocity in such way that, on average, the decrease depends logarithmically on the total number of particles. Hence, even for a macroscopic number of particles, the effect of fluctuations can be observed. In two space dimensions, the stochastic front surface roughens in time with the scale-invariance properties. Indeed, we have shown through extensive simulations of the algorithm based on a special stochastic PDE solver, that the $2d$ sFKPP traveling wave solutions define a surface that roughens with the same scaling exponents as the KPZ equation in $1d$. To further support this claim, we have calculated the distribution function of the fluctuations in surface position, and obtained very good agreement with the distribution of the KPZ surface, which is the Tracy-Widom-GOE distribution. The fact that dimensionality of the universality class is smaller than the one of the sFKPP equation lies in the weak-noise mechanism, which only affects the microscopic region of the front. In the macroscopic region, the weak noise does not produce any additional effect. Namely, above certain length-scale, the effect that fluctuations produce in the microscopic region, simply propagates back to the macroscopic one. We show that the morphology of the microscopic surface defines that of the macroscopic surface after a time related to the total number of particles, providing the same universality class for all equipotential lines.

With respect to thin fluid films, our study of the spreading of droplets, described by the lubrication equation, confirmed the enhancement of spreading in the surface-tension-dominated regime, when thermal fluctuations are accounted for. To check the validity of analytical argument, based on self-similar solutions, that supports the faster spreading rate of stochastic systems, we have studied the gravity-dominated regime. Actually, deterministic droplets already spread faster under gravity than under surface-tension while due to the self-similar solution shape, it is difficult to reach times where noise unambiguously dominates the spreading. Nevertheless, we show that in this case there is also an enhanced spreading with respect to the one described by the deterministic equation, in such a way that, as in the surface-tension-dominated case, at long times the system tends to reach the spreading law based on the self-similar analysis of the noise term. We have also studied the spreading under the influence of surface tension and the van der Waals force. The interplay between these two forces introduces a fixed contact angle given by the Young-Laplace formula, adapted to the lubrication approximation. We show that, on average, fluctuations extend more the droplet defining a slightly smaller contact angle. The difference in contact angle increases with the increase of the amplitude of the noise. It also increases for smaller contact angles (given by the Young-Laplace formula). For instance, in physical systems, like specific polymer films, deterministic contact angles of $\sim 20^\circ$ correspond to the roughly $\sim 13^\circ$ stochastic contact angles at physically relevant temperatures.

Finally, we have conducted a comparison of the full time evolution between stochastic and deterministic dewetting processes described by the lubrication equation. A flat film initial condition, if perturbed by unstable modes, breaks into droplets. Thus, linear analysis had provided good results, predicting the evolution of unstable modes. Here we have first discussed the evolution on time scales on which droplets develop completely. With the increased interest in experiments on dewetting, many setups have led to irregular pattern formation, often inconsistent with linear theory. The latter predicts that, the unstable modes do not couple but grow independently, so that the fastest growing mode selects the characteristic length scale in the film, namely, the distance between the droplets. Our deterministic simulations show that the unstable modes do couple in the nonlinear time regime. The main peak of the power spectrum moves towards smaller values with respect to the value predicted by the linear analysis, leading to a larger characteristic length. Still, the distribution of the distances between droplets (also of the droplet heights) remains narrow. To be able to give good comparison between deterministic and stochastic systems, the same initial conditions are used. With respect to stochastic films, they are seen to undergo a coarsening process in the linear regime where the structure factor peak moves from larger wavelengths toward the deterministic linear peak obeying a power-law decay. At the rupture time, nonlinear terms become significant and the peak starts moving more rapidly. Eventually, the peak goes beyond the values of both the linear and nonlinear deterministic systems. We also show that, for larger noise amplitudes (temperatures) the peak reaches smaller wavelengths, i.e. the characteristic length-scale (droplet distance) grows with the increase of fluctuations. During their development, the droplets move laterally more than the deterministic ones. They often approach close enough to each other to cause coalescence, which leads to larger droplet distances. Moreover, the droplet size varies significantly in stochastic systems, comparing to their deterministic counterparts. In general, fluctuations increase the irregularity of the pattern and the system develops a variety of droplet sizes.

Due to the precursor film, droplets exchange mass, so that smaller droplets disappear in favor of their larger neighbours. Hence, the SLE undergoes a coarsening process towards a single large droplet. The smaller the precursor is, the larger the time-scale to reach that state becomes. We have simulated thick precursor films for large domains. Stochastic films lose droplets more rapidly just after their creation, but eventually the deterministic system the same number after which the evolution is almost indistinguishable from the deterministic case. Still we cannot claim that any of the systems shows the expected power-law for the decrease in number of droplets. This remains jet to be studied in more detail.

Future Work

Bearing in mind the complexity and variety of possible setups for the systems we have studied, a number of related projects naturally arise in connection with our results, that remain to be studied in future.

Regarding FKPP fronts, a natural generalization of our work could be to consider a circular geometry for the advancing front, beyond the band geometry which we have studied. The goal would be to assess the occurrence of front fluctuations described by the TW-GUE distribution, as expected within recent developments related with KPZ universality. Such type of geometry arises naturally in many physical context, like e.g. the growth of bacterial colonies.

Beyond the specific sFKPP equation we have studied, a more general process $A + B \to 2A$ is described by the coupled reaction-diffusion equations,

$$\begin{aligned} \frac{\partial c_A}{\partial t} &= D_A \nabla^2 c_A + c_A c_B \\ \frac{\partial c_B}{\partial t} &= D_B \nabla^2 c_B - c_A c_B, \end{aligned} \tag{8.21}$$

where c_A and c_B are the concentrations of the A and B species. The special case $D_A = D_B$ leads to the FKPP equation. If the cut-off theory is applied (concentrations are set to zero whenever they are smaller than some small number ϵ related to the total number of particles), and for $D = D_B/D_A > 1$, this system develops morphologically unstable solutions [70] when ϵ is not too small. This result has been confirmed by simulating the system (8.21) using a PDE solver and eliminating values below ϵ. In view of our results for the sFKPP equation, it would be interesting to study the evolution of system (8.21) when fluctuations are accounted for.

Recently, a number of interesting papers have appeared that deal with Fisher-like models, among which the one by *Farrell et al.* [23] has called our attention. The model studied here describes growth of a colony of rod-shaped bacteria on a solid substrate, assuming mechanical interactions between bacterias (recall Fig. 1.1). The substrate contains a nutrient with initially constant concentration. Bacterias move as they consume the nutrient and also due to mechanical interactions. The interplay between these two mechanisms determines regimes in which the colony develops Fisher-like traveling waves or branches.

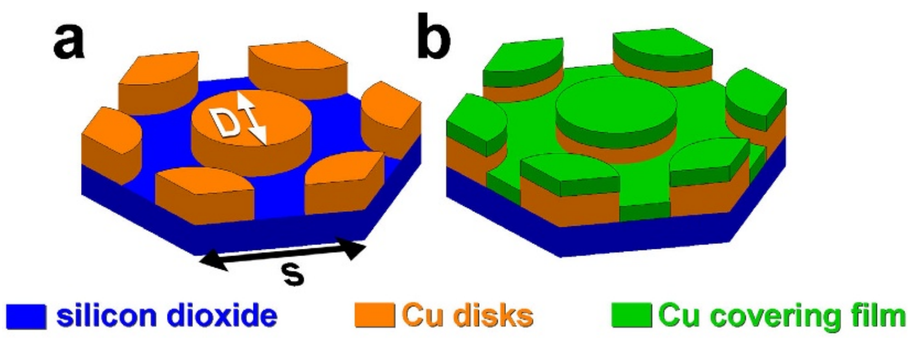

Figure 8.10: a) Illustration of a patterning process where cylinder arrays of diameter D are placed at equal distances from each other. b) The setup from (a) covered by a thin Cu film. Picture taken from *Kondic et. al* [142].

In this case the stochasticity comes from the cut-off theory and it would be interesting to assess the evolution of such systems including appropriate noise terms.

Regarding thin films, we have presented a theoretical study on the influence of noise in their evolution, in comparison to deterministic systems. We are still developing and testing a $3d$ algorithm to simulate geometrically more complicated setups. This is not an easy task, as the computational time rapidly increases with dimensionality. The ADI method can significantly reduce computational times by approximating a $3d$ system as a set of $1d$ systems. In reality, more iterations are needed to converge within a given tolerance, than the corresponding $1d$ system would take. Stochastic $2d$ systems need even more iterations, which requires making a choice between a large number of iterations or taking very small time steps. Optimization of this choice is still ongoing.

Back to physical problems, a very interesting geometry has called our attention, whose evolution is experimentally studied in [22]. The system contains a set of evenly-spaced thin cylinders, which are prepared on a substrate using electron beam lithography, see Fig. 8.10. Then, the film is exposed to a laser pulse, whose energy is selected so as to rise the cylinders temperature above the melting point. The cylinders transform into a liquid film that undergoes a dewetting process in which a pattern forms. The irregularity of the pattern increases with the increase in distance between the cylinders. Moreover, different irregularities are seen when, instead of a cylinder (circular section), different shapes are used, for example triangular or square sections. The deterministic evolution can be controlled by introducing appropriate perturbations into the initial condition, but it still seems limited as a description of the observed patterns. We believe that the stochastic SLE that we have studied could provide a better description of the experimental observations.

So far we have studied the SLE for a specific choice of the disjoining pressure. The corresponding interface potential is unstable, leading to the spinodal dewetting process that we have studied. It would be interesting to see how fluctuations affect the dynamics when for example an interface potential with a meta-stable states [21] is included. On the other hand, if gravity is not negligible, it is expected to set the upper limit for the film thickness, above which the linear SLE does not develop instabilities. The question arises whether such a limit still holds under the influence of fluctuations.

Resumen en Castellano

La investigación en fisica estadística se ha centrado en estudiar los estados en equilibrio que alcanza un sistema físico, mientras que la dinámica fuera del equilibrio, descrita por ejemplo por las ecuaciones diferenciales, solo es conocida en los casos más simples. El desarrollo de los ordenadores ha permitido a los investigadores estudiar numéricamente esta dinámica fuera del equilibiro. Los estudios basados en simulaciones numéricas no solo han hecho posible observar la evolución dinámica sino también, en muchos casos han contribuido en que se encontraran o mejoraran las predicciones analíticas [1–3]. Sin embargo, las simulaciones han hecho posible estudiar una gran variedad de modelos, como por ejemplo, modelos de partćulas, dadas las relaciones de interacción entre sí mismas, modelos explícitos, implícitos o semi-implícitos, basados en soluciones numéricas de las ecuaciones parciales diferenciales, modelos espectrales o pseudo-espectrales, etc. Estos modelos matemáticos, a parte de modelar los sistemas físicos tienen muchas aplicaciones en otros campos, especialmente en biología, química y economía. Además, la necesidad industrial de entender cuantitativamente los procesos en escalas muy pequeñas (micro y nano) requiere estudios numéricos para ver qué modelo describe mejor dichos procesos. Los modelos en los que se centran los trabajos presentados en esta tesis describen sistemas microfluídicos, como por ejemplo la evolución de una superficie o intercara entre fluido y vapor sobre un sustrato plano. Normalmente, en esas escalas (micro y nanoscópicas) es imposible desarrollar modelos teniendo en cuenta todas las interacciones conocidas, mientras los modelos fenomenológicos a veces son demasiado simples. Por esta razón, hemos estudiado la evolución de dos modelos simples con un ruido específico que trata de agrupar los efectos que se pierden simplificando la naturaleza de las interacciones, creando modelos más realistas. El primer modelo es un proceso reactivo-difusivo dado por la ecuación de Fisher-Kolmogorov-Petrovsky-Piscounov (FKPP), utilizada recientemente en bastantes sistemas biológicos. El segundo modelo representa los sistemas de películas delgadas y la evolución de las películas bajo diferentes situaciones físicas de la interacción fluido-sustrato.

La ecuación de FKPP es una de las ecuaciones de reacción-difusión más básicas, cuyas soluciones describen procesos biológicos como el movimiento de microorganismos por la comida o el crecimiento de poblaciones de genes [9, 11]. Para condiciones iniciales adecuadas, la ecuación [10] tiene soluciones cuya forma no cambia en el tiempo, sino que sólo se desplaza. Ese tipo de soluciones se conocen como ondas viajeras y su velocidad característica se puede hallar fácilmente. Fisicamente, por la forma del término de reacción, la ecuación representa cómo un estado estable invade a otro inestable. En realidad, los sistemas que describe esta ecuación dejan de ser continuos por debajo de una cierta escala espacial o densidad de partículas. Se ha demostrado que, con añadir un término estocástico adecuado, la ecuación también puede representar un sistema discreto [77]. Para la ecuación estocástica en una dimensión Brunet y Derrida demostraron numéricamente [7] que la velocidad de las ondas viajeras cambia drásticamente en el caso estocástico. Además, el cambio está relacionado con la amplitud de las fluctuaciones y lo más sorprendente es que se detecta incluso para fluctuaciones muy pequeñas que en un principio no deberían provocar ningún cambio en escalas macróscopicas.

Últimamente se han realizado muchos trabajos sobre algoritmos numéricos y simulaciones de las ecuaciones tipo FKPP en una dimensión. Sin embargo, hay muy pocos en $2d$ debido al coste computacional de los algoritmos numéricos habituales para sistemas continuos. Por otro lado, los algoritmos basados en simular partículas permiten realizar simulaciones sólo para números pequeños de partículas. Nosotros hemos desarrollado un algoritmo numérico en dos dimensiones basado en el método de separación de pasos (splitting step method) [88, 95] y las soluciones de ecuaciones Fokker-Planck asociadas [80, 85]. La idea de simular la ecuación en 2d vino de un trabajo [93] en el que se conjeturó que una familia de ecuaciones estocásticas que generaliza las FKPP tiene la misma dinámica que la ecuación de Kardar-Parisi-Zhang (KPZ) [1] en una dimension mayor, y se demostró numéricamente [92] para amplitudes grandes (pequeño número de partículas) utilizando el modelo de partículas. Nosotros hemos realizado simulaciones numéricas directas de la FKPP. El algoritmo empleado nos permite usar amplitudes del ruido muy pequeñas (número de particulas muy grande). Dichas simulaciones proporcionan los exponentes de crecimiento de superficie asociados a las ondas viajeras en $2d$, que para un ruido suficientemente pequeño son sin duda los de la ecuación KPZ en la misma dimensión. Además, hemos obtenido una ley de escala para el ruido según la cual para las fluctuaciones microscópicas el término estocástico es demasiado pequeño para ser visible en la región macroscópica, pero aun así la superficie se sigue arrugando. Definiendo dos líneas equipotenciales, una en la región microscópica y la otra en la región macroscópica, su correlación cruzada muestra la similitud entre ambas y proporciona un tiempo característico en el que la forma de la primera curva se propaga hasta la otra curva. Eso demuestra que las fluctuaciones en extremo de la onda viajera se propagan por la región macroscópica preservando los exponentes de crecimiento superficial. Finalmente, debido a la solución analítica [45] de la ecuación KPZ en una dimensión donde la altura de la superficie tiene la distribución de Tracy-Widom, hemos comprobado que la distribución de las las curvas equipotenciales macroscópicas y microscópicas son compatibles con dicha distribución. Esto es una prueba más a que el efecto del ruido se propague por el frente manteniendo unidimensionalidad de las lineas equipotenciales. Los resultados (menos las conclusiones respecto a la distribución de TW) están publicados en (1).

La ecuación de películas delgadas (PD) trata de describir un caso especial de la dinámica de los fluidos en un sustrato donde las perturbaciones características de la superficie son muy grandes respecto a la altura media de la película. En ese caso la dinámica de la película puede describirse como una ecuación para la intercara sometida a las diferentes fuerzas como la tension superficial, la interacción de van der Waals (vdW) y la gravedad [3, 151]. Nosotros hemos considerado un caso más realista, incluyendo un ruido térmico que tiene en cuenta las fluctuaciones de velocidad en el fluido. En el trabajo [4], simulaciones numéricas de la ecuación de PD estocástica mostraron que el ruido cambia la escala temporal en la que se extiende una gota en un regimen controlado por la tension superficial (sin contribuciones de vdW ni de la gravedad). Más recientemente se han hecho muchos experimentos de películas delgadas que muestran que la dinámica de la PD determinista no reproduce bien la observaciones respecto a la escala temporal característica o la forma del fluido [20]. Nuestro trabajo ha sido preparar el algoritmo empleado incluyendo términos adicionales en la ecuación de evolución para poder simular diferentes fluidos y estudiar la ecuación estocástica con una meta final de ver si la dinámica estocástica reproduce mejor los resultados experimentales [22]. Hemos encontrado que la escala temporal con la que se extiende una gota también cambia en presencia de ruido para un sistema bajo sólo el efecto de la gravedad. Además las simulaciones reproducen bien el cambio previsto teoréticamente [4]. También hemos encontrado que en un sistema donde el fluido con el sustrato forma un ángulo de contacto fijo, que representa el estado equilibrio entre la tension superficial y las interacciones de vdW [151], las fluctuaciones introducen un pequeño cambio en el ángulo observado en el mismo sistema determinista. Los resultados están publicados en (2)

Motivados por los resultados de la ecuación estocástica hemos estudiado una dinámica conocida como “dewetting” donde las películas planas, debido a las perturbaciones en la superficie [151], se forma un patrón de gotas. La versión lineal de la ecuación estocástica tiene un intervalo de ondas inestables donde existe una onda con el crecimiento más rápido, la cual da lugar a una longitud característica [108] que define el tamaño de las gotas [17]. Una de las mayores dificultades de las aproximaciones numéricas de ecuaciones de PD son las zonas donde coexisten las intercaras vapor-fluido y fluido-sustrato. Hay varias maneras de tratarlas [139], bien haciendo no nula la velocidad en la intercara o bien introduciendo una capa precursora, el caso que hemos considerado nosotros. De hecho, esa capa precursora se ha observado en varios experimentos [108]. Además, calculando los flujos, las gotas se comunican por ella, intercambiando la masa. El estado más favorable asimptóticamente es solo una gota grande [122] con lo cual no es consistente con la teoría lineal.

En tiempos cortos, nuestras simulaciones de las películas inicialmente planas y perturbadas con un ruido blanco, confirman la teoría lineal. El ruido acelera el proceso de creación de gotas comparado con el caso determinista. Al principio del régimen no lineal las ondas empiezan a acoplarse en ambos sistemas, lo que se manifiesta en apariencia de picos secundarios y diferente forma del factor de estructura. La longitud característica a partir del tiempo de ruptura supera el valor previsto con la teoría lineal donde el valor del sistema estocástico siempre está por debajo del valor determinista. En promedio, los sistemas estocásticos desarrollan menos gotas. Además, la anchura de la distribución de las distancias entre las gotas y la de sus alturas crecen con el crecimiento del ruido. En realidad, las gotas estocásticas se mueven más lateralmente por lo cual es más probable que las gotas acaben juntándo en el proceso de coalescencia. Esto resulta en más heterogeneidad de las gotas en los sistemas estocásticos. Nuestros resultados muestran que el ruido afecta el patrón del estado final aumentando la irregularidad de los patrones y es un mecanismo importante dado que en muchos sistemas experimentales los patrones creados no coinciden con la predicción lineal. Por otro lado, en tiempos aun más largos, los sistema no lineales determinista y estocásticos pasan por un proceso de ”coarsening” donde las gotas desaparecen en favor de sus vecinos mas grandes. Justo después de la creación, las gotas estocásitcas desaparecen más rápido comparado con el sistema determinista pero hasta un cierto tiempo después del que la evolución casi la misma. En ambos casos, por falta de estadística, tiempos inalcanzables u otro efecto, es difícil de observar la ley de potencia con la que baja el numero de gotas, prevista analíticamente [66, 67, 122–126]. Sin embargo nuestros resultados son compatibles con teorías efectivas del coarsening asintótico de gotas (cita). Los resultados del proceso ”dewetting” están publicados en (3).

Artículos Publicados y Preprints

1. S. Nesic, R. Cuerno, E. Moro, “*Macroscopic Response to Microscopic Intrinsic Noise in Three-Dimensional Fisher Fronts*”, *Physical Review Letters* **113**, 180602 (2014).
2. S. Nesic, R. Cuerno, E. Moro, L. Kondic, “*Dynamics of thin fluid films controlled by thermal fluctuations*”, *European Physical Journal Special Topics* **224**, 379 (2015).
3. S. Nesic, R. Cuerno, E. Moro, L. Kondic, “*Role of Thermal Fluctuations in Nonlinear Thin Film Dewetting*”, enviado a *Physical Review Letters* (2015).

A

Thin liquid films

A.1 Discrete stochastic lubrication equation

Here we give some steps that are skiped in the Sec. 6.1 for easiser reading. When discretized, the fourth order derivative is

$$f_i = \left[\partial_x \frac{h^3}{3}\,\partial_x^3 h\right]_i = \sum_{j=-2}^{2} a_j h_{i+j}, \tag{A.1}$$

where the coefficients a_j are non-linear terms grouped around the values h_{i+j}

$$\begin{aligned} a_2 &= D_{i+1/2} \qquad a_0 = 3\left(D_{i+1/2} + D_{i-1/2}\right) \qquad a_{-2} = D_{i-1/2} \\ a_1 &= -3D_{i+1/2} - D_{i-1/2} \qquad\qquad a_{-1} = -D_{i+1/2} - 3D_{i-1/2}, \end{aligned} \tag{A.2}$$

where the diffution coeficients are calculated using the centered differences

$$D_{i\pm 1/2} = (h_i^3 + h_{i\pm 1}^3)/2.$$

Eq. (6.9), which we recall here

$$-\frac{\partial F(h_i^{\nu+1})}{\partial h_j^{\nu+1}} = \delta_{ij} + \frac{\partial f_i}{\partial h_j^{\nu+1}} \Delta t \theta\, q_j, \tag{A.3}$$

accounts for derivatives of f_i with respect to h_{i+j} which are given by

$$a_{ii-2} = \frac{\partial f_i}{\partial h_{i-2}} = a_{-2} \tag{A.4}$$

$$a_{ii-2} = \frac{\partial f_i}{\partial h_{i-1}} = a_{-1} - \frac{3}{2} h_{i-1}^2 \left(h_{i+1} - 3h_i + 3h_{i-1} - h_{i-2}\right) \tag{A.5}$$

$$a_{ii} = \frac{\partial f_i}{\partial h_i} = a_0 + \frac{3}{2} h_{i-1}^2 \left(h_{i+2} - 4h_{i+1} + 6h_i - 4h_{i-1} - h_{i-2}\right) \tag{A.6}$$

$$a_{ii+1} = \frac{\partial f_i}{\partial h_{i+1}} = a_1 + \frac{3}{2} h_{i+1}^2 \left(h_{i+2} - 3h_{i+1} + 3h_{i-1} - h_{i-1}\right) \tag{A.7}$$

$$a_{ii-2} = \frac{\partial f_i}{\partial h_{i+2}} = a_2. \tag{A.8}$$

The elements a_{ij} form the matrix pentha-diagonal $\mathbf{A}$ ((6.11)).

References

[1] A.-L. Barábasi, *Fractal concepts in surface growth*. New York, NY, USA: Cambridge University Press, 1995.
Cited on pages I, 1, 3, 6, 7, 12, 31, 41, 47, 72, 73, 103, and 104.

[2] L. E. Reichl, *A modern course in statistical physics*, 3rd ed. Weihheim: Wiley, 2009.
Cited on pages I, 26, 50, and 103.

[3] H. Bruus, *Theoretical microfluidics*, ser. Oxford master series in physics. Oxford; New York: Oxford University Press, 2008.
Cited on pages I, 54, 103, and 105.

[4] B. Davidovitch, E. Moro, and H. Stone, *Physical Review Letters* **95**, (2005).
Cited on pages I, II, 15, 52, 56, 68, 72, 73, 74, 75, 76, 79, and 105.

[5] A. M. Willis and J. B. Freund, *Journal of Physics: Condensed Matter* **21**, 464128 (2009).
Cited on page I.

[6] D. Panja and W. van Saarloos, *Physical Review E* **66**, 036206 (2002).
Cited on pages I and 22.

[7] E. Brunet and B. Derrida, *Physical Review E* **56**, 2597 (1997).
Cited on pages I, 17, 22, 28, 47, and 104.

[8] E. Brunet, B. Derrida, A. H. Mueller, and S. Munier, *Europhysics Letters (EPL)* **76**, 1 (2006).
Cited on pages I and 28.

[9] R. A. Fisher, *Annals of Eugenics* **7**, 355 (1937).
Cited on pages I, 17, 21, and 103.

[10] A. N. Kolmogorov, I. Petrovsky, and N. Piskunov, *Mosc. Univ. Bull. Math* **1**, 1 (1937).
Cited on pages I, 17, 22, 27, and 104.

[11] J. D. Murray, *An introduction*. New York; London: Springer, 2002.
Cited on pages I, 17, 19, 22, 24, and 103.

[12] H. Hinrichsen, *Advances in physics* **49**, 815 (2000).
Cited on pages I and 21.

[13] R. Ledesma-Aguilar, R. Nistal, A. Hernández-Machado, and I. Pagonabarraga, *Nature Materials* **10**, 367 (2011).
Cited on page II.

[14] S. Dietrich, M. N. Popescu, and M. Rauscher, *Journal of Physics: Condensed Matter* **17**, S577 (2005).
Cited on page II.

[15] T. M. Squires and S. R. Quake, *Reviews of Modern Physics* **77**, 977 (2005).
Cited on page II.

[16] E. Delamarche, D. Juncker, and H. Schmid, *Advanced Materials* **17**, 2911 (2005).
Cited on page II.

[17] G. Grün, K. Mecke, and M. Rauscher, *Journal of Statistical Physics* **122**, 1261 (2006).
Cited on pages II, 15, 52, 55, 73, 86, 89, and 105.

[18] R. Fetzer, M. Rauscher, R. Seemann, K. Jacobs, and K. Mecke, *Physical Review Letters* **99**, (2007).
Cited on pages II, 68, 82, 83, 84, 85, 86, 88, and 89.

[19] A. G. González, J. Diez, R. Gratton, and J. Gomba, *Europhysics Letters (EPL)* **77**, 44001 (2007).
Cited on pages II, 49, and 50.

[20] A. G. González, J. A. Diez, Y. Wu, J. D. Fowlkes, P. D. Rack, and L. Kondic, *Langmuir* **29**, 9378 (2013).
Cited on pages II, 57, 69, 77, 81, 85, 88, 89, and 105.

[21] T. D. Nguyen, M. Fuentes-Cabrera, J. D. Fowlkes, and P. D. Rack, *Physical Review E* **89**, (2014).
Cited on pages II, 81, and 100.

[22] J. D. Fowlkes, L. Kondic, J. Diez, Y. Wu, and P. D. Rack, *Nano Letters* **11**, 2478 (2011).
Cited on pages II, 81, 100, and 105.

[23] F. D. C. Farrell, O. Hallatschek, D. Marenduzzo, and B. Waclaw, *Physical Review Letters* **111**, 168101 (2013).
Cited on pages 2 and 99.

[24] F. Family and T. Vicsek, Eds., *Dynamics of fractal surfaces*. Singapore; River Edge, N.J: World Scientific, 1991.
Cited on pages 1 and 5.

[25] B. B. Mandelbrot, *The fractal geometry of nature*. San Francisco: W.H. Freeman, 1982.
Cited on pages 1 and 6.

[26] P. Meakin, *Fractals, scaling and growth far from equilibrium*. Cambridge University Press, 2011.
Cited on page 1.

[27] D. Blank, M. Bijlsma, R. Moerman, H. Rogalla, F. Stork, and A. Roshko, *Journal of Alloys and Compounds* **251**, 31 (1997).
Cited on page 5.

[28] F. Family, *Journal of Physics A: Mathematical and General* **19**, L441 (1986).
Cited on pages 6 and 7.

[29] M. Kardar, *Statistical physics of fields*. Cambridge; New York: Cambridge University Press, 2007.
Cited on pages 8 and 73.

[30] M. Plischke, *Equilibrium statistical physics*, 3rd ed. Hackensack, NJ: World Scientific, 2006.
Cited on page 8.

[31] J. P. Boyd, *Chebyshev and Fourier spectral methods*, 2nd ed. Mineola, N.Y: Dover Publications, 2001.
Cited on pages 8 and 89.

[32] J. Krug, *Physica A: Statistical Mechanics and its Applications* **313**, 47 (2002).
Cited on page 11.

[33] A. C. Levi and M. Kotrla, *Journal of Physics: Condensed Matter* **9**, 299 (1997).
Cited on page 11.

[34] M. Kardar, G. Parisi, and Y.-C. Zhang, *Physical Review Letters* **56**, 889 (1986).
Cited on pages 11, 12, and 31.

[35] H. Holden, T. Lindstrøm, B. øksendal, J. Ubøe, and T. Zhang, *Communications in Partial Differential Equations* **19**, 119 (1994).
Cited on page 11.

[36] L. Bertini and G. Giacomin, *Communications in Mathematical Physics* **183**, 571 (1997).
Cited on page 11.

[37] L. D. Landau and E. M. Lifchitz, *Course of theoretical physics. Tome VI*. London; New York; Paris [etc.]: Pergamon press, 1959.
Cited on pages 11, 50, 52, and 54.

[38] H. S. Wio, C. Escudero, J. A. Revelli, R. R. Deza, and M. S. de la Lama, *Philosophical Transactions of the Royal Society A: Mathematical, Physical and Engineering Sciences* **369**, 396 (2011).
Cited on page 12.

[39] H. S. Wio, *International Journal of Bifurcation and Chaos* **19**, 2813 (2009).
Cited on pages 12 and 48.

[40] R. A. L. Almeida, S. O. Ferreira, T. J. Oliveira, and F. D. A. A. Reis, *Physical Review B* **89**, pp. 045 309–1 (2014).
Cited on page 12.

[41] T. Halpin-Healy and Y.-C. Zhang, *Physics Reports* **254**, 215 (1995).
Cited on pages 12 and 31.

[42] V. G. Miranda and F. D. A. Aarão Reis, *Physical Review E* **77**, 031134 (2008).
Cited on page 12.

[43] L. Canet, H. Chaté, B. Delamotte, and N. Wschebor, *Physical Review Letters* **104**, (2010).
Cited on page 12.

[44] J. Kelling and G. Ódor, *Physical Review E* **84**, 061150 (2011).
Cited on page 12.

[45] P. Calabrese and P. Le Doussal, *Physical Review Letters* **106**, 250603 (2011).
Cited on pages 13 and 104.

[46] T. Sasamoto and H. Spohn, *Physical Review Letters* **104**, (2010).
Cited on page 13.

[47] C. A. Tracy and H. Widom, *Communications in Mathematical Physics* **159**, 151 (1994).
Cited on pages 13 and 43.

[48] M. Prähofer and H. Spohn, *Physical Review Letters* **84**, 4882 (2000).
Cited on page 13.

[49] K. Johansson, *Communications in Mathematical Physics* **209**, 437 (2000).
Cited on page 13.

[50] K. A. Takeuchi, M. Sano, T. Sasamoto, and H. Spohn, *Scientific Reports* **1**, 1 (2011).
Cited on pages 13 and 48.

[51] M. Nicoli, R. Cuerno, and M. Castro, *Journal of Statistical Mechanics: Theory and Experiment* **2013**, P11001 (2013).
Cited on pages 13 and 14.

[52] T. Sasamoto and H. Spohn, *Journal of Statistical Mechanics: Theory and Experiment* **2010**, P11013 (2010).
Cited on page 13.

[53] S. N. Santalla, J. Rodríguez-Laguna, and R. Cuerno, *Physical Review E* **89**, (Jan. 2014).
Cited on page 14.

[54] P. Le Doussal, *Journal of Statistical Mechanics: Theory and Experiment* **2014**, P04018 (2014).
Cited on page 14.

[55] T. Gueudré and P. L. Doussal, *Europhysics Letters* **100**, 26006 (Oct. 2012).
Cited on page 14.

[56] P. Calabrese, P. L. Doussal, and A. Rosso, *Europhysics Letters* **90**, 20002 (2010).
Cited on page 14.

[57] T. Halpin-Healy and G. Palasantzas, *Europhysics Letters* **105**, 50001 (Mar. 2014).
Cited on page 14.

[58] K. A. Takeuchi and M. Sano, *Physical Review Letters* **104**, (2010).
Cited on page 14.

[59] M. Cross and H. Greenside, *Pattern formation and dynamics in nonequilibrium systems*. Cambridge, UK; New York: Cambridge University Press, 2009.
Cited on pages 14 and 86.

[60] R. Cuerno, M. Castro, J. Munoz-García, R. Gago, and L. Vázquez, *The European Physical Journal Special Topics* **146**, 427 (2007).
Cited on pages 14 and 15.

[61] A. Novick-Cohen, *Physica D: Nonlinear Phenomena* **26**, 403 (1987).
Cited on page 14.

[62] C. Misbah, H. Müller-Krumbhaar, and D. E. Temkin, *Journal de Physique I* **1**, 585 (1991).
Cited on page 14.

[63] R. Cuerno and A.-L. Barabási, *Physical Review Letters* **74**, 4746 (1995).
Cited on page 14.

[64] A. Karma and C. Misbah, *Physical Review Letters* **71**, 3810 (1993).
Cited on page 14.

[65] O. Pierre-Louis and C. Misbah, *Physical Review Letters* **76**, 4761 (1996).
Cited on page 14.

[66] A. Bray, *Advances in Physics* **43**, 357 (1994).
Cited on pages 15, 86, 95, and 106.

[67] F. Corberi and P. Politi, Eds., *Coarsening dynamics*, ser. Comptes Rendus Physique, 2015.
Cited on pages 15 and 106.

[68] K. Sneppen, J. Krug, M. H. Jensen, C. Jayaprakash, and T. Bohr, *Physical Review A* **46**, R7351 (1992).
Cited on page 16.

[69] R. Cuerno, H. A. Makse, S. Tomassone, S. T. Harrington, and H. E. Stanley, *Physical Review Letters* **75**, 4464 (1995).
Cited on page 16.

[70] D. A. Kessler and H. Levine, *Nature* **394**, 556 (1998).
Cited on pages 17, 26, and 99.

[71] J. Armero, J. Casademunt, L. Ramirez-Piscina, and J. M. Sancho, *Physical Review E* **58**, 5494 (1998).
Cited on page 17.

[72] J. L. Cardy and U. C. Täuber, *Journal of Statistical Physics* **90**, 1 (1998).
Cited on page 17.

[73] F. Sagués, J. Sancho, and J. García-Ojalvo, *Reviews of Modern Physics* **79**, 829 (2007).
Cited on page 17.

[74] W. van Saarloos, *Physics Reports* **386**, 29 (2003).
Cited on page 17.

[75] D. Panja, *Physics Reports* **393**, 87 (2004).
Cited on pages 17, 22, and 29.

[76] P. Grindrod, *Patterns and waves: the theory and applications of reaction-diffusion equations*, ser. Oxford applied mathematics and computing science series. Oxford: New York: Clarendon Press ; Oxford University Press, 1991.
Cited on page 17.

[77] C. R. Doering, C. Mueller, and P. Smereka, *Physica A: Statistical Mechanics and its Applications* **325**, 243 (2003).
Cited on pages 22, 26, 27, and 104.

[78] D. Lima, W. van Saarloos, and A. De Wit, *Physica D: Nonlinear Phenomena* **218**, 158 (2006).
Cited on page 22.

[79] C. W. Gardiner, *Handbook of stochastic methods for physics, chemistry, and the natural sciences*. Berlin; New York: Springer-Verlag, 1985.
Cited on pages 25, 27, 33, 34, and 36.

[80] L. Pechenik and H. Levine, *Physical Review E* **59**, 3893 (1999).
Cited on pages 26, 35, and 104.

[81] N. G. v. Kampen, *Stochastic processes in physics and chemistry*. Amsterdam; New York: North-Holland, 1992.
Cited on page 26.

[82] N. Van Kampen and I. Oppenheim, *Physica A: Statistical Mechanics and its Applications* **138**, 231 (1986).
Cited on page 26.

[83] J. Cook and B. Derrida, *Journal of Statistical Physics* **61**, 961 (1990).
Cited on page 28.

[84] E. Moro, *Physical Review E* **70**, 045102 (2004).
Cited on pages 28, 33, and 35.

[85] I. Dornic, H. Chaté, and M. Muñoz, *Physical Review Letters* **94**, (2005).
Cited on pages 28, 33, and 104.

[86] E. Brunet, B. Derrida, A. Mueller, and S. Munier, *Physical Review E* **73**, 056126 (2006).
Cited on pages 28, 29, 44, and 45.

[87] C. Mueller, L. Mytnik, and J. Quastel, *Inventiones Mathematicae* **184**, 405 (2011).
Cited on pages 28 and 30.

[88] E. Moro, *Physical Review Letters* **87**, 238303 (2001).
Cited on pages 29, 41, and 104.

[89] C. Mueller and R. Sowers, *Journal of Functional Analysis* **128**, 439 (1995).
Cited on page 29.

[90] D. Panja, *Physical Review E* **68**, 065202 (2003).
Cited on pages 29 and 30.

[91] E. Moro, *Physical Review E* **69**, 060101 (2004).
Cited on page 30.

[92] G. Tripathy, A. Rocco, J. Casademunt, and W. van Saarloos, *Physical Review Letters* **86**, pp. 5215–5218 (2001).
Cited on pages 31, 39, 48, and 104.

[93] G. Tripathy and W. Van Saarloos, *Physical Review Letters* **85**, 3556 (2000).
Cited on pages 32 and 104.

[94] O. Hallatschek and K. Korolev, *Physical Review Letters* **103**, (2009).
Cited on page 32.

[95] E. Moro and H. Schurz, *SIAM Journal on Scientific Computing* **29**, 1525 (2007).
Cited on pages 32, 34, and 104.

[96] F. C. Klebaner, *Introduction to stochastic calculus with applications*, 2nd ed. London; Hackensack, N.J: Imperial College Press, 2005.
Cited on page 33.

[97] S. M. Ross, *Stochastic processes*, 2nd ed., ser. Wiley series in probability and statistics. New York: Wiley, 1996.
Cited on page 33.

[98] H. Risken, *The Fokker-Planck equation: methods of solution and applications*, 2nd ed., ser. Springer series in synergetics. New York: Springer-Verlag, 1996.
Cited on page 34.

[99] W. H. Press, Ed., *Numerical recipes in C: the art of scientific computing*, 2nd ed. Cambridge; New York: Cambridge University Press, 1992.
Cited on pages 37 and 40.

[100] T. J. Oliveira, S. G. Alves, and S. C. Ferreira, *Physical Review E* **87**, 040102 (2013).
Cited on page 41.

[101] D. Panja and W. van Saarloos, *Physical Review E* **65**, 057202 (2002).
Cited on page 45.

[102] O. Hallatschek, P. Hersen, S. Ramanathan, and D. R. Nelson, *Proceedings of the National Academy of Sciences* **104**, 19926 (2007).
Cited on page 47.

[103] M. Reiter, S. Rulands, and E. Frey, *Physical Review Letters* **112**, 148103 (2014).
Cited on page 47.

[104] M. Henkel, *Non-equilibrium phase transitions*, ser. Theoretical and mathematical physics. Dordrecht [Netherlands]; New York: Springer, 2008.
Cited on page 48.

[105] L. Arnold and P. Imkeller, *Probability Theory and Related Fields* **110**, 559 (1998).
Cited on page 48.

[106] L. Arnold, N. Sri Namachchivaya, and K. R. Schenk-Hoppé, *International Journal of Bifurcation and Chaos* **06**, 1947 (1996).
Cited on page 48.

[107] J. Eggers, *Reviews of Modern Physics* **69**, 865 (1997).
Cited on pages 49 and 82.

[108] J. A. Diez and L. Kondic, *Physics of Fluids* **19**, 072107 (2007).
Cited on pages 49, 50, 57, 58, 71, 77, 79, 82, 85, 86, 89, and 105.

[109] R. V. Craster and O. K. Matar, *Reviews of Modern Physics* **81**, 1131 (2009).
Cited on page 49.

[110] R. V. Craster and O. K. Matar, *Physics of Fluids* **17**, 032104 (2005).
Cited on page 49.

[111] M. R. E. Warner, R. V. Craster, and O. K. Matar, *Journal of Fluid Mechanics* **510**, 169 (2004).
Cited on page 49.

[112] A. Oron, S. H. Davis, and S. G. Bankoff, *Reviews of Modern Physics* **69**, 931 (1997).
Cited on pages 49 and 55.

[113] N. Tipei, *Journal of Lubrication Technology* **104**, 510 (1982).
Cited on page 51.

[114] S. Porthun, L. Abelmann, and C. Lodder, *Journal of Magnetism and Magnetic Materials* **182**, 238 (1998).
Cited on page 51.

[115] H.-J. Butt, K. Graf, and M. Kappl, *Physics and chemistry of interfaces*. John Wiley & Sons, 2006.
Cited on pages 52, 53, 56, and 78.

[116] S. Boatto, L. P. Kadanoff, and P. Olla, *Physical Review E* **48**, 4423 (1993).
Cited on page 56.

[117] P. de Gennes, *Reviews of Modern Physics* **57**, 827 (1985).
Cited on pages 56 and 57.

[118] P.-G. d. Gennes, F. Brochard-Wyart, and D. Quéré, *Capillarity and wetting phenomena drops, bubbles, pearls, waves*. New York: Springer, 2004.
Cited on page 56.

[119] J. N. Israelachvili, *Intermolecular and surface forces*. San Diego, Calif: Academic Press, 2011.
Cited on pages 56, 57, and 58.

[120] D. Bonn, J. Eggers, J. Indekeu, J. Meunier, and E. Rolley, *Reviews of Modern Physics* **81**, 739 (2009).
Cited on pages 56, 57, 72, 77, and 81.

[121] J. Eggers, J. R. Lister, and H. A. Stone, *Journal of Fluid Mechanics* **401**, 293 (1999).
Cited on page 57.

[122] K. Glasner and T. Witelski, *Physical Review E* **67**, (2003).
Cited on pages 57, 85, 86, 91, 93, 94, 95, 105, and 106.

[123] K. B. Glasner and T. P. Witelski, *Physica D: Nonlinear Phenomena* **209**, 80 (2005).
Cited on pages 57 and 106.

[124] M. Gratton and T. Witelski, *Physical Review E* **77**, (2008).
Cited on pages 57 and 106.

[125] M. B. Gratton and T. P. Witelski, *Physica D: Nonlinear Phenomena* **238**, 2380 (2009).
Cited on pages 57 and 106.

[126] T. P. Witelski, *Advances in Water Resources* **28**, 1133 (2005).
Cited on pages 57 and 106.

[127] L. M. Hocking, *Physics of Fluids A: Fluid Dynamics* **5**, 793 (1993).
Cited on page 58.

[128] L. M. Hocking, *Physics of Fluids* **6**, 3224 (1994).
Cited on page 58.

[129] V. S. Ajaev, *Journal of Colloid and Interface Science* **280**, 165 (2004).
Cited on page 58.

[130] V. S. Ajaev, T. Gambaryan-Roisman, and P. Stephan, *Journal of Colloid and Interface Science* **342**, 550 (2010).
Cited on page 58.

[131] Q. Wu and H. Wong, *Journal of Fluid Mechanics* **506**, 157 (2004).
Cited on page 58.

[132] F. London, *Transactions of the Faraday Society* **33**, 8b (1937).
Cited on page 58.

[133] T. Yi and H. Wong, *Journal of Colloid and Interface Science* **313**, 579 (2007).
Cited on page 58.

[134] E. Yeh, J. Newman, and C. Radke, *Colloids and Surfaces A: Physicochemical and Engineering Aspects* **156**, 137 (1999).
Cited on page 58.

[135] J. Diez, L. Kondic, and A. Bertozzi, *Physical Review E* **63**, (2000).
Cited on pages 62, 72, 86, and 87.

[136] A. L. Bertozzi and M. Pugh, *Nonlinearity* **7**, 1535 (1994).
Cited on page 62.

[137] L. Zhornitskaya and A. L. Bertozzi, *SIAM Journal on Numerical Analysis* **37**, 523 (1999).
Cited on pages 62 and 86.

[138] B. T. Polyak, *Journal of Mathematical Sciences* **133**, 1513 (2006).
Cited on page 63.

[139] J. A. Diez and L. Kondic, *Journal of Computational Physics* **183**, 274 (2002).
Cited on pages 66, 87, and 105.

[140] T. Witelski and M. Bowen, *Applied Numerical Mathematics* **45**, 331 (2003).
Cited on page 67.

[141] T.-S. Lin, L. Kondic, and A. Filippov, *Physics of Fluids* **24**, 022105 (2012).
Cited on page 67.

[142] L. Kondic, N. Dong, Y. Wu, J. Fowlkes, and P. Rack, *The European Physical Journal Special Topics* **224**, 369 (2015).
Cited on pages 67 and 100.

[143] L. Kondic, *Siam review* **45**, 95 (2003).
Cited on page 67.

[144] T.-S. Lin, L. Kondic, U. Thiele, and L. J. Cummings, *Journal of Fluid Mechanics* **729**, pp. 214–230 (Aug. 2013).
Cited on page 67.

[145] K. Mecke and M. Rauscher, *Journal of Physics: Condensed Matter* **17**, S3515 (2005).
Cited on pages 68 and 84.

[146] D. G. A. L. Aarts, *Science* **304**, 847 (2004).
Cited on pages 69, 74, and 76.

[147] Y. Hennequin, D. Aarts, J. van der Wiel, G. Wegdam, J. Eggers, H. Lekkerkerker, and D. Bonn, *Physical Review Letters* **97**, (2006).
Cited on pages 69, 74, and 76.

[148] S. Nesic, R. Cuerno, E. Moro, and L. Kondic, *The European Physical Journal Special Topics* **224**, 379 (2015).
Cited on page 71.

[149] L. H. Tanner, *Journal of Physics D: Applied Physics* **12**, 1473 (1979).
Cited on pages 72 and 74.

[150] M. Rauscher and S. Dietrich, *Annual Review of Materials Research* **38**, 143 (2008).
Cited on page 81.

[151] J. Eggers and E. Villermaux, *Reports on Progress in Physics* **71**, 036601 (2008).
Cited on pages 81, 82, and 105.

[152] L. Yang and G. M. Homsy, *Physics of Fluids* **19**, 044101 (2007).
Cited on page 82.

[153] F. Dörfler, M. Rauscher, and S. Dietrich, *Physical Review E* **88**, 012402 (2013).
Cited on page 82.

[154] K. B. Lauritsen, R. Cuerno, and H. A. Makse, *Physical Review E* **54**, 3577 (1996).
Cited on page 84.

[155] R. Limary and P. F. Green, *Langmuir* **19**, 2419 (2003).
Cited on pages 85, 86, 91, and 93.

[156] A. Torcini and P. Politi, *The European Physical Journal B* **25**, 519 (2002).
Cited on page 86.

[157] A. J. Roberts, *Physica (Amsterdam)* **387A**, 12 (2008).
Cited on page 48.

[158] "See Supplemental Material for a movie (S1-movie.mp4) in which the $h(x,t)$ and $S_q(t)$ curves, together with the histograms of individual drop heights and inter-drop distances, are all shown for times $t \in [1, 250]$, for deterministic and stochastic simulations of Eq. (8.1)."
Cited on pages 89 and 91.

[159] "See supplemental material for a movie (S2-movie.mp4) showing the evolution of $h(x,t)$ in this regime."
Cited on pages 94 and 95.

[160] "See supplemental material for a movie (S-movie.mp4) showing the evolution of a $2d$ FKPP wave."
Cited on page 44.